

UC Berkeley

UC Berkeley Electronic Theses and Dissertations

Title

3D Printing with Post-processing for Piezoelectret Energy Harvesters and Vacuum Electronics

Permalink

<https://escholarship.org/uc/item/5ss6s2vf>

Author

karakurt, ilbey

Publication Date

2020

Peer reviewed|Thesis/dissertation

3D Printing with Post-processing for Piezoelectret Energy Harvesters
and Vacuum Electronics

By

Ilbey Karakurt

A dissertation submitted in partial satisfaction of the
requirements for the degree of

Doctor of Philosophy

in

Engineering - Mechanical Engineering

in the

Graduate Division

of the

University of California, Berkeley

Committee in charge:

Professor Liwei Lin, Chair

Professor Dorian Liepmann

Professor Lisa Pruitt

Professor Hayden Taylor

Spring 2020

**3D Printing with Post-processing for Piezoelectret Energy
Harvesters and Vacuum Electronics**

Copyright © 2020

by

Ilbey Karakurt

Abstract

3D Printing with Post-processing for Piezoelectret Energy Harvesters and Vacuum Electronics

by

Ilbey Karakurt

Doctor of Philosophy in Mechanical Engineering

University of California, Berkeley

Professor Liwei Lin, Chair

Additive manufacturing has been at the forefront of manufacturing research with advances in basic printing techniques, materials, and post-processing schemes. This work addresses two technical challenges in the broad spectrum of 3D printed structures: (1) functional surfaces and devices; (2) the surface finishing in terms of roughness.

In the first part of this dissertation, a post-fabrication process is investigated to create functional 3D printed structures that can be used for energy harvesting applications by converting mechanical energy to electricity. Chemical vapor deposition (CVD) of various Parylene layers is used to coat a thin film on top of the 3D printed polymer surfaces. The corona discharge method is then used to implant surface charges on the film to construct multi-layered energy harvesting structures. Experimentally, the prototypes can produce $12.5 \mu\text{W}/\text{cm}^2$. Then, a wearable shoe sole energy harvester has been created using 3D printing and CVD of Parylene C and tested in real-life scenarios such as walking, running, and jumping. The system can produce a peak power output of $8 \mu\text{W}/\text{cm}^2$ from a single layer design.

In the second part of this dissertation, a novel surface polishing method has been developed to polish enclosed structures by 3D printed waveguide structures for vacuum electronics for high frequency applications with very stringent surface finish requirements. Magnetic particles have been used in an abrasive slurry and a linear actuator system has been developed to move a magnet. The moving magnetic field can move the slurry inside an enclosed structure to polish the surface. The system has been tested on sample waveguide structures made of copper powders via the electron beam 3D printing process with an initial surface roughness of $40 \mu\text{m}$. By using the method developed in this dissertation, the surface roughness has been reduced to reach $1.5 \mu\text{m}$ in a waveguide.

Table of Contents

1. Chapter 1: 3D Printing Technologies -Techniques, Materials, and Post-processing	1
1.1. Overview of Widely Used 3D Printing Techniques	4
1.2. Material Selection	7
1.3. Current Limitations and Post-Processing Influences	11
1.4. Future Prospects of 3D Printing	13
1.5. Thesis Structure.....	13
2. Chapter 2: 3D Printed Piezoelectret Devices via Chemical Vapor Deposition of Parylene. 15	
2.1. Introduction	15
2.1.1. Overview of Piezoelectret Devices, Fabrication Methods, and Applications	15
2.2. 3D Printed Triboelectric Energy Harvesters via Chemical Vapor Deposition of Parylene AF4 18	
2.2.1. Device Design & Working Principle	18
2.2.2. Fabrication and Characterization	21
2.2.3. Drawbacks and potential improvements	27
2.3. 3D Printed Piezoelectret Shoe Sole Energy Harvester via Chemical Vapor Deposition of Parylene C.....	27
2.3.1. Device Design & Working Principle	28
2.3.2. Fabrication and Characterization	29
2.3.3. Experimental setup, Results, and Discussion	31
2.4. Conclusion.....	33
3. Chapter 3: Magnetically Driven Abrasive Flow Finishing for 3D Printed Internal Surfaces 35	
3.1. Literature Review	35
3.1.1. Vacuum Electronic Devices and Manufacturing Methods	35
3.1.2. Electron Beam Melting and Its Challenges	36
3.1.3. Surface Polishing Techniques.....	38
3.2. Surface Roughness and Proposed Polishing Methods	39
3.2.1. Fabrication of Samples and Surface Characterization	39
3.2.2. Electrochemical polishing.....	41
<i>i. Experiments and Results</i>	43
3.2.3. Magnetically Driven Abrasive Flow Polishing Process	49
3.3. Conclusion.....	72

4. Chapter 4: Conclusion and Outlook.....	73
4.1. Conclusion.....	73
4.2. Outlook & Future Works.....	74
4.2.1. 3D printed Energy Harvesters and soft devices	74
4.2.2. Metal 3D Printing Polishing	79
References.....	80
Appendix A: Appendix to Chapter 3	97

List of Figures

Figure 1.1: Trend of additive manufacturing technologies and its potential in the recent future... 2	2
Figure 1.2: General trends and applications in 3D printing..... 8	8
Figure 1.3: (a) Silicone gloves with embedded resistive strain sensors. Conductive carbon grease is extruded into a viscous silicone pre-polymer matrix. Changes in resistance can be used to monitor hand motions and gestures [76]; (b) Multi-core-shell direct ink writing of ionically conductive fluids and insulating silicone elastomers as strain-dependent capacitive sensors [77]; (c) Responsive graphene oxide sheets via DIW 3D printed. Drying and thermal reduction can lead to ultra-light graphene-only structures with restored conductivity and elastomeric behavior [78]; (d) Electronic components and systems fabricated by the combination of MJM and the liquid metal paste filling process [79]; (e) Conformal printing of electrically small antennas on convex (left) and concave (right) surfaces [80]. 10	10
Figure 1.4: (a) 3D printed energy harvesting structures made by polyurethane using a DLP printing system coated with Parylene AF4 to functionalize the surface via a post-printing process [56]; (b) 3D printed ethanol sensor fabricated using the polyjet printer. The surface is functionalized by post-printing with polyaniline using electropolymerization [86]; (c) Oxygen free high conductivity copper WR10 waveguide surface fabricated via electron beam melting. (left) As printed sample with rough surface. (right) Polished surface post-printing using magnetic abrasive polishing [30]; (d) Direct ink writing of sol-gel and glass components at various stages. By various heating steps in post-processing can be converted to SiO ₂ . [19]; (e) Sequential self-folding structures by 3D printed digital shape memory polymers [85]; (f) Antibiotic loaded chambers and the color changing reaction taken by a smart phone camera (antibiotic Ampicillin, Kanamycin, Ciprofloxacin, and Sulfamethoxazole are loaded in wells) [81]. 12	12
Figure 1.5: Thesis goals and structure. (1) Chemical vapor deposition of Parylene for piezoelectret energy harvesters. (2) Polishing methods for metal 3D printed vacuum electronic devices..... 13	13
Figure 2.1: Working Principle of piezoelectret devices..... 16	16
Figure 2.2: Typical photographs of some piezoelectret energy harvesting devices: (a) a cellular PP device for finger tapping [109]; (b) a sensor/energy harvester under harsh environment [110]; (c) a shoe insole energy harvester [111]; (d) a 3D stack to harvest energy from human motion [112]; (e) a fabric-based harvester for harvesting body motion energy [113]; (f) a 3D stack energy harvester for vibration energy [114]; (g) a foot/hand pressing energy harvester [115]. ... 17	17
Figure 2.3: Conceptual drawing of a multi-layer 3D printed triboelectric energy harvester (TEH) with high surface area by means of the 3D structure and the high surface charge density layer using the conformal coating process of Parylene AF4. The V-shaped supports are designed to separate the layers. A corona charging process is conducted to provide high surface charges. ... 19	19
Figure 2.4: Main working principle of piezoelectret energy harvester. From left to right, the device is shown first in its original configuration after the corona charging step. The charges are in a quasi-static equilibrium. Then the top layer of the device is compressed, and the equilibrium conditions change, forcing electron movement from one electrode to the other to create the electrical current. As the device is released, it returns to its original configuration. 19	19
Figure 2.5: COMSOL simulations of the displacement under a force of 3-Newton for devices with single, double and triple layers. 20	20

Figure 2.6: The fabrication details of the stereolithographic 3D printing process with the continuous liquid interface printing for the energy harvesters. The UV LED is applied from the bottom of the system and the high-resolution screen is used as the optical mask. The UV-curable resin is illuminated by the UV light and the cured structure is pulled by the build platform. Various 3D printed devices can be made in the same batch. 21

Figure 2.7: (a) The conformal Parylene AF4 coating process; (b) the corona charging process; and (c) metallization for the electrodes. 21

Figure 2.8: Optical photo of an actual device as compared with a U.S. penny. The top electrode has a coating of aluminum. 22

Figure 2.9: SEM image showing different locations on the 3D printed structure. (a) The cross-sectional image shows the area where the support structure connects to the top and bottom layers. The various measurements are also used to compare to the original design. (b) Structure’s side surface image showing the striations on the surface indicative of the layer height. (c) A closer view of the side surface in (b). 23

Figure 2.10: Uniformity study of the Parylene deposition on the 3D printed samples. The samples are split into 6 regions and the measurements shown are the average heights taken at 3 different points along each side of the samples. 23

Figure 2.11: Cross-sectional view of the Parylene coated 3D printed structure. (a) Zoomed out image showing both top and bottom layer. (b) Zoomed in image showing the top layer which has metal layer on the top and Parylene layer on the bottom. (c) The metal layer (gold) and 3D printed polyurethane is shown. (d) 3D printed polyurethane coated with Parylene AF4 is shown. 24

Figure 2.12: (a) Surface charge measurement; (b) Surface charge potential vs. time after the corona charging process. The surface charges is stabilized at -12 Volts. 24

Figure 2.13: Initial performance of samples. Compressive force applied at approximately (a) 2 Hz; (b) 3 Hz; (c) 4 Hz. 25

Figure 2.14: Sample attached to mechanical testing setup (a) Uncompressed. (b) Compressed... 25

Figure 2.15: (a) Short circuit current output of single-, double-, and triple-layer devices tested separately. (b) A shorter time-frame of the results shown in (a) are shown to highlight the details in output performance. (c) A triple-layer device is pressed on (red) and compared to a free-standing device (blue) to compare the output. 26

Figure 2.16: Output performance of a triple-layer device under a 3-Newton force at 2 Hz. (a) Short circuit current. (b) Current and power output over varying resistors. 27

Figure 2.17: (a) Wearable devices; (b) IDTechEx Wearable Technology market projections for the year 2025 [145] 28

Figure 2.18: Shoe sole concept showing the different materials used for each layer.[150] 28

Figure 2.19: (a) PolyJet Multimaterial printing process showing the droplets of different materials being jetted on to the printing surface. (b) Water-soluble support that allows for overhangs to be printed. (c) Parylene C coated surface. 29

Figure 2.20: Fabricated shoe insole 30

Figure 2.21: (a) Surface charge decay of Parylene C coated on the test sample with different charging time periods. (b) Initial results showing the energy harvesting shoe sole in use. The device can be used to harvest energy while walking, running, and jumping. 31

Figure 2.22: Varying force and amplitude testing of shoe insole. (a), (b), (c), (d) are short circuit current outputs and (e), (f), (g), (h) are tested with an external resistive load. (a) & (e) Under light foot tapping condition tested at 1Hz; (b) & (f) Progressively stronger foot tapping; (c) & (g) light foot tapping condition tested at 3Hz; (d) & (h) a single jumping motion.	32
Figure 2.23: Comparison of different materials [56,154–156]	33
Figure 3.1: Typical setup for Electron Beam Melting (EBM) based system showing the two major compartments and the raking system needed. The part is fabricated on the build plate via electron beam. The unfused particles surrounding the part is removed by post processing. Dark brown particles are unfused copper particles, where as the lighter brown region is fused copper particles.	36
Figure 3.2: Electron Beam Melting (EBM) system used by North Carolina State University. (a) Schematic showing each component, (b) Real device image. Courtesy of North Carolina State University CAMAL	37
Figure 3.3: A chess-piece manufactured by NCSU, qualitatively showing the unfused particles on the surface of the sample. (a) Chess piece from afar, (b) zoomed in photograph of side surface, (c) SEM image of side surface.	40
Figure 3.4: Comparison of two different surfaces of the sample to show the differences in surface texture of side (left image) and top (right image) surfaces.	40
Figure 3.5: Surface roughness of as fabricated samples. These measurements were done both for the top and side surfaces. The surface roughness values approximately 1 standard deviation away from the mean are those of the side surface. The samples with low surface roughness correspond to the top surface measurements	41
Figure 3.6: Surface roughness distribution of samples	41
Figure 3.7: Electrochemical polishing. (a) Electrochemical polishing cell showing the smoothening mechanism qualitatively. (b) Polarization curve adopted from [182].....	42
Figure 3.8: Samples used to conduct optimization experiments: (a) a half cylinder-shape sample used to run initial experiments; (b) flat rectangular-shape sample used to easy quantify the surface roughness using contact profilometry; (c) flat 0.5 x 0.5 in ² samples with thicknesses ranging from 1 to 4 mm.	44
Figure 3.9: Electrochemical polishing setup consisting of Gamry electrochemical unit, hot-plate heater, stainless steel electrode and stainless-steel counter electrode.....	44
Figure 3.10: Electropolishing optimization results for the surface roughness with respect to: (a) electrolyte molarity; (b) processing temperature; (c) current density; and (d) processing time. The optimized process is for 10M of electrolyte, 55°C of processing temperature, 1 A/in ² of current density and 25 min of processing time.	45
Figure 3.11: Cube-shape samples. (a) Top surface of a cube-shape sample with build direction normal to the top surface. Accumulation of powder due to uneven sintering during operation can be seen. (b) Side wall of the same sample showing rugged surface and layered structure.	46
Figure 3.12: Directionality analysis. (left) Side wall surface roughness before and after the electrochemical polishing process to show significant reductions in the surface roughness. (right) Top face surface roughness before and after the electrochemical polishing process to show increases in the surface roughness.	46
Figure 3.13: SEM images of side wall: (a) the pre-polishing SEM image showing regions where	

powder has not fully fused to form voids; (b) the post-polishing image showing a smoother texture and less voids.	47
Figure 3.14: SEM images of top surface: (left) the pre-polishing SEM image showing a wavy surface, and (right) post-polishing SEM showing a less reflective and rougher surface.....	47
Figure 3.15: Electrochemical polishing results for surface roughness with respect to: (a) electrode surface area; and (b) electrode distance to the sample.....	48
Figure 3.16: Electrochemically polished sample: (a) pre-polishing surface, and (b) post-polishing surface. The mark indicated in (b) is the electrical connection portion. An overall decrease in surface texture and roughness can be seen visually.....	48
Figure 3.17: Surface morphology of a three-walled channel structure.....	49
Figure 3.18: Conceptual image of the magnetically driven abrasive flow polishing system	49
Figure 3.19: Detailed image showing the abrasive slurry containing the magnetic and abrasive particles over a copper work. The permanent magnet and the generated magnetic force lines show how the magnet can guide this slurry. The free-body diagram of a single magnetic particle is also shown. The forces acting on this particle can then be translated to “P”, the force acting on the surface by the abrasive particle.	50
Figure 3.20: Abrasive wear model for material removal [190]	50
Figure 3.21: Permanent magnet illustration showing the dimensions, infinitesimal element and point of evaluation (p). The center of the selected infinitesimal element has coordinates of x', y', z'	53
Figure 3.22: Magnetic flux density contour plots showing the magnetic flux density in units of Tesla at various distances from the surface of the permanent magnet. The force generated by the magnetic field on the abrasive particles is directly proportional to the magnetic flux density hence understanding how the flux density decays is an important parameter in designing the experimental setup.	55
Figure 3.23: The 2D geometry used for computational modeling showing the available domains.	56
Figure 3.24: Mapped mesh used in the computational model with the color bar representing element size. At time = 0s the mesh is not deformed. The consecutive time steps show how the mapped mesh is deformed.	58
Figure 3.25: Computational results for the magnetic flux density showing both a surface plot and the magnetic flux contour lines. The consecutive images (right to left and then top to bottom) show how the translational magnetic field and hence the magnetic flux density changes over 1 full cycle.....	59
Figure 3.26: Parameter sweep results showing how the magnetic flux density changes with varying air gap distance between the magnet and the copper piece and the magnetic flux density on the magnet’s surface. (a) Magnetic flux density 1 Tesla, and 2cm air gap. (b) Magnetic flux density 1 Tesla, and 4cm air gap. (c) Magnetic flux density 1.5 Tesla, and 2cm air gap. (d) Magnetic flux density 1.5 Tesla and 4cm air gap.	60
Figure 3.27: model of abrasive particle and the force being calculate (left). Computational calculation of force on a single particle (in N) (right)	61
Figure 3.28: Material removal process is conceptualized to show how the size of the abrasive particles can affect the overall material removal.	62

Figure 3.29: Normalized wear rate vs. iron particle concentration. The wear rate calculated for each concentration is normalized by the maximum achievable wear rate.	63
Figure 3.30: 3D rendering of conceptual experimental setup highlighting key components.	64
Figure 3.31: Wiring diagram for stepper motor driving the linear belt drive system.	65
Figure 3.32: An optical photo of the experimental setup.	65
Figure 3.33: Graphical user interface used to control the process parameters and the position of the permanent magnet.	66
Figure 3.34: Motion of the magnetic abrasive slurry under the influence of an external translational magnetic field. The images are taken in 0.2s intervals and the 6 images show 1 full cycle.	67
Figure 3.35: Processing results compared to as-fabricated samples. (a) The as-fabricated sample has many asperities, mostly due to unfused particles. (b) The processed sample has a smoother texture and less visible unfused particles.	68
Figure 3.36: Process optimization. (a) Particle concentration optimization, (b) Process cycle optimization, (c) Full polishing cycle on a single sample.	68
Figure 3.37: SEM images comparing surfaces pre (left) and post-polishing (right)	70
Figure 3.38: Post fabrication improvement samples before and after being polished: (a) visual comparison of polished and unpolished samples; (b) enlarged light microscopy image of surface after the polishing process; (c) SEM image of as fabricated sample; (d) SEM image of polished sample.	70
Figure 3.39: Modified experimental setup.	71
Figure 3.40:(a) Half-inch waveguide; (b) Waveguide cross-section; (c) Waveguide attached to experimental setup.	71
Figure 3.41: Signal losses in waveguide structure fabricated in figure 3.40.	72
Figure 4.1: (a) conceptual device with three different sensors and one actuator. (b) Device on the finger.	75
Figure 4.2: A modified 3D printing system.	76
Figure 4.3: Different airless tire concepts from commercial companies. (a) Bridgestone airless tire [201]; (b) Michelin airless tire [202]; (c) Goodyear Turf Command airless tire [200]; (d) Michelin airless tire on a real EV [199].	77
Figure 4.4: COMSOL Multiphysics simulation highlighting the displacement of the outer tire with respect to the inner wall.	78
Figure 4.5: Experimental setup concept to test the potential applicability of this idea to road vehicles.	78
Figure 4.6: 3D printed airless tire concepts.	79
Figure 4.7: A 2D motion polishing system.	79

List of Tables

Table 1.1: Additive manufacturing technologies. Various subcategories of 3D printing, the technologies that they use and the materials that can be printed with each technique is shown. Compiled from [1,6,8–10]	3
Table 1.1: Overview of Widely Used 3D Printing Techniques	4
Table 2.1: Material Selection and Charging Potentials [107].....	15
Table 3.1: Fabrication process parameters used by NCSU-CAMAL to fabricate the samples used throughout this chapter	39
Table 3.2: Optimization Parameters for Electrochemical Polishing using H ₃ PO ₄	43

To my parents,
Ilgün & Atalay Karakurt

Acknowledgments

I would like to express my sincere gratitude to my advisor, Professor Liwei Lin. Throughout my PhD he has been nothing but supportive, helpful, and an excellent advisor. Coming to Berkeley as a 22-year-old directly after receiving my BSc, I required guidance not just in what to study but also in how to conduct research at a higher level. Professor Lin was able to guide me patiently through this incredibly new environment. After my first two years, I believe we were able to form a very productive advisor-student relationship, which allowed me to explore different research areas. This allowed me to grow in ways I had not imaged coming into my Ph.D. I could not have asked for a better research advisor than Professor Lin and I will truly miss our weekly meetings chatting about research.

I want to express my appreciation to Professor Timothy Horn from NCSU-CAMAL. In my first three years here, I was able to work together with him and his students on the DARPA INVEST program. Through our collaboration we were able to develop the magnetically driven abrasive flow polishing process for 3D printed vacuum electronic devices. I could not have done it without them supplying me constantly with very expensive and time-consuming 3D printed copper samples.

I would like to express my appreciation to Professor Neville Luhmann from UC Davis and Dr. Diana Gamzina from UC Davis and SLACK for allowing me to use their lab space and equipment and for helping me understand much about vacuum electronic devices. Without their help I could not have developed the polishing process for the DARPA INVEST project.

I would like to specifically mention the undergraduate researchers I mentored over the past 5 years and thank them for their support in many of my projects. Derek (Kong Yin) Ho was the first student I mentored, and for 2 years he helped me immensely in developing the polishing process. Without his countless hours in the lab it would have been a lot harder to achieve results. Jesse Orozco has been working with me for the past 2 years and I would like to thank him not just for his hard work and perseverance but also his friendship. Among the many people I worked with, I don't think I have seen such a dedicated and hard-working person. I will miss eating pizza while watching football in between our experiments. Finally, I would like to thank Suchi Naryanan, who worked with me for approximately 1 year, whose friendship I will cherish going forward.

I want to express my deepest gratitude to my parents, İlgin and Atalay Karakurt. Their love, patience, encouragement, and support helped me pass through tough times and achieve my goals. Without them this journey would not have happened.

I am immensely thankful to the many friends who made this journey worth it. I would like to thank Arda Ozilgen, Dr. Levent Beker, Sedat Pala, Jacqueline Elwood, Dr. Eric Sweet for their kindness, friendship, and making this journey fun. I am truly thankful to Dr. Junwen Zhong for his friendship and help in my research.

It was a pleasure to work with all the members of the Lin Lab, NCSU-CAMAL and the UC Davis MMWPDG and I am thankful for their kindness and friendship. Through the years, I received much help from UC Berkeley Marvell Nanolab staff and Berkeley Sensor & Actuator Center staff which I'm very grateful. I would like to thank Sam Tsitrin for helping me set up the parylene coater in the nanolab, Naima Azgui for helping me in the BNC, and Paul Lum for training and helping me in the BNC over the past 5 years.

1. Chapter 1: 3D Printing Technologies -Techniques, Materials, and Post-processing

Manufacturing techniques and fabrication processes have been at the forefront of research and development and have been instrumental in achieving technological advancements in many fields. The interest in manufacturing dates all the way back to the beginning of civilization, when people invented tools and developed them to simplify real-world tasks. With advancements in manufacturing techniques humans were able to build bigger structures, build roads for faster travel, and even construct devices that could help them in their daily lives such as the personal computer and then the smart phone. In the last 200 years manufacturing has advanced at a phenomenal rate starting with the industrial revolution and it is still advancing today at an amazing pace with additive manufacturing techniques. These techniques significantly differ from conventional subtractive (i.e. milling, drilling), formative (i.e. casting, forging), and joining (i.e., welding) processes [1] since they allow the structures to be built from the bottom-up by depositing material at every pre-determined layer. Additive manufacturing techniques have immense advantages compared to conventional techniques, such as reducing waste material, allowing to build more complex structures, reducing build times, and reducing the need for assemblies. Due to such advantages they have drawn considerable attention worldwide from politicians (Obama 2013) to CEO's indicating a level of need recognized by industry and world leaders. For example, it is predicted that General Electric (GE) Aviation will produce over 100,000 parts for its LEAP and GE9X engines throughout their life cycle using metal additive manufacturing [1]. Additive manufacturing has also drawn interest from militaries worldwide. In 2010, The United States Navy published the results of a workshop on additive manufacturing envisioning affordable, durable, and structurally efficient aircraft components fabricated via additive manufacturing of metals [2]. Achieving this would allow for enhanced operational readiness, reduced energy consumption, and reduced total ownership cost showing the true potential and goal for additive manufacturing techniques [2]. One final example to truly show that additive manufacturing is the future would be to highlight its use in helping us along our path on conquering the final frontier: Space. Researchers and companies alike have invested in developing techniques which will allow us to build buildings on mars [3,4] and there have also been many advancements in producing spacecraft parts using additive manufacturing [5] .

However, the current state was not reached in a short period. Even though the potential applications and benefits were identified early on there was need for improvement both in terms of technology readiness and market-need. Starting from the mid '90s much effort was put into developing the tools and techniques required to meet these needs. In 1997 only 1057 rapid prototyping machines were sold world-wide [6], whereas 496,745 units shipped in 2016 alone [7]. Many consulting companies predict more than a 50% annual growth rate (in revenue) in the 3D printing market resulting in a \$180-490B industry by 2025 [7].

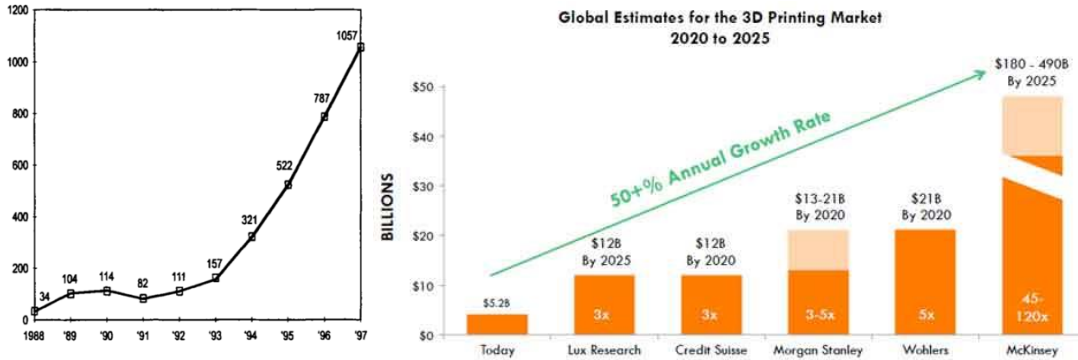


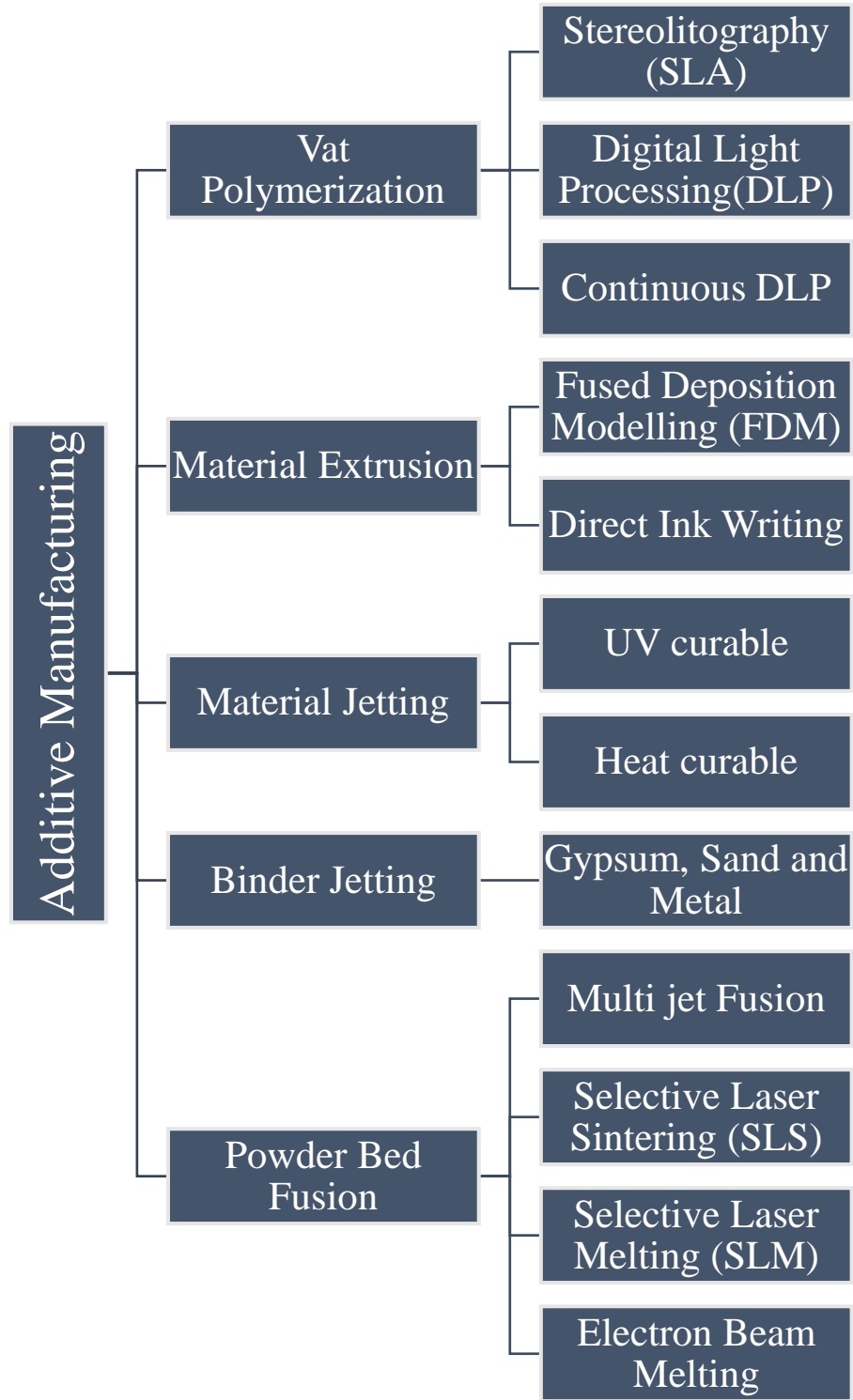
Figure 1.1: Trend of additive manufacturing technologies and its potential in the recent future; (a) the number of 3D printers sold between 1988 and 1997, adopted from Kruth et al. [6]. (b) Market growth estimates of 3D printing by major consulting companies predicting a potential market of \$180-400 billion by 2025. Adopted from [7].

To achieve this market growth, many different types of commercial additive manufacturing methods capable of producing parts from many different families of materials have been developed in the past years. These methods can be divided into categories by either the supply material they use: (1) liquid, (2) powder, (3) solid, (4) gas [6] or the technique used. The most prominent methods with respect to the materials used have been outlined in Table 1.1 and a more in-depth review has been given in Table 1.2.

It should be noted that certain technical limits to these methods still exist. Some technological challenges that still need to be overcome are: (1) process controls, sensors and models, (2) metallurgy, (3) mechanical properties, (4) fatigue, porosity and surface roughness [2,8]. Especially material properties and surface finishes achieved with these methods are still not on par with other conventional methods.

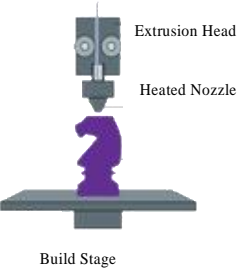
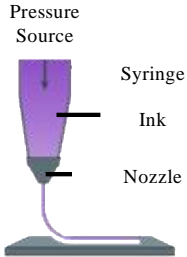
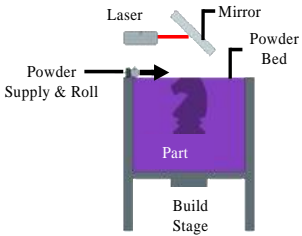
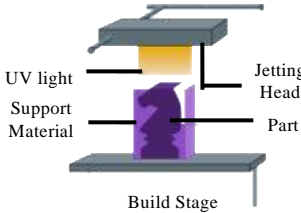
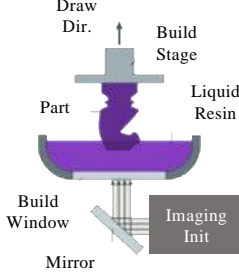
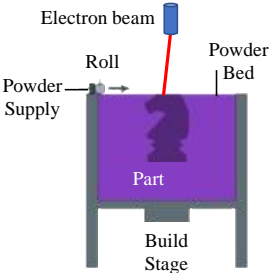
As such this chapter will aim to introduce the main concepts in additive manufacturing such as different techniques, material selection influences, and current limitations and post processing techniques. The goal of the thesis is to utilize the main concepts of 3D printing technologies mentioned here. This chapter will first focus on the most prominent additive manufacturing techniques currently being used or developed. The first section will cover the properties of these techniques and will show the reader application areas in which each of these techniques has been utilized. Then the second section of this chapter will cover material selection and material properties while also giving examples from different areas. Finally, the last section of this chapter will cover the current limitations of additive manufacturing and will show some post-processing techniques that have been used to either improve material and/surface properties or to functionalize the 3D printed structure.

Table 1.1: Additive manufacturing technologies. Various subcategories of 3D printing, the technologies that they use and the materials that can be printed with each technique is shown. Compiled from [1,6,9–11]



1 **1.1. Overview of Widely Used 3D Printing Techniques**

2 *Table 1.1: Overview of Widely Used 3D Printing Techniques*

	Fused deposition modelling	Direct ink writing	Selective Laser Sintering	Inkjet Printing	Stereolithography & Light-based Systems	Electron Beam Melting
Illustration						
x-y res	100µm	1-100µm	1-100µm	10-100µm	100nm-100µm	1-100µm
Materials	Thermoplastics, Cement	Hydrogels, composites	Metals and polymers	Methacrylate based polymer networks	Photocurable polymers networks	Metals and metal alloys
Application areas	<ul style="list-style-type: none"> • Micro-fluidics, • Soft robotics • Prosthetics, • Composite ceramics, • Composite metallic 	<ul style="list-style-type: none"> • Hydrogels for soft robotics • Hydrogels for drug encapsulation • Tribo-electric touch sensors • Ceramics for optics • Cellulose nano-crystals 	<ul style="list-style-type: none"> • Soft robotic hand & soft systems • Turbine blades • Engines, brakes • Prosthetics and implants • Vacuum electronic devices 	<ul style="list-style-type: none"> • Microfluidics, • Soft robotics, • Structural components, • Sensors, actuators, and energy harvesters. 	<ul style="list-style-type: none"> • Microfluidics, • Soft robotics, • Micro pillars, fibers, and springs for cell studies 	<ul style="list-style-type: none"> • Aerospace, • Vacuum electronic devices, • Energy systems

3

The most commonly used 3D printing techniques are listed in Table 1.1. Specifically, fused deposition modeling (FDM) is widely adopted [1] by melting filaments/wires of thermoplastic polymers (such as ABS and PLA) through a hot nozzle followed by natural cooling and solidification to build structures [2, 3]. Key application areas range from robotics [3, 4] to microfluidics [16] with new efforts to include composite filaments by embedding ceramic or metal particles. Several drawbacks of this method include resolution, choice of materials, surface finish, and porosity. For example, the use of thermoplastics and thermoplastic composites results in limitations on mechanical and chemical properties [17]. The printing resolution depends on the nozzle size as well as the viscosity and flow characteristics of the filament. Surface finish and porosity depend on the z-axis movement control and the adherence between layers.

Direct ink writing (DIW) is similar to FDM such that a viscoelastic fluid (“ink”) flows through a nozzle under an external pressure source. The ink is selectively deposited by wetting the surface due to the gravitational force. The ink solidifies by either going through a sudden reduction in stress, phase change, solvent evaporation, polymerization (can be continuous or initiated by an external stimuli) or a combination of these effects [17]. For example, researchers have utilized DIW hydrogels for soft robotics, drug encapsulations, and touch sensors [18], as well as ceramics for optics [19] and cellular structure applications [20]. By tailoring the viscoelastic ink, DIW has good flexibility for different fields. The key drawback is the difficulty in making voids or overhanging structures, such that the structure must be self-supporting unless a sacrificial material can be incorporated.

Powder-bed based systems such as selective laser sintering (SLS) and electron beam melting (EBM) are techniques which use a high-power sources to irradiate the target powder bed [3, 11]. SLS uses high-power lasers at specific wavelengths to selectively irradiate (heat and sinter) a target powder bed such as metals, polymers, ceramics, and cement, whereas EBM uses an electron beam for irradiation to construct metal structures [3,10,22]. The sintering process occurs either through chemical or mechanical effects, allowing for fast solidification compared to FDM or DIW systems to create structures with bulk-like material properties [23]. Since the object is always surrounded by powder, overhanging structures can be created without requiring sacrificial materials [8]. Structures such as turbine blades, engines, brakes [24], cement houses [3], prosthetics and implants [25–27], and high frequency devices such as waveguides [28] have been demonstrated. The high temperature processes limits the material selection to metals with high thermal conductivity, whereas polymers for SLS processes are limited to thermoplastics [17]. Another key drawback is the surface finishing roughness, which is related to the powder size and the porosity of fabricated structures [21, 22].

Inkjet printing, or multi-material jetting, is capable of printing photopolymerizable resins [31] by selectively placing pico-liter droplets on a build plate solidified using a UV light source. Compared to FDM and DIW, inkjet printing can achieve better surface quality using microdroplets as well as

print overhanging structures and channels using sacrificial materials [17] for applications in microfluidics [31] and structural components [32]. However, expensive commercial printers and proprietary resins are key limitations. Recently several research groups have started developing their own piezo or acoustic inkjet nozzles and their own materials to expand the use of this technique [33,34].

Different stereolithography or vat polymerization techniques are called light-based 3D printing techniques in this paper, such as: stereolithography (SLA), two-photon polymerization (2PP) [35,36], digital light processing (DLP) [37–40], continuous liquid interface production (CLIP) [41], and volumetric 3D printing [42–44]. These techniques use photo-curable resins that solidify through a photochemical reaction. In SLA, DLP, and CLIP printing, the first layer is solidified on the build plate and proceeding layers are stacked and solidified on the preceding layer. In 2PP, the three-dimensional structure is formed by localizing the polymerization area and focusing the photochemistry to ensure higher resolution. This is achieved by using a chemistry that starts polymerizing using the energy from two photons instead of one. Volumetric 3D printing directly prints structures in three-dimensions by using a rotating vat and an index-matching resin. By projecting thousands of distinct images of the object taken from specific angles and continuously alternating them during rotation allows objects to be built. Contrary to other methods where the 3D structure is built by 2D layers, the object is created directly in 3D.

Material selection and design for additive manufacturing depend mostly on application and fabrication method, including a large spectrum of materials such as hydrogels, thermoplastics and thermosets, metals, and ceramics as well as a combination of these materials. Depending on the additive manufacturing method, adjustments to the design might be necessary in order to achieve successful prints. For example, hydrogels (Figure 1.1a-e) have been the material-of-choice for researchers focusing on biological applications such as organs [36], tissues, scaffolds and other 3D structures [16], microfluidics for point-of-care applications [45], soft robotic structures [37] for large deformations/drug encapsulations [46–48], and swimming robots for drug delivery [49]. A 3D volumetric printing method is used to create a hydrogel ear (Figure 1.1c) [50], and a 4D biomimetic inkjet printing with a temporal change in the structure is used to create complex geometries (Figure 1.1d) [51]. This technique is unique to deterministically define the elastic and swelling anisotropies. The soft nature of hydrogels and chemistry tuning process made it possible for required material properties.

Figure 1.2: All figures adapted with permission. **(a)** (left) the (3,10) torus knot, and (right) interpenetrating Hilbert curves entangled within hydrogel (20 wt % PEGDA, 6 kDa). Scale bars 3mm [52]; **(b)** As printed “Touchdown the Bear” mascot of Cornell University with hollow center (left) before (right) during the manipulation. Scale bar 10mm [53]; **(c)** Volumetric bioprinting of hydrogel. The inset in shows a stereomicrograph of the actual printed hydrogel, stained with alcian blue to facilitate visualization. Scale bar 2mm; **(d)** Flower geometries created via biomimetic 4D printing composed of bilayers oriented with respect to the long axis of each petal, with time-lapse sequences of the flowers during the swelling process (bottom panel). Scale bars, 5 mm, inset = 2.5 mm [54]; **(e)** Optically and sonically camouflaged hydrogel swimmers fabricated using a 3D printed mold casting process [55]; **(f)** 3D printed triboelectric energy harvester fabricated using elastomeric polyurethane on the Carbon3D DLP system. (left) conceptual drawing of a multi-layer device, (right) actual device as compared with a U.S. penny [56]; **(g)** A 3D printed microfluidic device to create 15 distinct different mixtures from 3 different inputs. Device was fabricated using the multijet 3D printing. US dime for scale [57]; **(h)** A robotic hand fabricated via fused deposition modeling [58]; **(i)** Multi-material grippers fabricated by projection stereolithography using shape memory materials. Top image shows the as-printed geometry which then undergoes programming and it can return to its original shape by increasing temperature [39]; **(j)** EMB3D printed octobot with a soft controller prefabricated inside [59]; **(k)** High force soft actuator fabricated via fused deposition modeling. Right picture shows the pneumatic actuator lifting a 3.2 kg chair; **(l)** A 3D-printed, functionally graded soft robot powered by combustion. 3D printed part with stiffness gradient - Young’s modulus spanning 3 orders of magnitude [60]; **(m)** Electron Beam Melted thin-walled Titanium implant. (left) Implant fit was tested on a replica bone. (center) The implant was placed surgically to evaluate bone response. (right) Implant in a dog with bandage protecting skin-implant interface [27]; **(n)** Stainless steel WR10 waveguides fabricated via direct metal laser sintering. Gold plated waveguide (left) for reference [61]; **(o)** Fully 3D printed metal alloy rocket engine by Relativity [5]; **(p)** Turbine blades designed and manufactured by Siemens engineers installed onto a 13-megawatt gas turbine [62]; **(q)** The GE LEAP 3D printed Fuel Nozzle to be used on the new Boeing 777X commercial airplanes [24]; **(r)** 3D-printed aluminum intake manifold made by Ford. Currently, this is the largest 3D-printed metal part ever installed on a functioning vehicle [63]; **(s)** Freeform sculpture post-heat curing fabricated via direct laser writing of a polymer-ceramic hybrid resin [64]; **(t)** Ceramic saddle surface, fabricated via 4D printing of elastomer-derived ceramics [65]; **(u)** Whiskers-coated alumina sponge by 3D printing. Left image shows the optical image of a printed mesh structure. Center image shows SEM image of multi-fold crossed struts of the sponge. Right image shows surface morphology after whiskers coating [66]; **(v)** 3D printing of piezoelectric metamaterials with complex micro-architectures using PZT coated with photosensitive monomers. Scale bars 300 μ m [67]; **(w)** (Left) SLA 3D printed cork screw. (Right) Micro-lattice formed using self-propagating photopolymer waveguide technology with polymer-derived ceramic resin [68].

Thermoplastics and thermosets have also been at the forefront of 3D printing especially with affordable and widespread FDM systems. The material choice for thermoplastics is quite limited, mostly to ABS and PLA filaments. With the advances in photochemistry and the possibility to print silicones and urethanes using stereolithography and other light-based printing systems, researchers were able to choose from a larger number of materials, such as the elastomeric polyurethane (EPU, a proprietary urethane system by Carbon3D) (Figure 1.1f) [56] for its highly flexible nature. Material jetting and thermoset materials have been utilized to create a multiple inlet-outlet gradient generator (Figure 1.1g) [57] to withstand flow pressures without disrupting the fluid flow profiles. 3D printed functional microfluidic devices [69] and materials in biofabrication [70] have all been discussed previously. Specifically, FDM printing and the use of thermoplastic materials were used to create soft robotic actuators (Figure 1.1h, i, k) [15,58], and EMB3D 3D printing method were used to combine silicone structures with infills for soft robotic actuators (Figure 1.1j) [71]. Novel photo-chemistries have also been utilized to create structures with changing material properties (Figure 1.1) [60]. This route of creating materials with changing mechanical properties and using this feature in designing actual structures further expands various possibilities of additive manufacturing.

On the other hand, the material choice for metals has been limited due to their processing requirements and issues that arise in trying to achieve bulk-like material properties. Researchers have utilized metal-polymer composites, but this approach quickly proved to be ineffective for applications in aerospace, bone-implants and vacuum electronic devices. Titanium, copper, stainless steel, and various aluminum alloys have been printed for different applications [72]. For example, titanium has been the material of choice for implants due to its lightweight, biocompatible and high strength characteristics [22]. One example is the thin-walled Titanium dog paw implants using electron beam melting method in the real-life scenario (Figure. 1.1m) [27].

In application areas where mechanical, electrical, and metallurgical requirements become more stringent, such as aerospace applications, material selection is dictated by the application. Stainless steel WR-10 waveguides has been demonstrated but higher conductivities are needed to achieve better performance (Figure 1.1n) [61]. The oxygen free high conductivity copper powers have been used in the electron beam melting scheme to create high performance WR-10 waveguides, but post-processing such as reducing the surface roughness after the printing process is needed [13], [19–21]. Major advances in the commercialization of metal additive manufacturing for aerospace applications have been demonstrated by *Relativity*, a start-up company based in California, USA for a proprietary metal additive manufacturing method to fully 3D print metal alloy rocket engines (Figure 1.1o). According to the company, this method not only decreases costs and reduces manufacturing waste, but also enables off-planet fabrication of metal alloy parts for space missions [5].

Apart from aerospace and high frequency electronic applications, harsh environment applications such as turbines, engines and their parts (i.e. turbine blades, fuel nozzles, etc.) also require precision fabrication with exceptional material properties [73]. Siemens Inc. has created multiple additive manufacturing factories for the sole purpose of high performance metal alloy turbine blades (Figure 1.1p) [74]. General Electric has printed metal fuel nozzles, which will become one of the first printed parts installed on a commercial airliner (Figure 1.1q). Ford has shown that 3D printing can be used to create high performance engine parts by 3D printing an aluminum intake manifold (Figure 1.1r) [63]. These recent advances show the capabilities of additive metal manufacturing and the material selection to meet industry needs.

The last set of engineering materials that can be 3D printed are ceramics commonly used in different areas, such as abrasion resistive applications in car brakes and high precision optical devices in lenses. For example, hybrid freeform structures using a polymer-ceramic composite resin with near-submicron features have been demonstrated (Figure 1.1s) [64] and a 4D printing technique with elastomer-based ceramic composite resin has been utilized to create lattice structures to be further deformed under heat (Figure 1.1t) [75]. A ceramics digital light processing printing technique has been used to create ceramic lattices coated with alumina particles to separate oil from water (Figure 1.1u) [66]. Lastly, piezoelectric structures using surface-functionalized piezoelectric nanoparticles can be dispersed in ultraviolet-sensitive monomers to be sculpted into 3D structures by the near-ultraviolet light (Figure 1.1v) [67].

One critical design obstacle has been building multiple materials in a single structure under an integrated manufacturing process, such as the capability to print devices that have conductive parts embedded in the nonconductive structural materials [16]. Different approaches have been proposed as shown in Figure 1.2 such as: direct ink writing and fused deposition modeling for wearable gloves made of silicone with embedded strain sensors for detecting finger motions (Figure 1.2a) [76]; a multi-core-shell structure using direct ink writing of ionically conductive fluids and insulating silicones for strain-dependent capacitive sensors in a wearable system (Figure 1.2b) [77]; and a material jetting technology to create polymer structures with internal cavities filled with a conductive filler material to function as electrical components for simple electronics circuit. This method was used in creating a “smart milkcap” which could detect the change in frequency of an LC circuit to sense whether milk had gone bad. Another example is a specialized ink writing technique to conformally deposit conductive material on 3D printed polymer surfaces [16] for 3D printed antennas (Figure 1.2e).

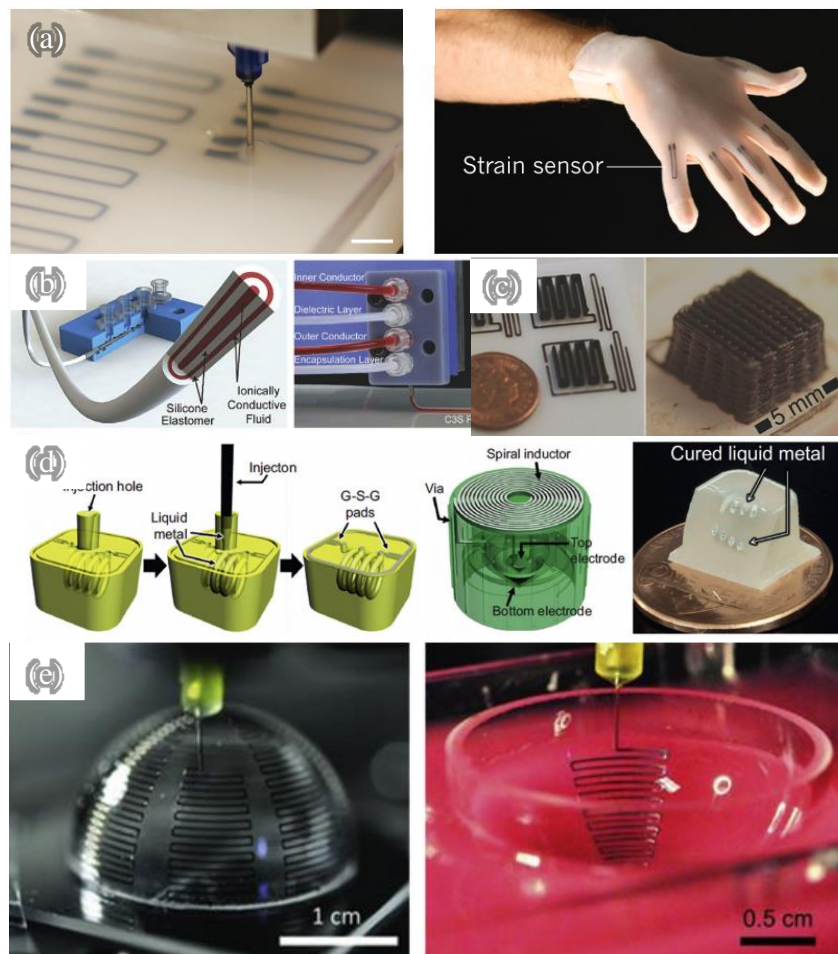


Figure 1.3: (a) Silicone gloves with embedded resistive strain sensors. Conductive carbon grease is extruded into a viscous silicone pre-polymer matrix. Changes in resistance can be used to monitor hand motions and gestures [76]; (b) Multi-core-shell direct ink writing of ionically conductive fluids and insulating silicone elastomers as strain-

dependent capacitive sensors [77]; (c) Responsive graphene oxide sheets via DIW 3D printed. Drying and thermal reduction can lead to ultra-light graphene-only structures with restored conductivity and elastomeric behavior [78]; (d) Electronic components and systems fabricated by the combination of MJM and the liquid metal paste filling process [79]; (e) Conformal printing of electrically small antennas on convex (left) and concave (right) surfaces [80].

1.3. Current Limitations and Post-Processing Influences

Most structures from 3D printing processes require post-printing processes to create functional and working devices as shown in Figure 1.3. The four major post-processing methods are: (1) removal of the support structure and secondary curing steps [5, 41]; (2) coating of surfaces for functionalization and/or protection [40, 73]; (3) polishing and surface roughness improvements [21, 74]; and (4) treatments for changing material properties and structure shapes [8, 11, 19, 20, 74, 75].

The removal of support structures, cleaning, and secondary curing steps are processes required in nearly all 3D printing systems. Systems such as fused deposition modeling and material jetting make use of support materials to stack layers and to create void structures and/or overhanging structures. To access these voids and overhanging structures, the support materials are removed, or dissolved. This technique has been widely used in the microfluidics area to create fluidic channels such as a three-layer microfluidic mixer with 3 inputs and 15 distinct outputs by the material jetting 3D printing process and the removal of the support material (Figure 1.1g) [57]. Secondary curing steps are utilized in polymer chemistries in which the first polymerization reaction, generally UV curing or heating, leads to the formation of polymer chains. However, unreacted monomers still remain in the system and they are removed either using temperature or UV exposure [41]. This secondary heating steps can also be used to change the material properties or the shape of the 3D printed structures to achieve their final forms. A multi-step thermal process has been utilized to change the optical properties of the direct sol-gel glass composites to SiO₂ (Figure 1.3d) [19] and the sequential self-folding structures realized by the thermal activation of spatially-variable patterns have been 3D printed with digital shape memory polymers for different shape memory behaviors (Figure 1.3e) [85].

The coating of 3D printed surfaces involves various deposition techniques to create functional devices and there have been various demonstrations. Conformal Parylene AF4 deposition has been used to create a flexible triboelectric energy harvester (Figure 1.3a) [56]; electropolymerization has been utilized to functionalize the surface of a lattice structure made via material jetting to create an ethanol sensor (Figure 1.3b) [86]; and a microfluidic reactor using the material jetting technology has been functionalized by loading antibiotics (Figure 1.3f) [81]. Finally, the requirement of better surface finish and surface roughness improvements have been widely recognized in additive manufacturing due to application specific surface finish requirements and aesthetic reasons. Even though many advances have been made in fabricating high-quality surfaces, processes based on powder systems often have high surface roughness and require post-processing. The issue with having high surface roughness is that during conversion or transportation of energy high losses can be incurred. Specifically, surface finish issues become very important for high loss systems such as high frequency waveguides as well as structures

which are used for engine and turbine parts. I will cover issues relating to energy losses in high frequency waveguides in chapter 3; however, other application specific losses will not be covered in the thesis. The losses that occur due to surface texture and roughness in general are directly related to the manufacturing or fabrication process that is used. Different methods have been developed to smoothen surfaces that have been fabricated using conventional methods and these methods, such as grinding and sanding have been applied for 3D printed metal parts; however, some structures, such as enclosed channels, require novel polishing methods. To this end researchers have focused on exploring the application of already existing internal surface polishing methods. Such examples include vibratory bowl abrasion and ultrasonic abrasion finishing[82].

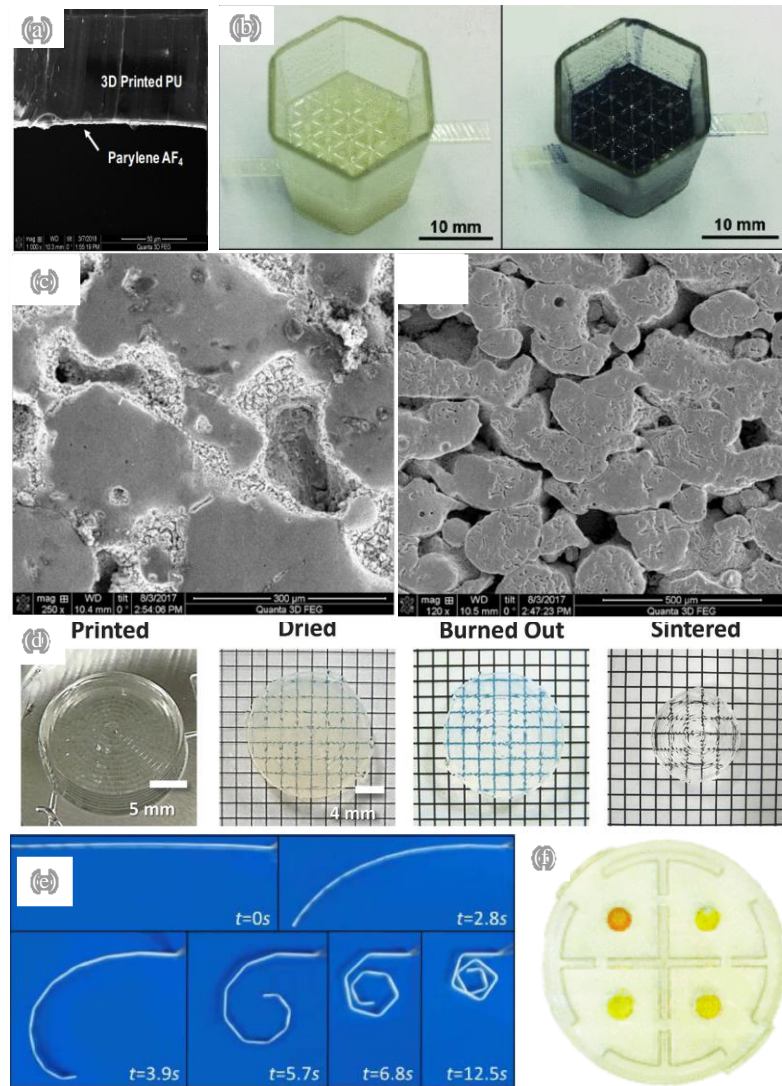


Figure 1.4: (a) 3D printed energy harvesting structures made by polyurethane using a DLP printing system coated with Parylene AF4 to functionalize the surface via a post-printing process [56]; (b) 3D printed ethanol sensor fabricated using the polyjet printer. The surface is functionalized by post-printing with polyaniline using electropolymerization [86]; (c) Oxygen free high conductivity copper WR10 waveguide surface fabricated via electron beam melting. (left) As printed sample with rough surface. (right) Polished surface post-printing using magnetic abrasive polishing [30]; (d) Direct ink writing of sol-gel and glass components at various stages. By

various heating steps in post-processing can be converted to SiO₂. [19]; (e) Sequential self-folding structures by 3D printed digital shape memory polymers [85]; (f) Antibiotic loaded chambers and the color changing reaction taken by a smart phone camera (antibiotic Ampicillin, Kanamycin, Ciprofloxacin, and Sulfamethoxazole are loaded in wells) [81].

1.4. Future Prospects of 3D Printing

Many applications previously thought impossible using additive manufacturing have been realized using post-processing techniques. Some techniques have been used to improve material properties while others have added functionality to 3D printed structures. However, technical challenges still remain, some of which are: (1) it is still difficult to fabricate structures with functional layers within polymer layers; and (2) It is highly important to be able to lower the surface roughness of 3D printed parts. It is my belief that the true potential of 3D printing can only be realized once functional layers can be integrated into the 3D printing process via a multi-material printing process to reduce (if not eliminate) the need for post-processing while also reducing the surface roughness through a finer printing process

1.5. Thesis Structure

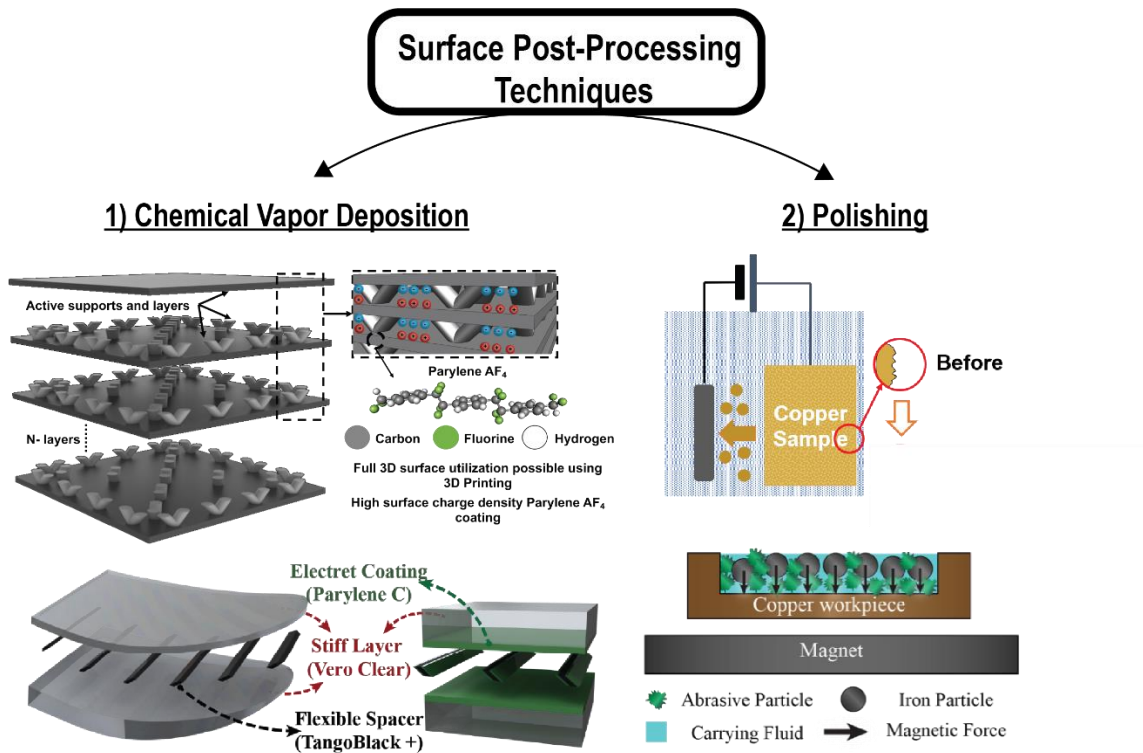


Figure 1.5: Thesis goals and structure. (1) Chemical vapor deposition of Parylene for piezoelectret energy harvesters. (2) Polishing methods for metal 3D printed vacuum electronic devices.

The overall goal of this thesis, illustrated in Figure 1.5, will be to tackle the current technical challenges mentioned before. The second chapter will first focus on developing a simple post-processing technique to create functional 3D printed devices that can be used as self-powered sensors and energy harvesters. The chapter will then introduce an energy harvesting 3D printed shoe sole which can be the basis for many different wearable applications. Finally, the second chapter will finish by introducing future applications and directions that can be taken further to benefit from the simple fabrication technique developed through the chapter. The third chapter will focus on the second technical issue concerning the surface roughness of 3D printed parts. The chapter will specifically focus on electron beam melting and vacuum electronic devices which were used as the application area for the surface polishing technique that was developed. The chapter will introduce electron beam melting and vacuum electronic devices (specifically waveguides) and will then construct a theoretical and computational background for the proposed surface polishing technique. The chapter will finally use the developed technique on a 3D printed copper waveguide to demonstrate its polishing performance. The fourth chapter will summarize the key results from chapters 2 and 3 and will provide improvements and exciting applications that can be investigated in the future.

2. Chapter 2: 3D Printed Piezoelectret Devices via Chemical Vapor

Deposition of Parylene

2.1. Introduction

The aim of this chapter is to tackle the issue of creating functional 3D printed surfaces and devices. To achieve this goal, a versatile post-fabrication process in the form of chemical vapor deposition of different parylenes on to 3D printed polymer surfaces is developed. This process is utilized for different 3D printing techniques, which can be used to produce structures with various material properties. In this chapter, these different 3D printing techniques are used to fabricate structures for two different applications: (1) a multilayer piezoelectret energy harvester, (2) a shoe-sole piezoelectret energy harvester.

To understand the need for using 3D printing to create structures for electret-based applications, the working principle behind piezoelectret devices, the materials, and fabrication techniques used are investigated. The current drawbacks especially for the fabrication techniques used in making piezoelectret devices are examined and specific application examples are provided.

2.1.1. Overview of Piezoelectret Devices, Fabrication Methods, and Applications

The rise of wearable electronics has resulted in significant impacts on society in various fields such as healthcare, entertainment, personal communication, and environmental monitoring [87–89]. With the increase of these devices in our daily lives, cheap and renewable energy sources have become increasingly important [90]. This has led to the developments of different energy harvesting schemes to create self-sufficient systems. Energy harvesting systems as self-sustained power sources are capable of capturing and transforming energy sources from the environment into electrical energy, providing an alternative to conventional batteries [91–95]. In general, the kinetic energy of an object can be transformed into electrical energy through electrostatic [96–98], electromagnetic [99], piezoelectric [100–103], and triboelectric mechanisms [99,104,105]. Among various types of energy harvesters reported in literature, triboelectric nanogenerators (TENGs) based on the piezoelectret effect combining triboelectricification and electrostatic induction effects have shown unique advantages in terms of high energy conversion efficiency, diverse material selection (Table 2.1) and relative ease of fabrication [106].

Table 2.1: Material Selection and Charging Potentials [107]

More positively charged (+)	▲
Fur, Hair	Silver
Glass	Gold
Mica	PET
Nylon	Polystyrene

Lead	Acrylic
Silk	PVC
Aluminum	Silicon
Paper	Polyethylene
Rubber	PTFE
▼	More Negatively charged (-)

The working principle of TENGs relies on the change in the quasi-static charge state of two oppositely charged surfaces known as electrets. This change occurs whenever the surface is displaced with respect to the other, causing the structure to reach a new quasi-static charge state. This new state is reached by moving electrons from one electrode to the other as shown in Figure 2.1. By repeating this motion, TENGs can convert mechanical motion into electrical energy creating a renewable energy source.

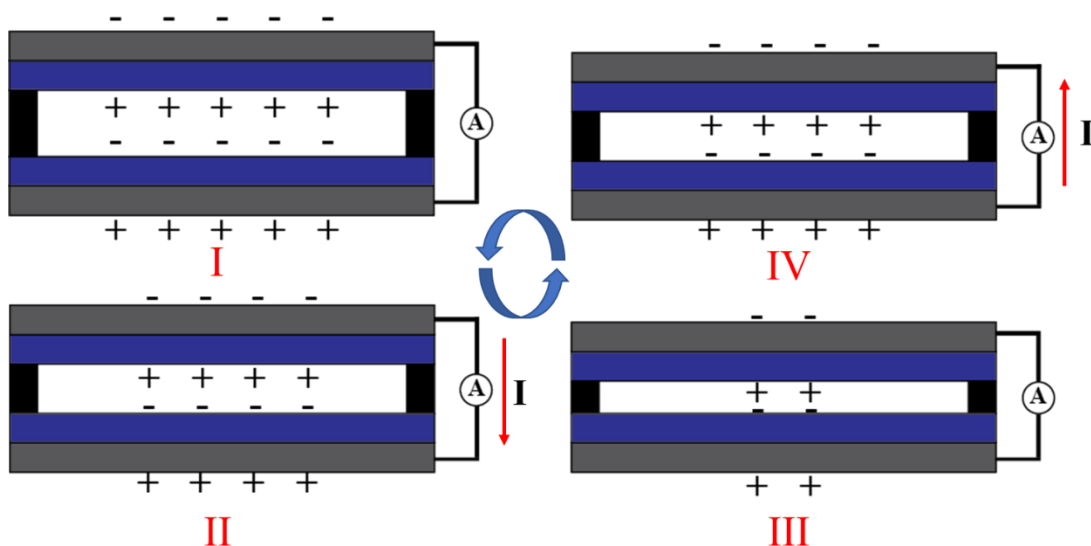


Figure 2.1: Working Principle of piezoelectret devices.

Different self-powered sensing systems ranging from gas and chemical detection to pressure/tactile monitoring as well as e-skins have been developed using the TENG principle [108]. Various sources of mechanical energy such as wind power, human motion, and acoustic waves have been used for electrical energy generations and some of them are illustrated in Figure 2.2

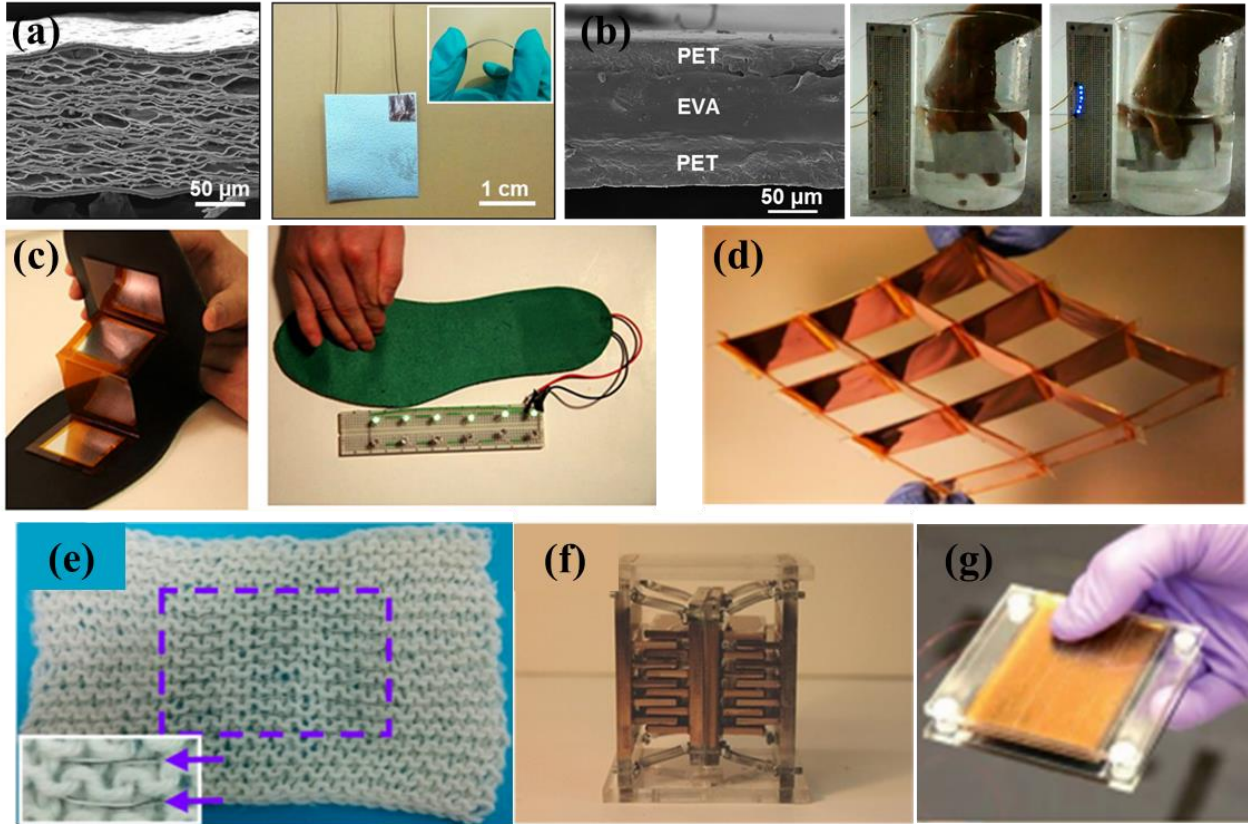


Figure 2.2: Typical photographs of some piezoelectric energy harvesting devices: (a) a cellular PP device for finger tapping [109]; (b) a sensor/energy harvester under harsh environment [110]; (c) a shoe insole energy harvester [111]; (d) a 3D stack to harvest energy from human motion [112]; (e) a fabric-based harvester for harvesting body motion energy [113]; (f) a 3D stack energy harvester for vibration energy [114]; (g) a foot/hand pressing energy harvester [115].

However, the focus of technological development has been in increasing performance and less on the manufacturability. Recently, various strategies have been proposed to improve the output performance as well as the manufacturability of TENGs, including functional material synthesis [116,117], nanostructured surface modifications of contact polymer materials [118–120], smart designs with arch-shaped plates [121,122], multilayered structure optimizations, and 3D printing [56,114,123–126]. Among these approaches, the nanostructured surface modification of contact polymer material has a complicated fabrication process, which is unfavorable for large-scale batch-fabrication and long-term durability [127]. The auxiliary architectures, designed to support the periodical contact and separation operations make the whole device bulky and difficult to be integrated with wearable or biomechanical microsystems [114,123]. Specifically, the currently used rigid designs of TENGs usually have restricted operation frequencies and directions, making them difficult to be adapted with vibrations of irregular, random, and low frequency characteristics, such as human motion [128–131]. Also, the output power of TENGs is quadratically proportional to the surface charge density, while the electrostatic induction of TENGs is severely affected by the effective surface charge density of different materials [131]. Finally, the 3D printing approach has focused on printing structural components to be assembled

with thin-film electret materials for functional devices without fully utilizing the full potential of the 3D printing process [132–135].

In order to advance the current state-of-art, a 3D printed, multi-layered and highly flexible TENG with thin film Parylene electret is proposed and demonstrated to have several unique advantages as shown in Figure 2.3, including: (1) TENGs with the stacking multilayer structure can be easily constructed using 3D printing to create complex, flexible, and deformable energy harvester based on facile and low-cost fabrication processes; (2) the increase of effective surface area can significantly amplify the capacitance variation of electrostatic induction to increase performances. As such, energy harvesting can be achieved without using labor-intensive fabrication processes and the light weight, long-term durability and excellent flexibility of the TENG devices can be easily integrated to wearable electronics for biomechanical energy harvesting.

2.2. 3D Printed Triboelectric Energy Harvesters via Chemical Vapor Deposition of Parylene AF4

In order to construct a multi-layer piezoelectret device, there are several fabrication approaches but most of these techniques are labor intensive. 3D printing is an exciting alternative to build complex three-dimensional structures with ease. Combined with post-processing methods, such as chemical vapor deposition to functionalize the surface of the 3D printed structures, 3D printing can potentially reduce fabrication costs and complexity. The concept of multilayer piezoelectret devices based on 3D printing and post-processing is developed in this section. Computational modeling is used to show the impact of having additional layers on the device performance for the device optimizations. The fabrication method is developed and characterized and the energy harvesting performance of the prototypes under different compressive force conditions is investigated.

2.2.1. Device Design & Working Principle

The main device design principle is to add planar layers on top of each other by adding supporting beams in between. These beams are designed to deflect as much as possible when the device is under a compressive load while being strong enough to resist the tensile forces that occur during the printing process. Figure 2.3 illustrates the concept for a device with the N-layer structure. Once the 3D printed structure is functionalized, it is charged to impart positive and negative charges on opposing surfaces in each layer. However, unlike conventional electret devices, the charges are also distributed on the support beams which are functionalized to increase the overall active area and performance. However, the main increase in performance is expected to be due to the softer spring constant of multilayer devices compared to single layer ones.

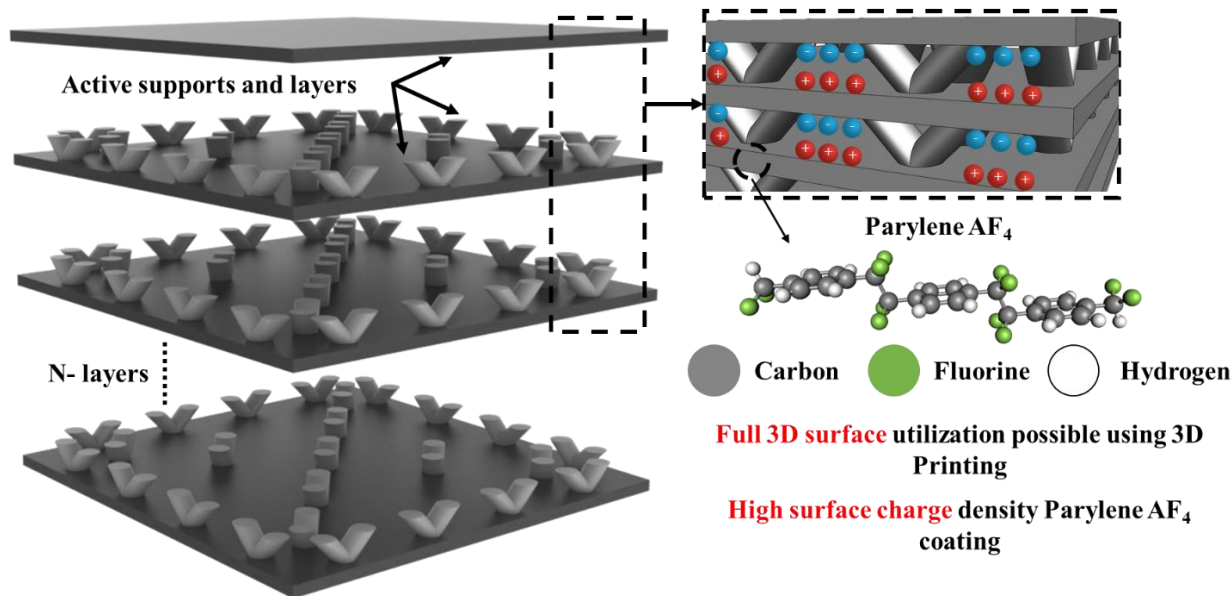


Figure 2.3: Conceptual drawing of a multi-layer 3D printed triboelectric energy harvester (TEH) with high surface area by means of the 3D structure and the high surface charge density layer using the conformal coating process of Parylene AF4. The V-shaped supports are designed to separate the layers. A corona charging process is conducted to provide high surface charges.

The working principle is similar to other electret devices. By bringing opposing surfaces closer and then releasing the structure, the quasi-steady charge state experiences change to drive (push) electrons from one electrode surface to the other through the closed circuit as illustrated in Figure 2.4 to light up an LED. Initially there is no electron flow (current) through the LED since the surfaces are in a quasi-steady state. Once the device is compressed, this charge state is disrupted and in order to achieve a new quasi-steady state, electrons flow to power the LED. Once the compressive force is released the system goes back to its original state.

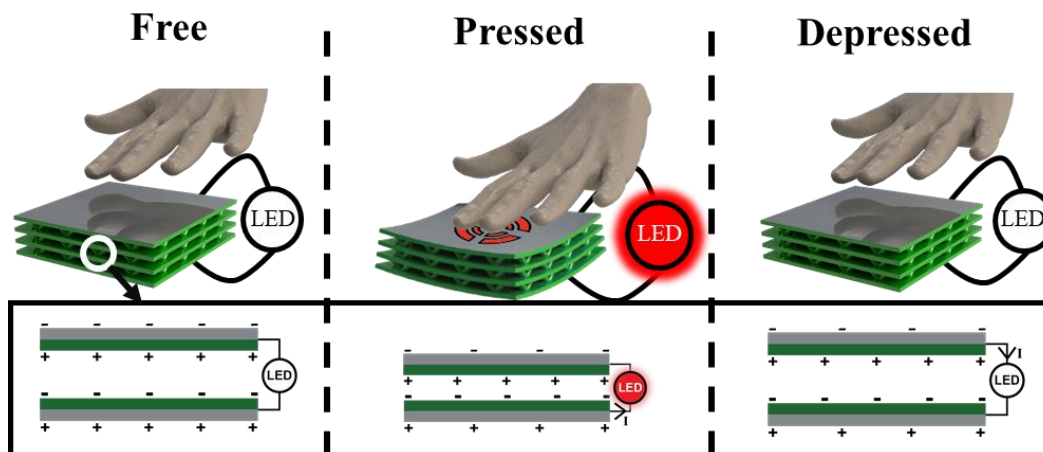


Figure 2.4: Main working principle of piezoelectret energy harvester. From left to right, the device is shown first in its original configuration after the corona charging step. The charges are in a quasi-static equilibrium. Then the top layer of the device is compressed, and the equilibrium conditions change, forcing electron movement from one electrode to the other to create the electrical current. As the device is released, it returns to its original configuration.

The surface charge density, can be calculated as [105]:

$$\sigma_o = \frac{\varepsilon \sum_{i=1}^n \sigma_i}{n \left(\frac{D_1}{D_2} + \varepsilon \right)} \quad (1)$$

where ε denotes the relative dielectric constant of the active electret layer; n is the number of layers in the structure; and D_1 and D_2 are the thickness of the electret material and gap in between the layers, respectively. From equation (1), it is observed that the thickness of the electret material, the gap distance between layers, and the deformation of the layers will affect the overall performance of the system. To get a better understanding of how the structure deflects, simple computational analyses can be conducted. For this, a static linear elastic compression model using COMSOL Multiphysics is used to show the deflection profiles.

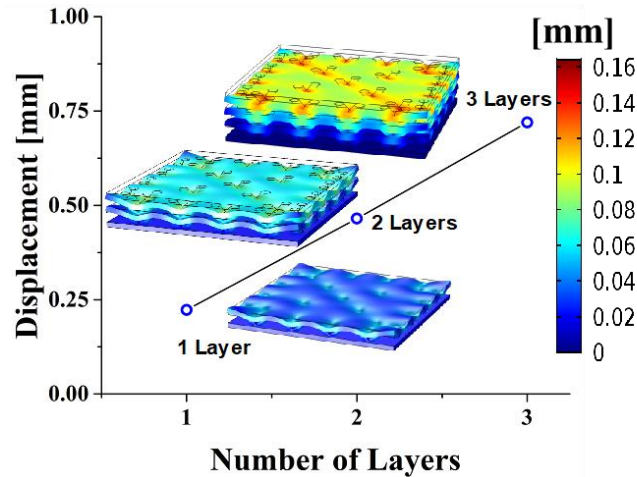


Figure 2.5: COMSOL simulations of the displacement under a force of 3-Newton for devices with single, double and triple layers.

From the deflection profiles seen in Figure 2.5, as the number of layers increase, the cumulative displacements of each design increases. This indicates that at the very least, a three-times increase in performance is expected for the triple-layer device compared to the single-layer one due to the softening of the overall spring constant.

2.2.2. Fabrication and Characterization

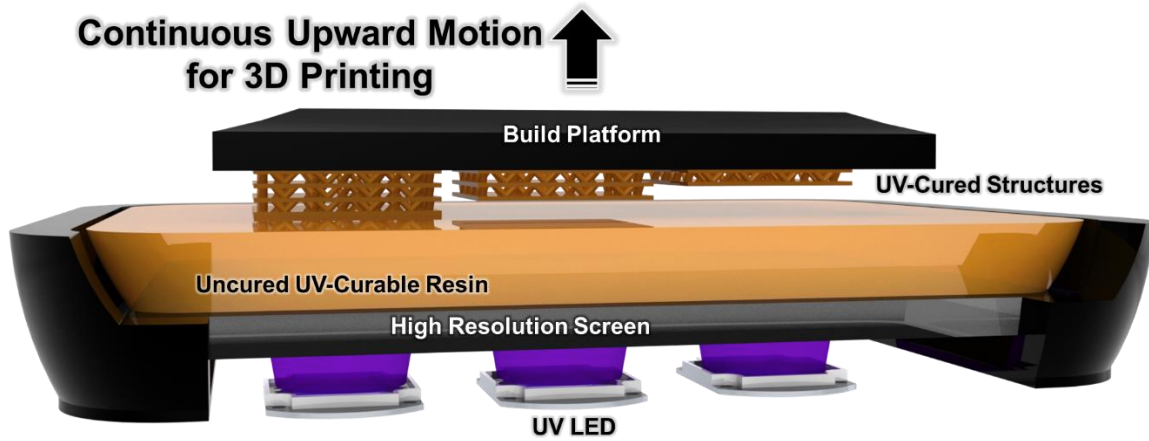


Figure 2.6: The fabrication details of the stereolithographic 3D printing process with the continuous liquid interface printing for the energy harvesters. The UV LED is applied from the bottom of the system and the high-resolution screen is used as the optical mask. The UV-curable resin is illuminated by the UV light and the cured structure is pulled by the build platform. Various 3D printed devices can be made in the same batch.

In order to create the three-dimensional TEH structures optimized for maximum deformation, the 3D printing process based on stereolithography is utilized. Even though many of the 3D printing techniques covered in Chapter 1 can be used to create these structures, DLP-based stereolithography is chosen due to the material selection offered and ease of access to the printing system. In this study elastomeric polyurethane (EPU) [136] is used to fabricate a highly flexible and compressible device.

Figure 2.6 illustrates the fabrication process by the stereolithographic 3D printing process using a commercial Carbon3D M1 printer [137]. A UV-light source (385 nm) irradiates the uncured photopolymerizable polyurethane resin and a high-resolution screen is used to project the required shape on to the resin to solidify it. This process is repeated many cycles until the desired structure is fabricated. As such, multiple layered devices can be created using this process for high design flexibility. Furthermore, numerous devices can be printed together to reduce manufacturing time.

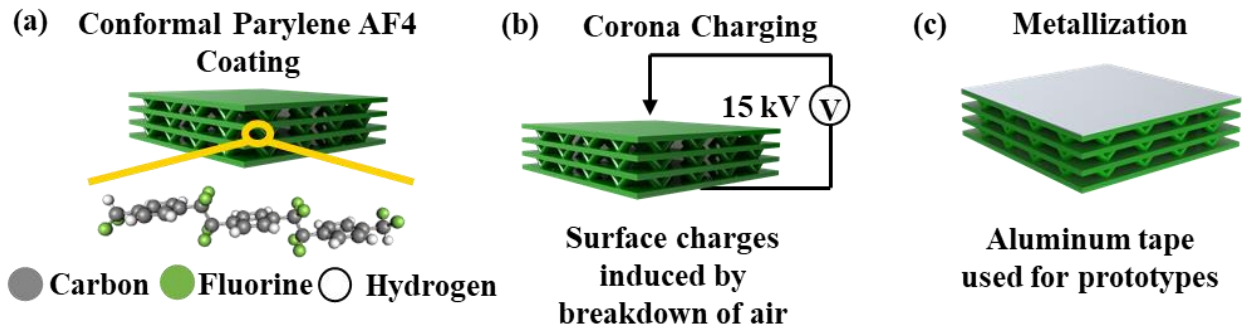


Figure 2.7: (a) The conformal Parylene AF4 coating process; (b) the corona charging process; and (c) metallization for the electrodes.

After the structures are printed, a conformal layer of Parylene AF4 is deposited as shown in Figure 2.7a. In the prototype fabrication, a total amount of 4 grams of Parylene AF4 is coated using Specialty Coating Systems' Parylene Deposition System 2010. This amount is determined by first conducting a characterization process to determine how much material is needed to achieve a certain thickness of coating. The resulting conformal layer can functionalize the surface of the polyurethane structures to capture a large amount of surface charges due to the high surface charge density of Parylene AF4 ($3.7\text{mC}/\text{m}^2$ [138]). This high surface charge density is due to the fluorine atoms present in the polymer's structure [139]. Surface charges are then induced in between the layers using the corona charging technique. A high voltage power supply is used to deliver 15 kV to the tip of the corona needle (Figure 2.7b). This high voltage is used to produce a high electrical field to break down the air molecules in between the Parylene layers, which then captures these charges. Lastly, the outer top and bottom layers are metallized using an aluminum tape (Figure 2.7c).

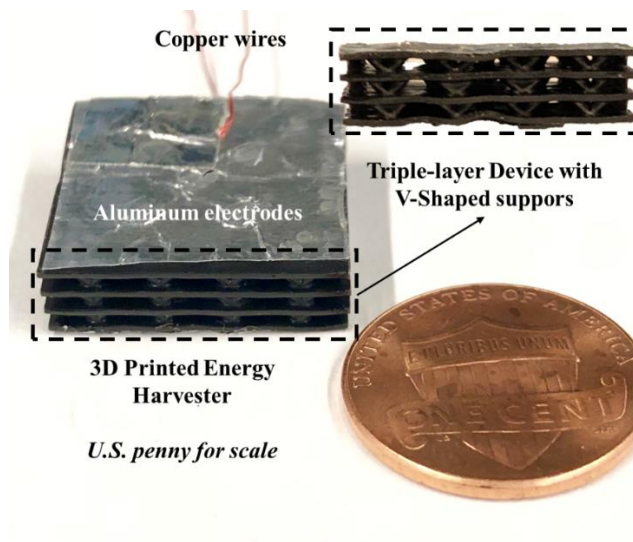


Figure 2.8: Optical photo of an actual device as compared with a U.S. penny. The top electrode has a coating of aluminum.

Figure 2.8 shows the fabricated prototype device with 3 active layers. Aluminum sheets are used as the electrodes for this device to reduce the number of post-processing steps by eliminating the need for electrode deposition. Copper wires are attached to the aluminum electrodes via another layer of aluminum tape on each side. The side view shows the v-shaped support structures after printing. The overall size of the prototype can be compared to a U.S. penny. It should be noted that the size of the device can be increased within the limits of the 3D printing system. The fabrication process is fully characterized. First, the Parylene coating on the surface is imaged using a scanning electron microscope (SEM) to measure the dimensions of the 3D printed samples and the thickness of the Parylene. Figure 2.9 shows the 3D printed structure that was used for characterizing the spacing, the layer height, and the beam width. Figures 2.9b and 2.9c show the top surface of the 3D printed structures to illustrate the surface morphology.

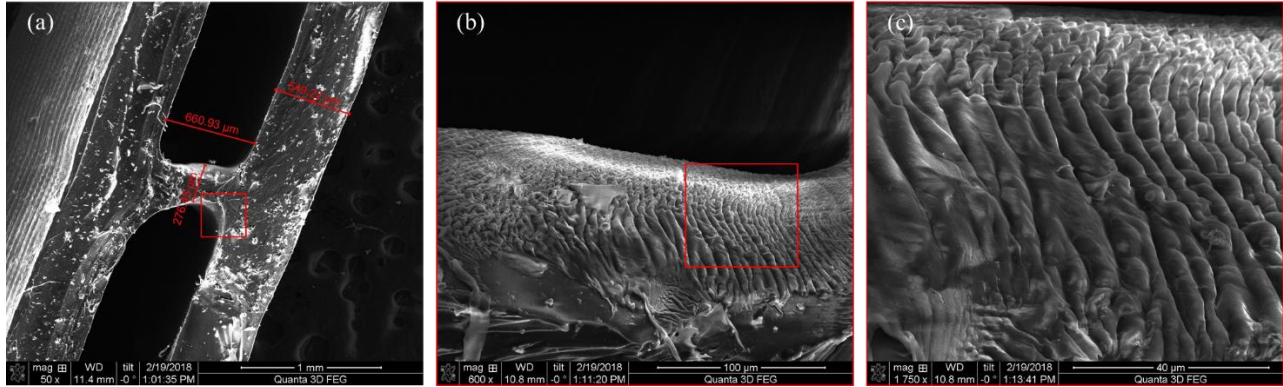


Figure 2.9: SEM image showing different locations on the 3D printed structure. (a) The cross-sectional image shows the area where the support structure connects to the top and bottom layers. The various measurements are also used to compare to the original design. (b) Structure's side surface image showing the striations on the surface indicative of the layer height. (c) A closer view of the side surface in (b).

The uniformity of the coating is examined around the middle of the structure and the sides. A 5cm x 5cm EPU single-layer device with a layer-to-layer separation of 660 μm and 500 μm thick layer height is fabricated. This structure is then cut into 6 equal parts as shown in Figure 2.10a. The thickness of the film is measured under SEM on 3 different points for each side of the samples. The average thickness for each sample is given in Figure 2.10b. It is found that the variation of the film thickness is approximately 30% between different regions and the center region has a thicker coating.

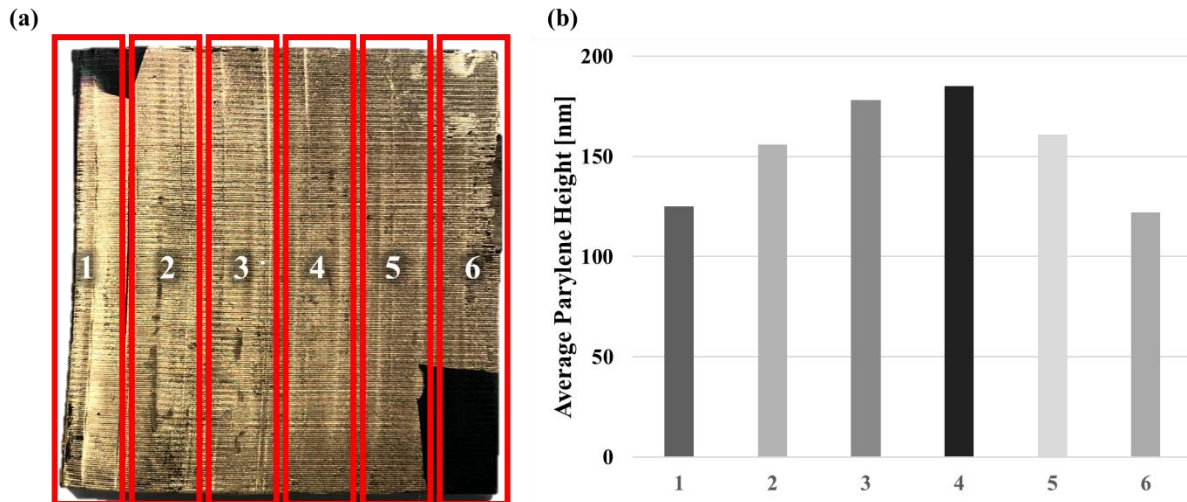


Figure 2.10: Uniformity study of the Parylene deposition on the 3D printed samples. The samples are split into 6 regions and the measurements shown are the average heights taken at 3 different points along each side of the samples.

A 100 nm thick Parylene AF4 layer is coated on the samples for study as shown in Figure 11. Parylene AF4 is nearly 100x more expensive than that of other Parylene materials and additional process control is required since the coating system was not originally designed for this type of Parylene. Also, AF4 is bought from Taiwan and the lead time is 1 month. These restrictions resulted in the decision to have a very thin layer of AF4, which reduces its expected performance since the overall charge density is dependent on the coating thickness as shown in Eqn. 1. Since

it is expensive to coat AF4 to a thickness of 5-10 μm (similar height to conventional thin film electrets), other Parylene types become more attractive for the prototype fabrication.

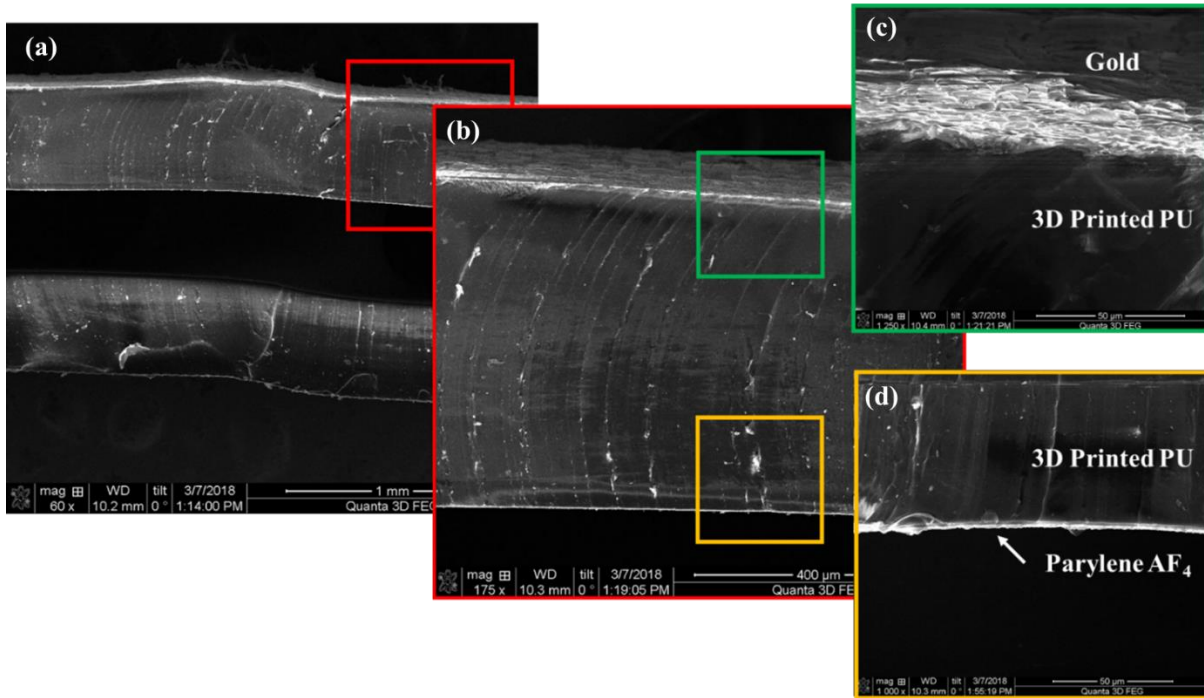


Figure 2.11: Cross-sectional view of the Parylene coated 3D printed structure. (a) Zoomed out image showing both top and bottom layer. (b) Zoomed in image showing the top layer which has metal layer on the top and Parylene layer on the bottom. (c) The metal layer (gold) and 3D printed polyurethane is shown. (d) 3D printed polyurethane coated with Parylene AF4 is shown.

The structures are then charged by the corona charging process and the samples are monitored for a month to observe the decay of the surface charge density as shown in Figure 2.12a. It should be noted that the samples are originally charged for 2 mins at 15 kV and a large decrease in surface charge potential is observed in 20 days, starting at -17 V to approximately -12 V as measured in Figure 2.12b. Compared to other electret materials, the measured surface charge potential is quite low, possibly due to the thickness of the film, the charging time, and the charge leaking process [140,141].

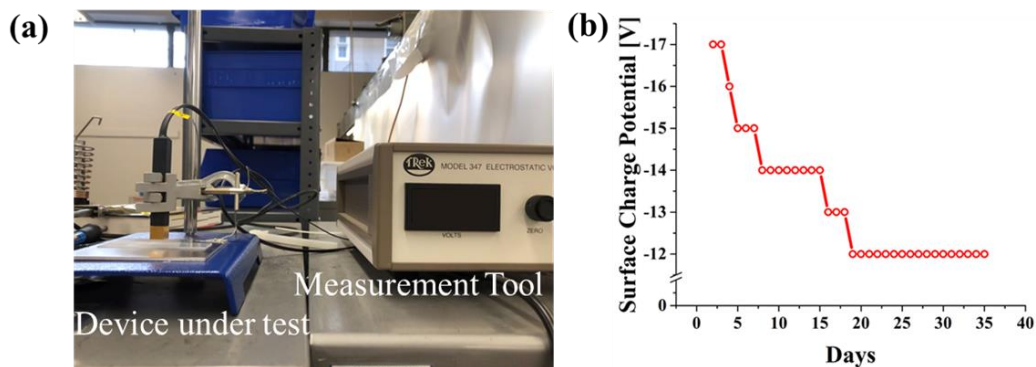


Figure 2.12: (a) Surface charge measurement; (b) Surface charge potential vs. time after the corona charging process. The surface charges is stabilized at -12 Volts.

2.2.2.1. Experimental setup, results, and discussion

The samples are first tested manually by pressing on them to determine whether the fabrication method produces working samples. These initial results can be seen in Figure 2.13 under different frequencies.

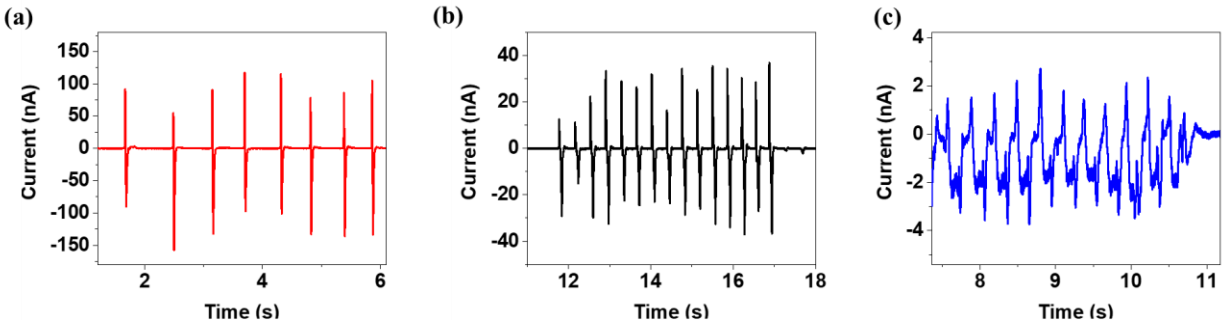


Figure 2.13: Initial performance of samples. Compressive force applied at approximately (a) 2 Hz; (b) 3 Hz; (c) 4 Hz.

Further characterization is conducted to determine the short circuit current (SCC) and the peak power output of the prototypes. These tests are conducted by mounting the devices on a dynamical mechanical test device in Figure 2.14 (ElectroForce 3200, TA Instruments).

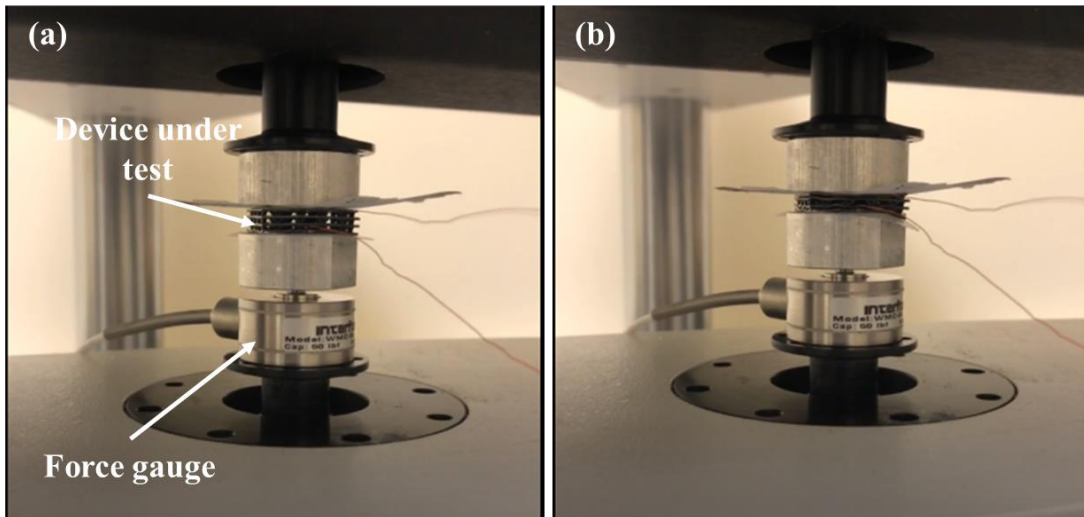


Figure 2.14: Sample attached to mechanical testing setup (a) Uncompressed. (b) Compressed

The top layer of the energy harvesters is displaced under a constant force amplitude actuator at a given frequency. The load exerted onto the harvesters is measured by a load cell placed underneath the bottom layer of the devices. The SCC output of the three different designs (single-, double-, and triple-layer) are compared as seen in Figure 2.15a. The top layers of the devices are compressed with a 3-Newton force applied at 1 Hz and this value is chosen to replicate a potential human interaction at low operating frequency. It is found that the SCC of the triple-layer device is approximately 20 times higher than that of a single-layer device. This observation is not expected since the computational displacement models had shown only about 3x increase in the overall

displacement. The key reason for the large increment is believed to be the increase in the active surface area due to the electret support beams which are not considered in the computational model.

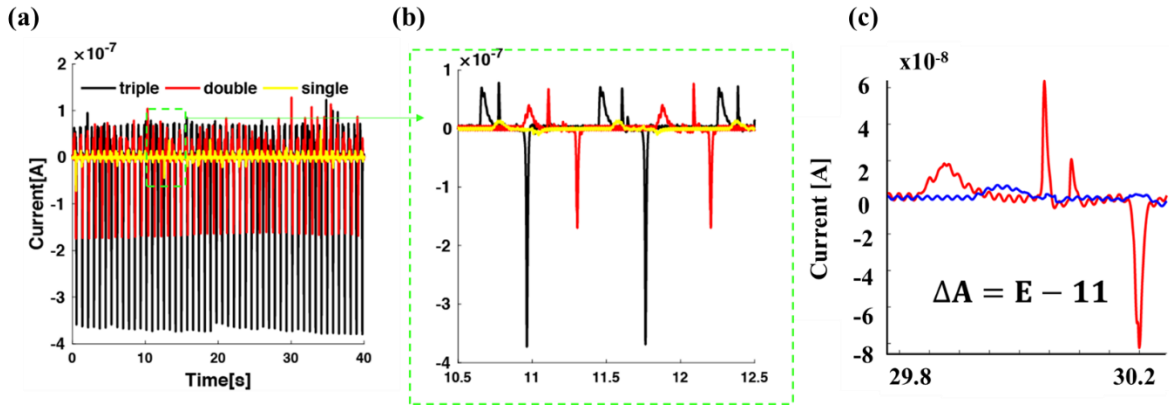


Figure 2.15: (a) Short circuit current output of single-, double-, and triple-layer devices tested separately. (b) A shorter time-frame of the results shown in (a) are shown to highlight the details in output performance. (c) A triple-layer device is pressed on (red) and compared to a free-standing device (blue) to compare the output.

Another interesting observation in these results is that the devices would show multiple positive current peaks (Figure 2.15b). This is believed to occur due to the different activation times of each layer. To test this hypothesis, the total positive and negative charge transferred in one cycle are calculated by integrating the SCC vs time curve for a single cycle. It is seen that the integration yields a net charge transfer of approximately zero which is what is expected from this system indicating that the signal with multiple peaks is a real signal further supporting the conclusion that each layer activates after a certain amount of time has passed as shown in Figure 2.15c.

Finally, the triple-layer device is tested under a 3-Newton force applied at 2 Hz. The SCC curve can be seen in Figure 2.16a. The important thing to note here is that the current is within a stable window and the performance does not degrade with time. The power output of the device is shown in Figure 2.16b with respect to an external electrical load resistor measured in ohm. The current experiences a sharp decrease as the external load is increased and the optimal operating window is approximately at 700 M Ω at a peak power of 12.5 μ W/cm².

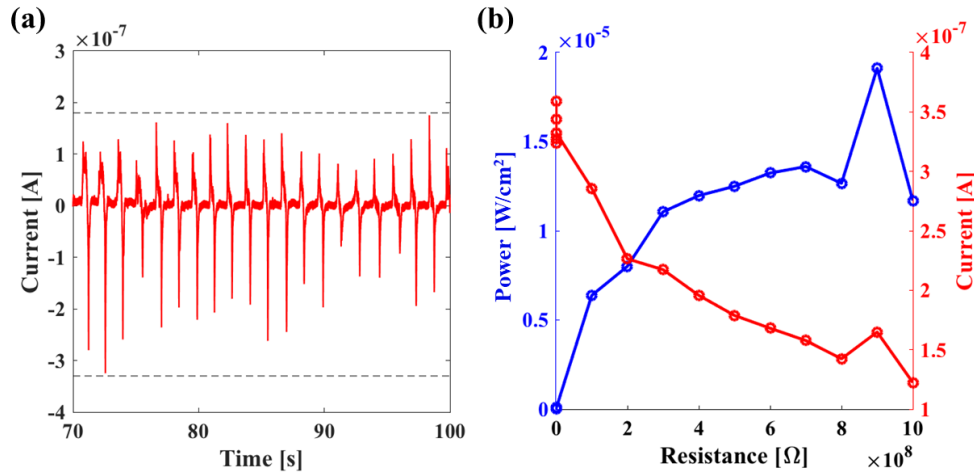


Figure 2.16: Output performance of a triple-layer device under a 3-Newton force at 2 Hz. (a) Short circuit current. (b) Current and power output over varying resistors.

2.2.3. Drawbacks and potential improvements

When compared to state-of-the-art electret devices the power output is considerably low, especially due to the low surface potential achieved when compared to other fluorinated polymer-based electrets (-2500V compared to -12V at steady state) [110]. The main reason for this is the thin electret layer (5-25 μm layers in most conventional electrets compared to 100 nm in this study [142]). As mentioned before the thickness affects the overall surface charge that can be implanted on to the surface and it has been shown that charges can leak underneath the electret and combine with the holes in the underlying material. As such, a thicker electret layer is needed to achieve better performance; however, this study has shown that using 3D printing combined with chemical vapor deposition provides a versatile manufacturing process to potentially increase the overall performance of piezoelectret devices. The next section in this chapter addresses the issues regarding electret thickness and ways to improve performance for such devices.

2.3. 3D Printed Piezoelectret Shoe Sole Energy Harvester via Chemical Vapor Deposition of Parylene C

In the previous section a new method to fabricate electret devices using 3D printing and CVD of Parylene AF4 is described. This approach offers the freedom for designers to create fully tailored devices for specific applications, such as wearable devices as illustrate in Figure 2.17a, which is defined as any device that has a form factor to be worn on the body without impeding regular motion [143] while providing valuable inputs to the user. One very famous wearable device is the Apple watch [144], which can measure biological signals while interfacing with users' other devices to provide a seamlessly integrated virtual network. It is estimated that the wearables market will grow considerably in recent years with an immense market size growth from \$35B in 2016 to \$80B in 2025 (Figure 2.17b) [145].

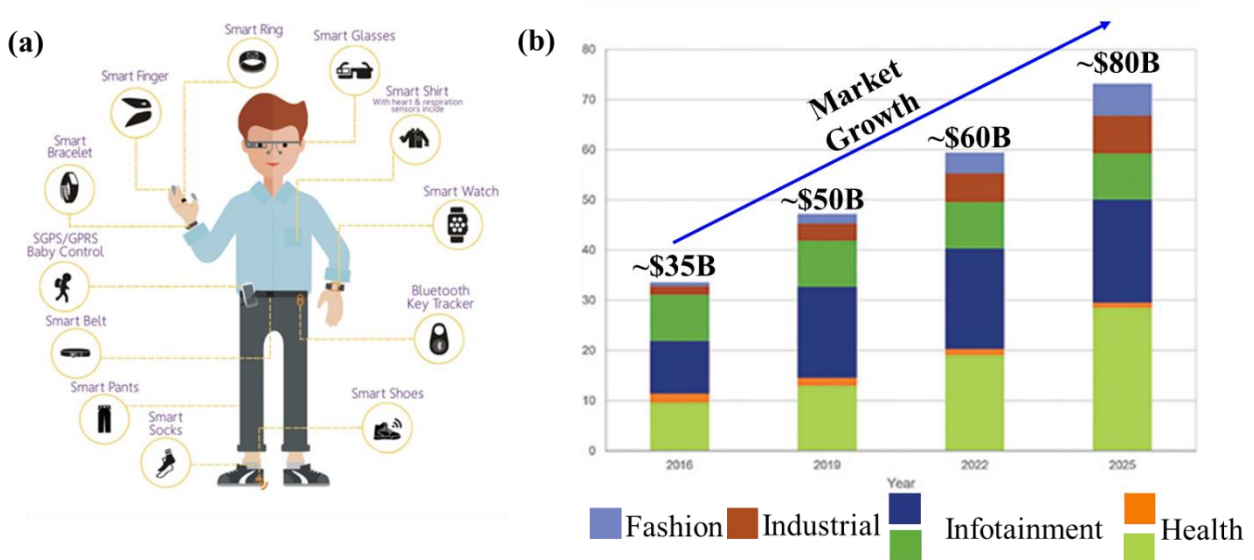


Figure 2.17: (a) Wearable devices; (b) IDTechEx Wearable Technology market projections for the year 2025 [145]

In this section, wearable energy harvesting shoes that can convert mechanical energy with the weight of the body to electrical energy are presented. The main principle of this work relies on the electret's capability of producing electricity when it is compressed. This idea builds up on the theory covered in the previous section to produce 3D printed wearable items [132], such as adidas's 3D printed shoes which have been in the market for nearly 3 years [146]. Even though the overall concept is to build a shoe energy harvester in order to show the concept, a shoe-sole is built instead of a full-sized shoe. It should also be noted that shoe energy harvesters have been investigated previously using various methods mostly involving the addition of an energy harvester implanted into the sole of the shoe. The core issue with these techniques is that the shoe becomes highly uncomfortable for regular use, diminishing the use [111,147–149]. The main idea of this section is to create a prototype system that can overcome the main challenge in creating a wearable energy harvester with good comfort without focusing extensively on the performance.

2.3.1. Device Design & Working Principle

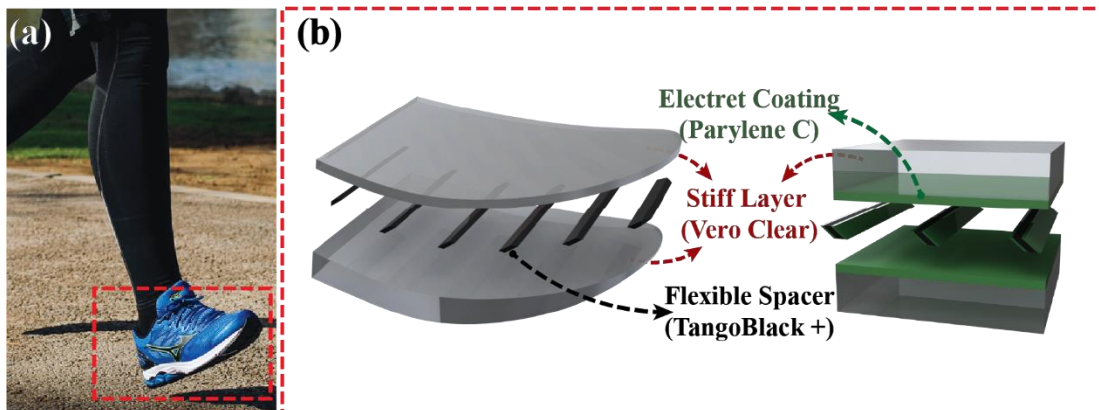


Figure 2.18: Shoe sole concept showing the different materials used for each layer. [150]

The shoe sole concept consists of 2 different materials in a single-layer configuration. Figure 2.18 shows the materials used in this application. A flexible intermediary flexible spacer layer separates the two stiff top and bottom layers. The spacer layer is angled such that it allows for large deformation of the top layer without having it touch the bottom one. Also, the main working principle remains the same as the previous application and relies on the compression of the top layer with respect to the bottom layer to create a change in the quasi-static charge state to cause electron flow from the top to the bottom electrode.

2.3.2. Fabrication and Characterization

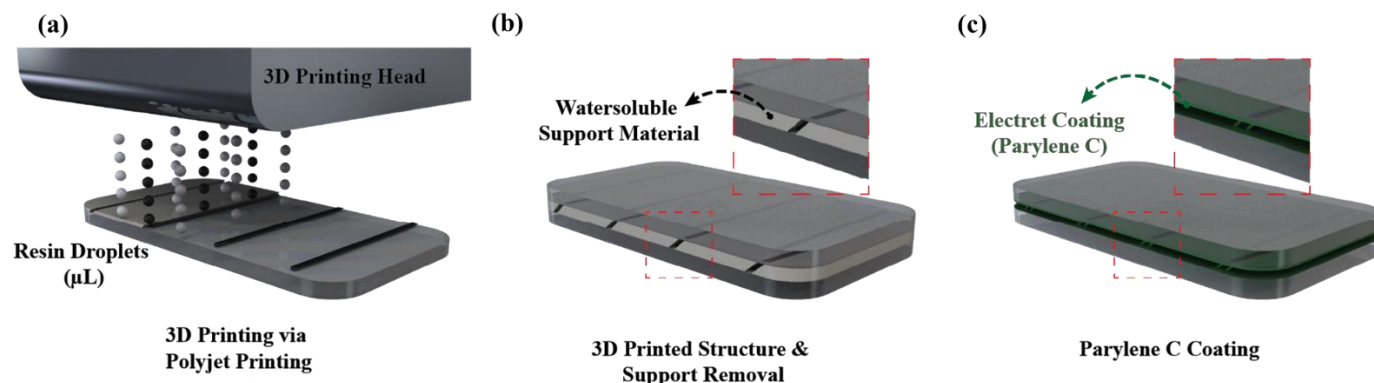


Figure 2.19: (a) PolyJet Multimaterial printing process showing the droplets of different materials being jetted on to the printing surface. (b) Water-soluble support that allows for overhangs to be printed. (c) Parylene C coated surface.

The fabrication method (Figure 2.15) is slightly modified to create structures having different stiffness layers (i.e. different materials) in a single printing step by utilizing PolyJet printing (Figure 2.19). The most important aspects of this method are covered in chapter 1; however, the main differences and advantages of this printing technique compared to the DLP method used in the previous section are the following: (1) multiple materials with varying mechanical properties can be used in a single printing step (Figure 2.19a) and (2) water-soluble support materials can be used to create overhanging structures with ease (Figure 2.19b).

The fabrication method consists of the same steps as the previous method covered in this chapter as seen in Figure 2.19. First, the structures are 3D printed and the support material is removed using 0.5M KOH at 55°C which is stirred continuously during the removal process to increase the removal rate of the support material. Once the structure is released (i.e. support removed), the structure is dried at room temperature under vacuum. Then, the structure is coated with Parylene C using the same chemical vapor deposition system (Specialty Coating Systems' Parylene Deposition System 2010). Using 10 grams of Parylene C dimer material, a total Parylene C thickness of 10 μm is coated on to the polymer structure. Compared to the thickness of Parylene AF4, a 100X increase in thickness is achieved within the same processing time, at a fraction of the material cost [151]. Once the structures are coated, a metal electrode layer is placed on the top and

bottom surface, and copper wiring is used to connect the devices to the experimental setups. The fabricated device can be seen in Figure 2.20 which also shows the shoe sole placed inside a real shoe as the insole.

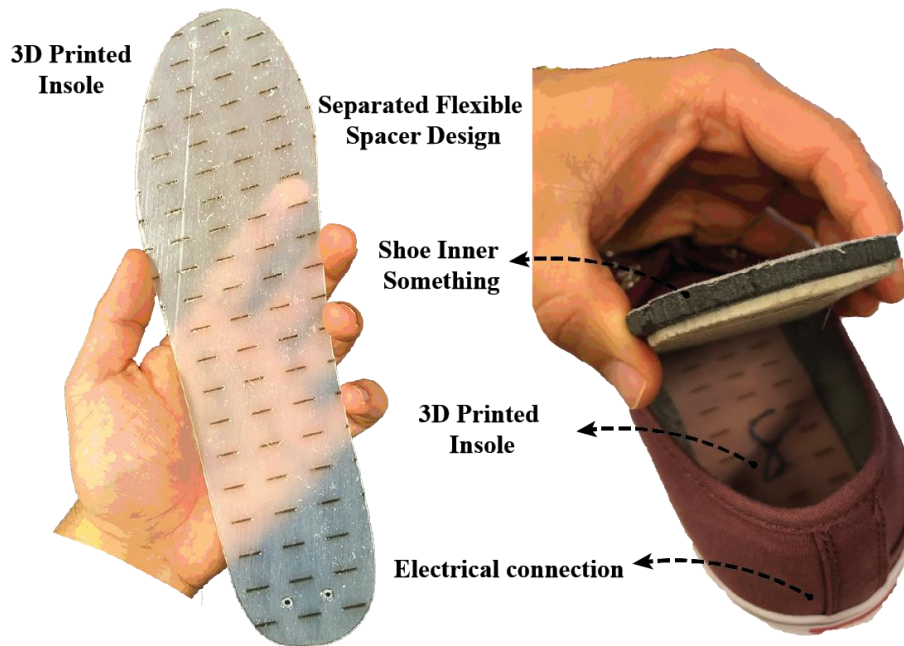


Figure 2.20: Fabricated shoe insole

In order to characterize the fabrication process further, square samples of the same material are coated with Parylene C to test whether a thicker coating of Parylene C could achieve a better surface charge density compared to that of Parylene AF4. The samples are charged via corona charging under the same accelerating voltage of -15 kV. However, to combat the charge leakage issue, longer charging time periods are tested based on the assumption that the underlying substrate could potentially be saturated with charges for more charge retention [152,153]. It is found that longer charging time periods increase the initial surface potential and also decrease the charge decrease rate in Figure 2.21. Furthermore, the initial surface potential is much higher than that of Parylene AF4 coating even for a short charging period (-17 V for AF4 compared to -1000 V for C). It can be concluded that the thickness of the electret layer plays an important role to achieve a high surface potential and the charging time will affect the surface potential degradation rate, in good agreement with previous reports [141,152,154].

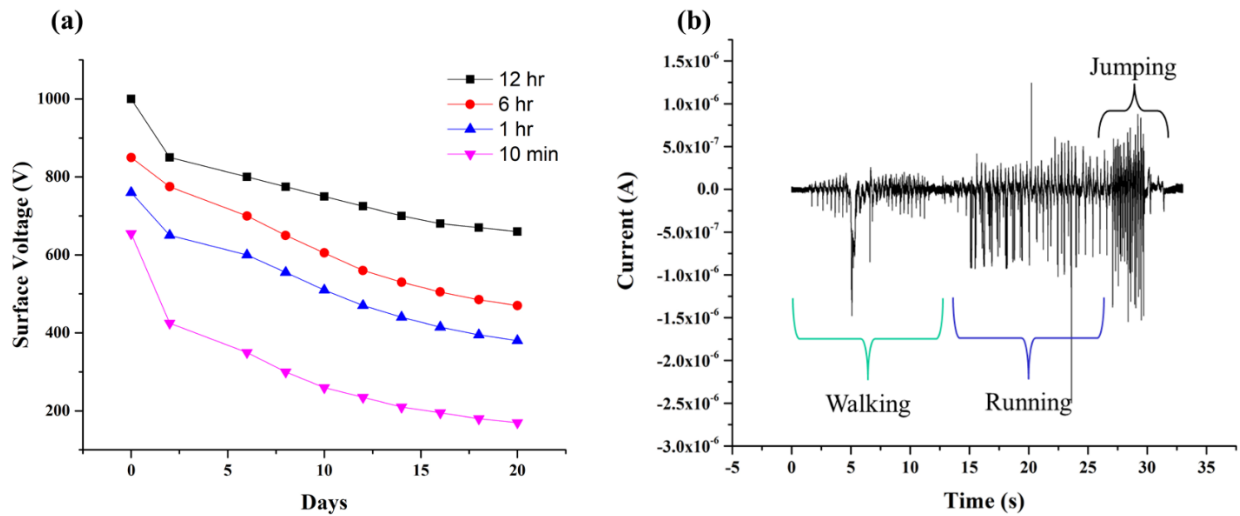


Figure 2.21: (a) Surface charge decay of Parylene C coated on the test sample with different charging time periods. (b) Initial results showing the energy harvesting shoe sole in use. The device can be used to harvest energy while walking, running, and jumping.

2.3.3. Experimental setup, Results, and Discussion

Prototype devices are directly tested under real conditions and the SCC is measured by connecting the electrical wires to a current preamplifier and DAQ. The devices are tested first by walking, running, and then jumping in the same experiment. This is conducted in order to gain insight into the performance of the device for the real-life scenario and to determine whether the device could recover fast enough to harvest energy during the three main types of motion a person can go through with their shoes. Figure 2.21b shows that approximately $1.5 \mu\text{A}$ can be generated while running and jumping with input frequencies up to 4 Hz without structure recovery issues. After completing the first round of testing, the devices are tested under a more controlled environment in which the force and frequency are controlled manually and changed progressively to test real-world performances. A peak power density of $8 \mu\text{W}/\text{cm}^2$ could be harvested through the single-layer insole as seen in Figure 2.22e and f.

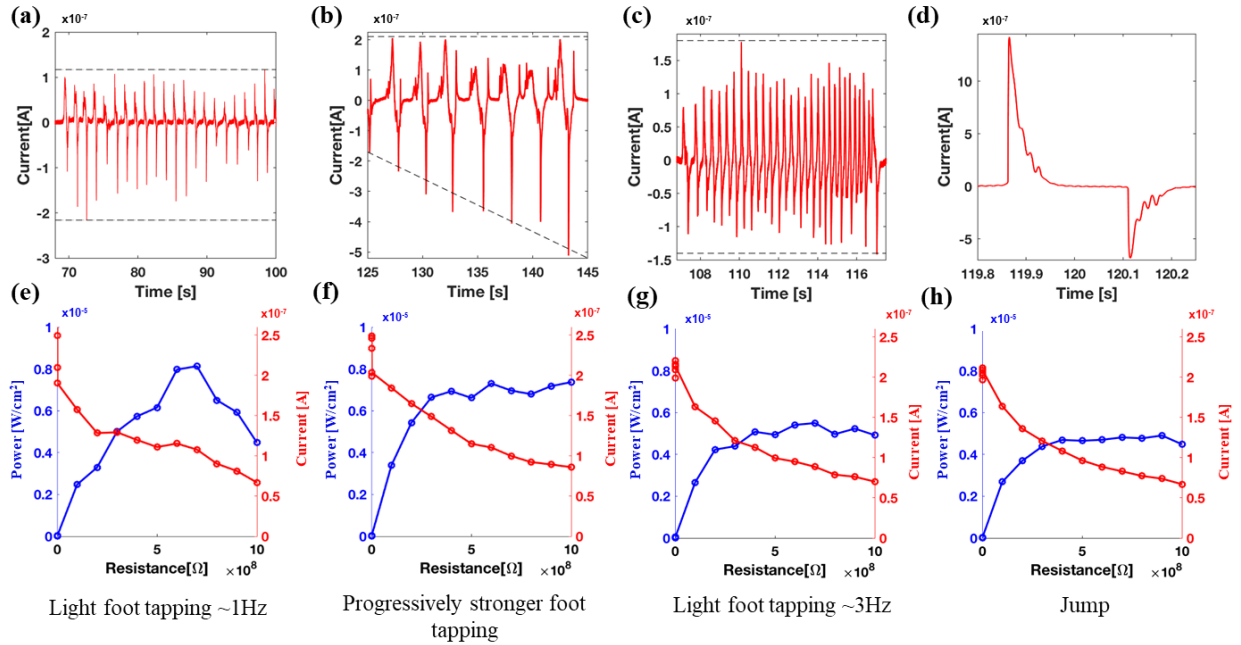


Figure 2.22: Varying force and amplitude testing of shoe insole. (a), (b), (c), (d) are short circuit current outputs and (e), (f), (g), (h) are tested with an external resistive load. (a) & (e) Under light foot tapping condition tested at 1Hz; (b) & (f) Progressively stronger foot tapping; (c) & (g) light foot tapping condition tested at 3Hz; (d) & (h) a single jumping motion.

Figure 2.22 shows that the current output changes as the input force changes progressively to stronger foot tapping cases and the jumping motion. Furthermore, these results show the structure is sturdy enough to carry an average human's weight. The testing results also validate the feasibility to create a fully 3D-printed shoe soles or full shoes to harvest mechanical energy.

In order to fully analyze these devices, further testing needs to be conducted for the long-term usages and the effect of environmental conditions. Furthermore, it should also be investigated whether the output can be further increased by combining the multi-layer device concept as well as different coating materials. Figure 2.23 shows the comparison of the surface potential of different materials used to create eletret energy harvesters in the Lin Lab. Finally, both the comfortability and manufacturability are important for true feasibility for commercialization.

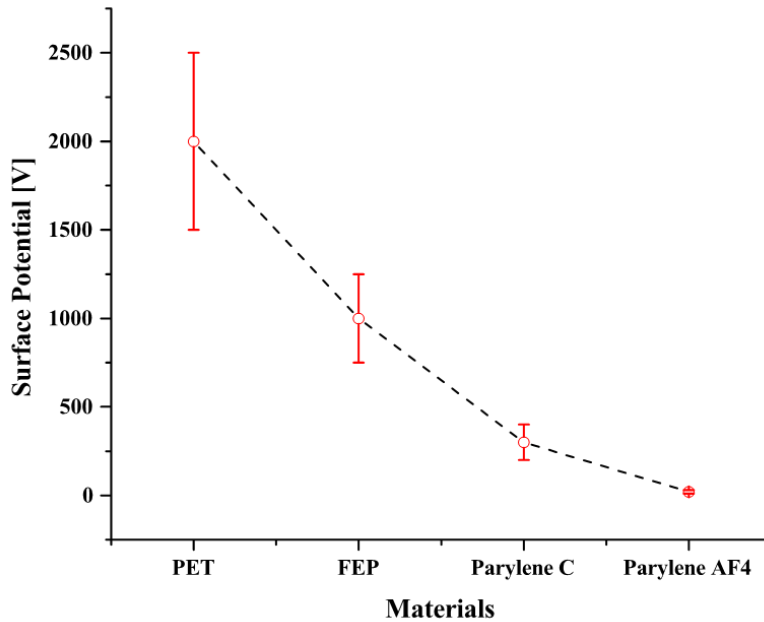


Figure 2.23: Comparison of different materials [56,154–156]

In conclusion, a 3D printed shoe sole as an energy harvester has been constructed using Parylene C coating on surface of 3D printed prototypes by the PolyJet multi-material printing process instead of the DLP printing process described in the first part of this chapter. This results in energy harvesting structure with a flexible supporting layer sandwiched between two stiff layers. Parylene C is used to allow the coating thickness to be 100x thicker than that of the Parylene AF4 coating process at a fraction of the cost with similar processing time. By utilizing a thicker coating layer, much higher surface potential values have been achieved using the corona charging process with a 12-hour long process to reduce the charge leakage issue. The fabricated devices exhibits stable performance for possible different applications. With advances in fabrication and material science for possible better electret materials, further advancements could increase the performance of these devices. In short, the prototype devices have shown that 3D printed structures can be fabricated and functionalized using simple post-fabrication processes for energy harvesters.

2.4. Conclusion

In this chapter, the concepts around piezoelectret devices in energy harvesters are introduced. The drawbacks of current fabrication methods and their limitations in creating complex designs are discussed. These issues are tackled by utilizing 3D printing to create complex structures and chemical vapor deposition of two different kinds of Parylenes to create functional surfaces. Using Parylene as the functional material, electret structures with underlying 3D substrates are constructed. The development of the fabrication method and multi-layer structure designs are introduced to improve the performance of energy harvesters. A triple-layer device has been fabricated via the DLP 3D printing process and functionalized through the CVD of Parylene AF4.

In the subsequent section, a shoe-sole energy harvester has been designed using 3D printing and CVD coating of Parylene to illustrate the simple fabrication for complex designs as energy harvesters.

3. Chapter 3: Magnetically Driven Abrasive Flow Finishing for 3D Printed

Internal Surfaces

The aim of this chapter is to develop a robust post-processing technique that can be used to polish the internal surfaces of 3D printed metal structures. One key application example is 3D-printed copper waveguides fabricated using electron beam melting, since very smooth surfaces are required in these applications. Specific features include: (1) waveguides require a certain surface finish (roughness) to operate efficiently at the required frequency; (2) 3D-printed waveguides can reduce losses that arise due to assembly issues in conventional manufacturing processes; (3) electron beam melting is a powder based process and the surface roughness of 3D-printed structures depends on the size of the metal powder; (4) copper is the material of choice for waveguides due to its high conductivity and good thermal properties. This chapter first introduces the concept of vacuum electronics and current manufacturing methods used. Then electron beam melting is investigated in some detail to understand why surface roughness is a major issue and how it can be reduced. Afterwards state-of-the-art methods for post processing metal 3D printed structures and their properties are presented. In section 3 the first prototype structures are analyzed, and the post processing methods proposed are presented. Finally, the novel polishing method, named magnetically driven abrasive flow finishing, is developed, optimized, and used to polish a 3D printed copper surface reducing the initial surface roughness of 40 μm down to 1.5 μm .

3.1. Literature Review

3.1.1. Vacuum Electronic Devices and Manufacturing Methods

Vacuum electronic devices (VED) are structures used to interact with electromagnetic waves to either modify the signal that is being transmitted or to simply guide it [157]. The earliest VED was a simple vacuum tube which could control electric flow in a high vacuum environment (i.e. diode invented by John Ambrose Fleming in 1904) [158]. Since its invention in the early 1900s till the development of integrated circuits (IC) in the 1960s vacuum tubes played an enormous role in many electrical applications, such as condenser microphones, radios, hearing aids, radars, and televisions [159]. However, with ICs' ability to handle high frequency applications with much lower power consumption and the ease of fabrication with developing micromachining techniques, VEDs fell out of grace and were only used for niche applications, such as microwave ovens, radar systems etc. [160]. With increasing demand in recent years to operate at higher frequencies for data transfer and imaging/screening purposes VEDs have started coming back [161,162]. Especially with long distance data transfer which has very high power requirements it is becoming increasingly complicated to use ICs due to thermal management issues [163]. However, technical challenges still remain in the field, especially in terms of manufacturing. Most fabrication is still done by manual assembly of cavity structures which can be made using conventional fabrication techniques or they are fabricated using expensive micromachining techniques (LIGA) [164]. These

techniques are used in order to achieve very high quality surface finish inside the vacuum tube which is a requirement for high frequency applications (i.e. device operating at 90GHz requires sub-0.2 μ m surface roughness to minimize signal loss) [28,165]. However, the manual assembly process is both time consuming and is prone to misalignment issues, and LIGA is expensive [166]. To combat these challenges metal 3D printing in the form of electron beam melting (EBM) has been proposed for the fabrication of VEDs in recent years [29]. Several advances have been made, yet one key challenge still remains: Surface roughness. Even though the cavity structures can now be built in a monolithic fashion, surface roughness that is required for the successful operation of VEDs cannot be achieved [23]. To better understand why this occurs, EBM and its challenges will be covered in detail in the next section.

3.1.2. Electron Beam Melting and Its Challenges

Electron beam melting is a type of metallic additive manufacturing technique that has been commercialized by the Swedish company ARCAM [167]. This technique can be thought of as a subset of powder bed fusion systems where the metallic powder is raked on to the build bed [2]. The operation principle of this method is as follows and is shown in Figure 3.1:

- (1) The powder is loaded into the machine and is then raked on to the build bed.
- (2) The layer of powder is heated and is then selectively sintered via an electron beam.
- (3) New layer of powder is raked on top of the old layer and is selectively sintered.

These steps are repeated until the desired geometry is fabricated.

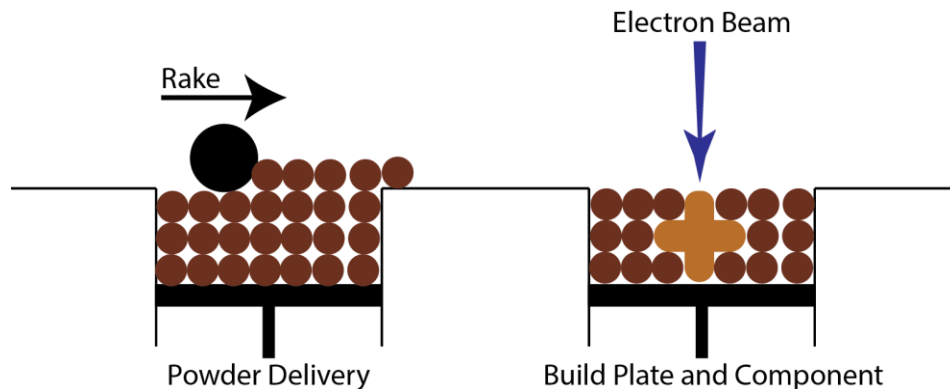


Figure 3.1: Typical setup for Electron Beam Melting (EBM) based system showing the two major compartments and the raking system needed. The part is fabricated on the build plate via electron beam. The unfused particles surrounding the part is removed by post processing. Dark brown particles are unfused copper particles, where as the lighter brown region is fused copper particles.

This process can be considered quite complex when compared to most commercially abundant 3D printers [2]. Vacuum is needed to avoid oxidation of the metal powders and approximately $\sim 8 \times 10^{-6}$ mbar is required for the operation. A 4-5 kW electron beam is generated within the electron beam gun. The tungsten filament is heated to extremely high temperatures to release electrons. These electrons are then accelerated by an electrical field and are focused by electromagnetic coils show

in Figure 3.2. This allows the electron beam to selectively melt each layer according to the final 3D geometry. Depending on the parameter sets and powder sizes, 20-200 μm in layer thicknesses can be achieved with a lateral accuracy of 20 μm [167].

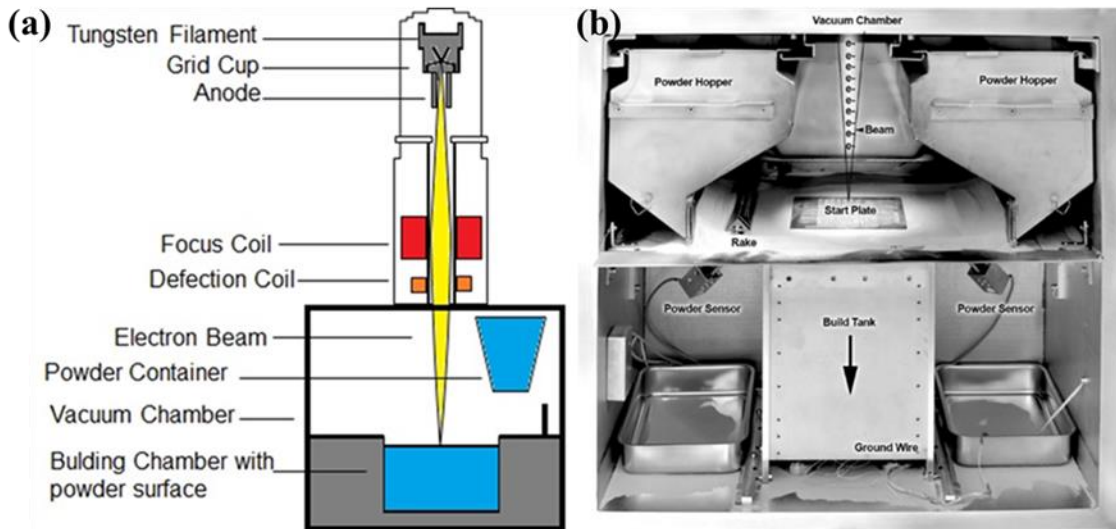


Figure 3.2: Electron Beam Melting (EBM) system used by North Carolina State University. (a) Schematic showing each component, (b) Real device image. Courtesy of North Carolina State University CAMAL

Using this method mechanical properties, such as yield strength and ultimate tensile strength as well as high electrical and thermal conductivity similar to bulk material can be achieved [25]. However, technical challenges still remain in terms of: (1) metallurgy, (2) fatigue, (3) porosity and (4) surface roughness [2].

These challenges arise due to different reasons. First, complex time dependent temperature profiles within the part occur in a layer-by-layer process of 3D printing. Many systems are optimized for very high cooling rates ($\sim 10^4$ K/s) but the combined effects of rapid solidification, and directional cooling can influence the microstructure of the materials deposited, potentially resulting in micro-porosity. Micro-porosity has been one major challenge reported in various studies which can heavily influence the performance of any finished device that requires good surface integrity [2,8].

Second, challenges come from the use of powder itself. For example, this process uses powder (~ 10 -50 μm average diameter) and relies on an energy source to melt and fuse these particles together. In this process some particles do not melt and fuse together entirely and results in high porosity and high surface roughness regions. This is especially evident on the outer surfaces where the temperature is dissipated fast. The outer surfaces, unless post-processed, tend to have partially-fused particles that act as asperities causing the surface to have highly irregular, non-reflective surface profile. This is a major issue in applications that require low porosity (high vacuum applications) and low surface roughness such as waveguides for vacuum electronics.

Finally, the direction of build and the process parameters affect the surface finish as well [8,21]. For example, the surface normal to the build direction has surface roughness approximately half to that of surfaces parallel to the build direction [2].

3.1.3. Surface Polishing Techniques

Many techniques have been developed to decrease the surface roughness of various surfaces either because of aesthetic reasons or because of functionality. For example, the surface of a tool would be given a fine finish such that the tool could be held with ease. For large structures made of wood, carpenters would use sandpaper and apply glossy finishes. For structures made of steel and iron, abrasive techniques such as grinding, blasting (more commonly known as sandblasting), honing, lapping, etc. have been developed. On the other hand, IC fabrication uses a polishing/flatting process known as chemical mechanical polishing (CMP) to flatten the surface. Even though more conventional polishing techniques have been developed for many structures, a post polishing process for enclosed surfaces of 3D printed structures is a challenge.

Techniques for decreasing surface roughness in enclosed structures, widely known as abrasive flow machining, have been developed by several research groups [168–175]. Slurries (high viscosity carrying media and abrasive particles) are flown through, usually with the help of two opposing hydraulic cylinders. The enclosed surface and the asperities on the surfaces are abraded by the help of these particles which are in contact with the surface. Variants of this technique have been developed to increase the performance of abrasion such as; magnetic field assisted abrasive flow machining, magnetorheological abrasive flow finishing, ultrasonic flow finishing, ultrasonic assisted abrasive flow finishing, and rotational abrasive flow finishing [168,170]. However, the application of these techniques have been mainly on steel pipe structures [169,170,176], and very little work has been done on 3D-printed structures [168].

Previously, Lane et al. and Yasa et al. have investigated post processing methods on stainless steel [10,177]; Pyka et al. have investigated post processing methods on Ti6Al4V porous structures [178]. Yasa et al. have focused on post processing via re-melting and using a laser post processing technique to re-fuse un-melted particles on the surfaces. Pyka et al. have used chemical etching in HF and electrochemical polishing in HF to reduce the surface roughness. In all studies the structures investigated were either open surfaces on the top or sides, or they were porous structures where the chemicals could easily penetrate the structure. None of the aforementioned studies focused on enclosed structures. It was noted by Pyka et al. that as the complexity of the parts increased, the post processing methods available and their effectiveness decreased [178]. Liu et al. have also discussed this problem in depth and have noted that when structures required internal finishing the ability to use mechanical (i.e. grinding, sandblasting, etc.), physical or chemical methods decreased [179]. Even though these studies have shown that electrochemical polishing and chemical etching methods can decrease the surface roughness up to 90% [178], none of these methods have focused on internal finishing of enclosed channel-like structures.

3.2. Surface Roughness and Proposed Polishing Methods

To fill the technical void surrounding enclosed surface polishing, two methods have been investigated in this chapter: electrochemical polishing and magnetically driven abrasive flow finishing. First, the surface characterization and preliminary surface roughness measurements of samples fabricated via electron beam melting are presented. Then, electrochemical polishing theory, experiments, optimization and surface roughness results are presented, and the drawbacks of this method are highlighted. Lastly the magnetically driven abrasive flow finishing process is developed. The theory behind abrasive wear and magnetic fields are presented. The analytical and computational modelling of the driving force, a varying/moving magnetic field, is investigated. The process setup and the control mechanism for the experiments are described in great detail and the initial results in terms of the reduction in surface roughness is shown.

3.2.1. Fabrication of Samples and Surface Characterization

3.2.1.1. Sample Fabrication

The samples used throughout this report have been solely fabricated by CAMAL at North Carolina State University. The samples used in this study have been designed by University of California, Berkeley and have been manufactured from OFHC copper powder with a mean size distribution of 50 μm . Some of the parameters used in this fabrication process can be found in table 3.1.

Table 3.1: Fabrication process parameters used by NCSU-CAMAL to fabricate the samples used throughout this chapter

Parameter	Value
Electron Beam Strength	4-5 kW
Vacuum	$\sim 8\text{E}-6$ mBar
Layer Thickness	20-200 μm

Using these parameters, parts with different geometries such as cylinders, cubes and rectangular prisms as well as a chess piece (Figure 3.3a) were fabricated. Even from a qualitative assessment of the surface texture, one can immediately see the un-melted and un-fused copper powder on the surface.

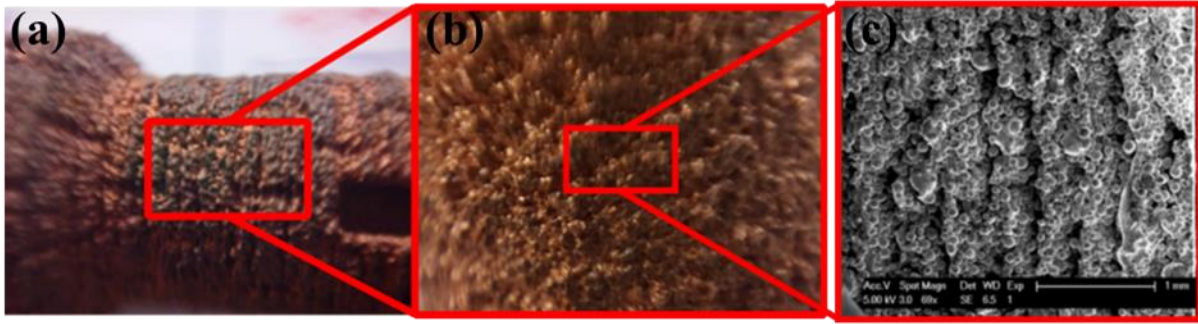


Figure 3.3: A chess-piece manufactured by NCSU, qualitatively showing the unfused particles on the surface of the sample. (a) Chess piece from afar, (b) zoomed in photograph of side surface, (c) SEM image of side surface.

When imaged using a scanning electron microscope (SEM), the fused powder shows a certain orientation following the build-direction (Figure 3.3c). This phenomenon arises due to the fabrication method itself and has been seen in all laser powder bed fusion systems. Due to this phenomenon, different surface textures can be seen on different surfaces. Figure 4 provides a qualitative comparison between two surfaces of the same part.

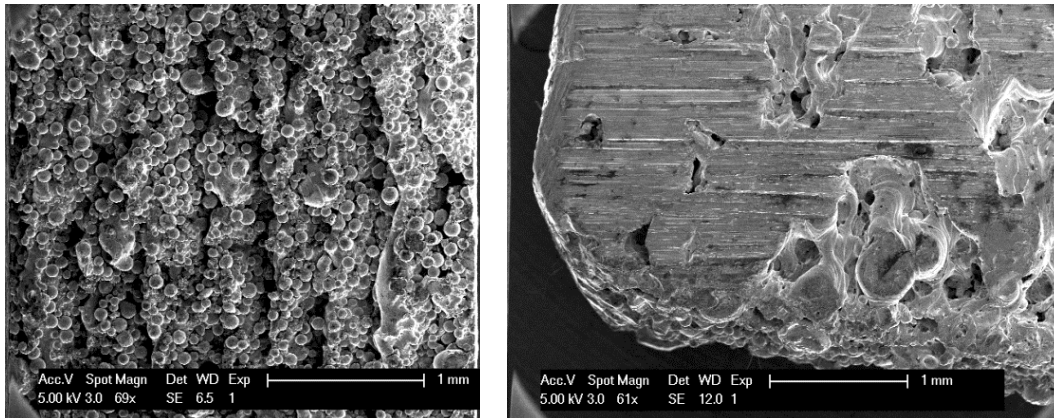


Figure 3.4: Comparison of two different surfaces of the sample to show the differences in surface texture of side (left image) and top (right image) surfaces.

3.2.1.2. Surface Characterization

In this study confocal microscopy (Olympus LEXT OLS3000 3D Laser Confocal Microscope) and surface profilometry (Talysurf, and DEKTAK 2020) were used to determine the surface roughness for the R_a (mean surface roughness) values. Even though R_a is an arithmetic average and can be thought of not being suitable for surface roughness measurements, it has been widely used to characterize surface roughness in the 3D printing industry [8,10,178,180]. The as-fabricated parts had an initial R_a of $35 \mu\text{m}$ on planes parallel to the build direction and

approximately 10 μm on planes perpendicular to the build plane. Figure 3.5 shows the surface roughness values for 29 samples fabricated in the same batch and Figure 3.6 shows the distribution of these values.

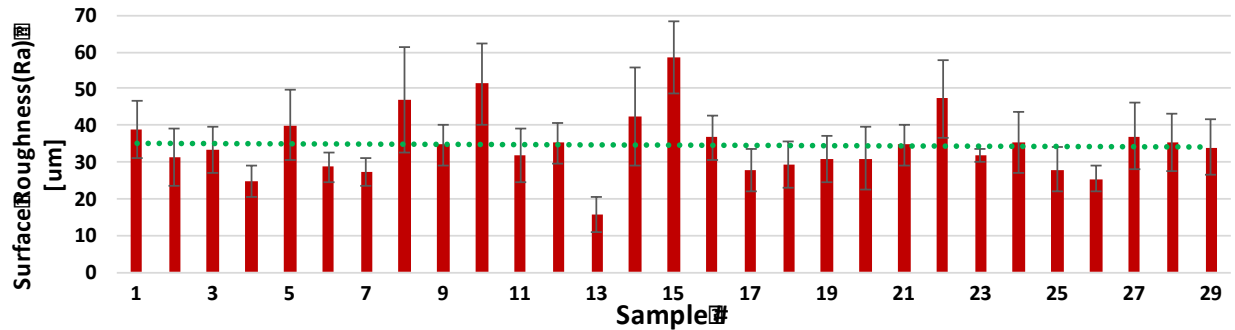


Figure 3.5: Surface roughness of as fabricated samples. These measurements were done both for the top and side surfaces. The surface roughness values approximately 1 standard deviation away from the mean are those of the side surface. The samples with low surface roughness correspond to the top surface measurements

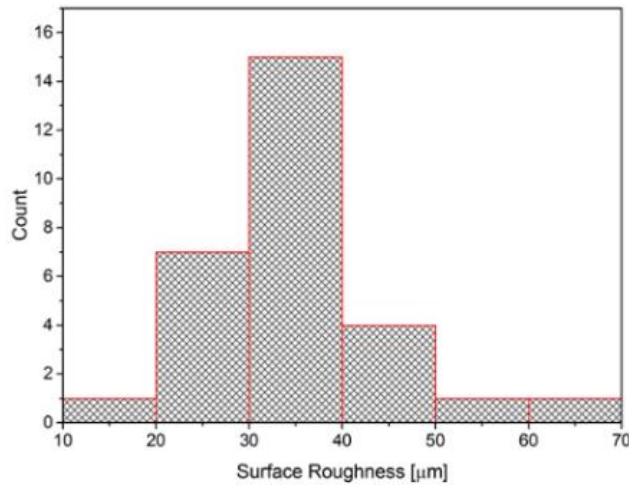


Figure 3.6: Surface roughness distribution of samples

3.2.2. Electrochemical polishing

The use of electrochemical polishing is first seen in literature by Jacquet in 1935 [181]. Studies have been conducted to determine the mechanisms that are responsible for this phenomenon. Mechanistic studies have shown that this process is a diffusion-controlled reaction which occurs at the limiting current [182]. Further studies have also been conducted to determine how additional factors such as electrolyte flow [182] and temperature [183] affect the process. Different metals such as copper, aluminum, stainless steel can be electrochemically polished, and these processes are still widely used today due to their simplicity. For example, semiconductor, biomedical, ultra-

high vacuum devices industries have been using this process as a means to smoothen the surface of fabricated parts [184].

Electrochemical polishing has also received interest in the 3D printing industry. Brent et al. have recently investigated electrochemical polishing for 3D printed steel structures and have optimized their process [185]. However, further process optimization and different strategies are needed for polishing 3D printed internal surfaces.

To develop a process to polish 3D printed copper internal surfaces, first electrochemical polishing of bulk copper was investigated. Many studies have been conducted in this area due to the copper's use in many industries [182,184,186–188]. The use of different electrolytes, additives, polarization characteristics have been studied. Amongst the electrolytes studied, ortho-phosphoric acid (H_3PO_4) was determined to be the electrolyte of choice for copper [186]. The limiting current for copper polishing was determined when the diffusion layer becomes saturated with Cu^{2+} [182]. Studies have been conducted on the concentration of phosphoric acid and its effects on the limiting current. It was seen that the limiting current decreased when the concentration increases to be above 6M [182].

A standard electrochemical polishing setup is shown in Figure 3.7a, consisting of a copper work piece (anode), stainless steel counter electrode (cathode), electrolyte and DC power supply.

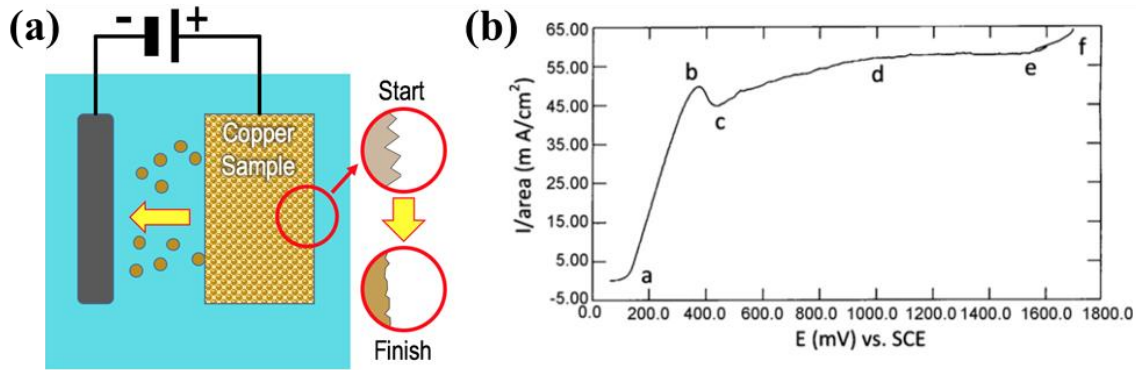
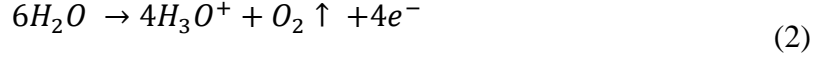


Figure 3.7: Electrochemical polishing. (a) Electrochemical polishing cell showing the smoothening mechanism qualitatively. (b) Polarization curve adopted from [182]

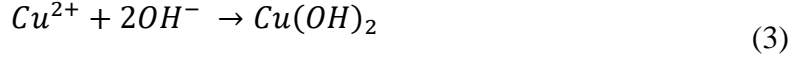
The mechanism of electrochemical polishing can be divided into 5 regions by examining the polarization curves obtained during polishing [184]. These steps also explain how the polishing phenomenon occurs.

- 1) Activation Step: The current sharply increases due to both anodic oxidation of outer surface and ionization of water molecules.





2) Neutralization step: The current and oxide/hydroxide film covering the surface decreases.



3) Stripping step: The current slightly increase and the film formed in step (2) is electrochemically decomposed leaving a bright copper surface.



4) Polishing step: The current stabilizes, and a plateau can be seen due to the presence of two equal and opposite reactions: (1) the surface cavities and depressions are filled up (Eqn. 3), and (2) the decomposition of the surface humps and peaks accompanied by gas evolution (eqn. 4).

5) High Dissolution region: The current density increases, and aggressive oxidation takes place resulting in high loss of copper.

i. Experiments and Results

The electrochemical polishing process used in this chapter uses phosphoric acid as the electrolyte, which has been previously shown to be effective when used to polish copper due to its excellent polarization behavior, promotion of passivity and film-controlled dissolution, and promotion of solution diffusion-control due to its viscosity [184,186,188]. The process depends on various properties such as temperature, process time, concentration of electrolyte, etc. These properties are examined and experimented with, to determine the optimum process parameters that can be used to polish fully enclosed 3D printed copper surfaces. Table 3.2 summarizes the process parameters and the values investigated for optimization purposes.

Table 3.2: Optimization Parameters for Electrochemical Polishing using H₃PO₄

Process Parameter [unit]	Values
Electrolyte concentration [M]	2, 4, 10
Temperature [C]	35, 45, 55, 65, 75
Time [min]	5,10,15, 20
Current Density [A in ⁻²]	0.05, 0.1, 0.2, 0.4

The 3D printed copper samples shown in Figure 3.8 (fabricated by NCSU CAMAL) were used as the work pieces in the electrochemical polishing experiments. These samples were fabricated using copper particles of 50 μm in diameter via the EBM process.

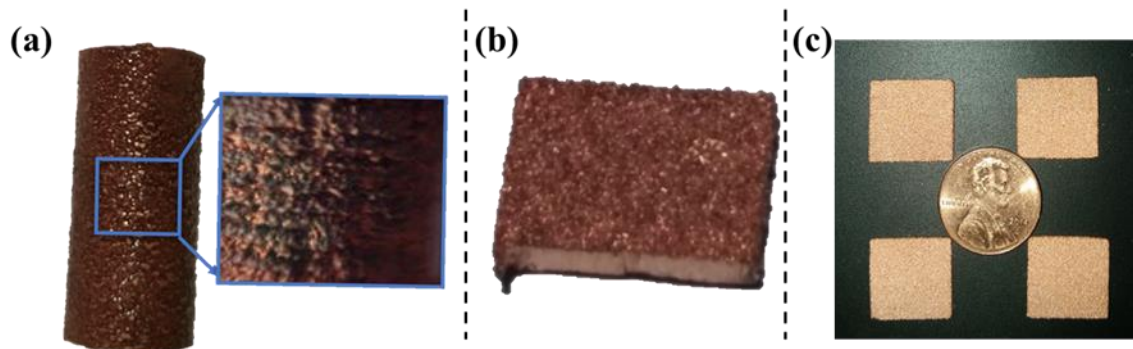


Figure 3.8: Samples used to conduct optimization experiments: (a) a half cylinder-shape sample used to run initial experiments; (b) flat rectangular-shape sample used to easy quantify the surface roughness using contact profilometry; (c) flat $0.5 \times 0.5 \text{ in}^2$ samples with thicknesses ranging from 1 to 4 mm.

The original mean surface roughness value across 30 samples after the metal 3D-printing process was approximately $35 \mu\text{m}$. The electrochemical polishing setup used to conduct the experiments for the optimization processes is shown in Figure 3.9, consisting of a power supply to control the current, a hot-plate heater to control process temperature, a stainless-steel counter electrode, and the copper work piece.

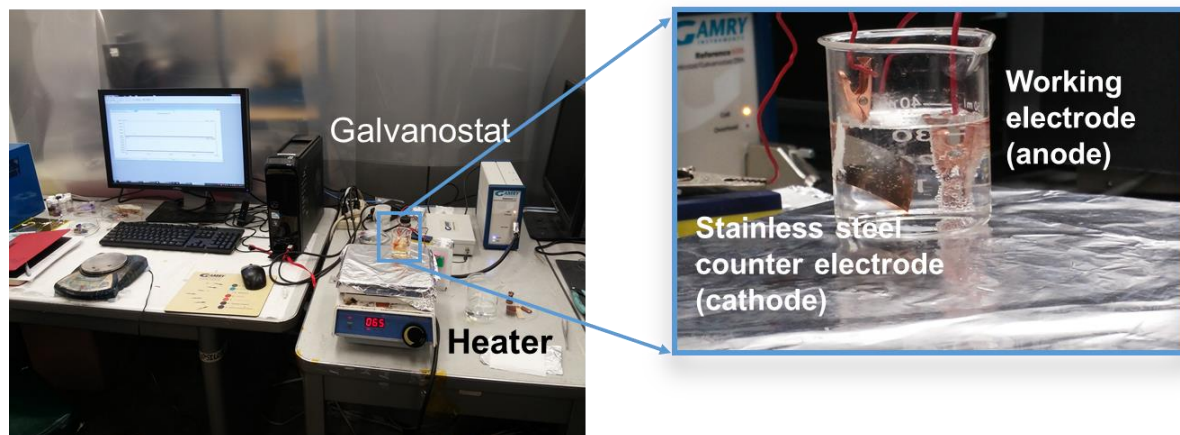


Figure 3.9: Electrochemical polishing setup consisting of Gamry electrochemical unit, hot-plate heater, stainless steel electrode and stainless-steel counter electrode.

The top surfaces of samples were used for evaluation since it provided a flat surface that could be easily analyzed using contact profilometry and confocal microscopy. The top surfaces of these samples are also of importance due to the directional behavior of the fabrication process which results in the top surfaces having the same texture as inner wall surfaces of the waveguides. As such it is beneficial for us to understand the effects of electrochemical polishing on these surfaces and optimize our process appropriately. An example of the samples with various thicknesses used can be seen in Figure 3.8c

By using the parameters shown in Table 3.2, the electrochemical polishing process was conducted, and the process was optimized in terms of electrolyte concentration, processing temperature, and time. It was seen that minimum R_a values for this sample were achieved using a 10M solution at 55°C for 20 minutes resulting in a R_a value of approximately 14 μm . The resulting plots in Figure 10 show the results of the optimization processes with respect to concentration, temperature, current density and time, respectively.

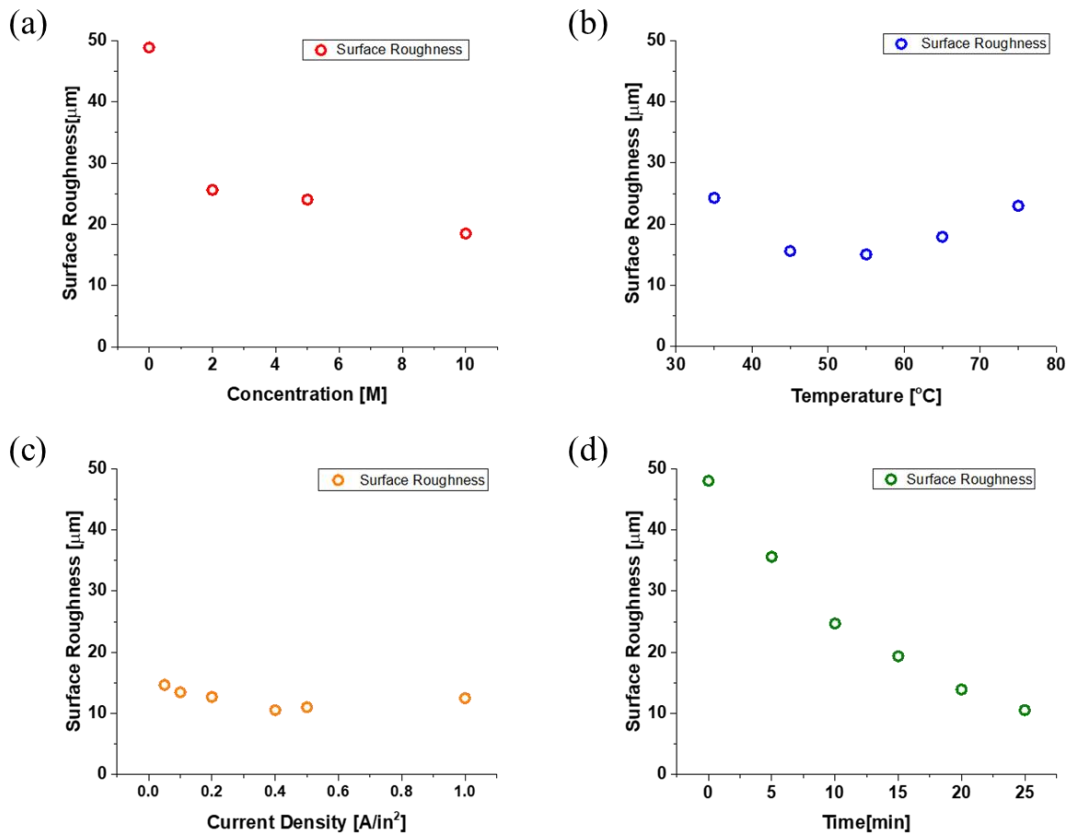


Figure 3.10: Electropolishing optimization results for the surface roughness with respect to: (a) electrolyte molarity; (b) processing temperature; (c) current density; and (d) processing time. The optimized process is for 10M of electrolyte, 55°C of processing temperature, 1 A/in^2 of current density and 25 min of processing time.

After the process optimization step the directionality of the electrochemical polishing process was investigated. Cube-shape samples of 1 cm side length were designed by UC Berkeley and

fabricated by NCU-CAMAL (Figure 11). Different build directions were also used to determine the optimized electrochemical polishing process.

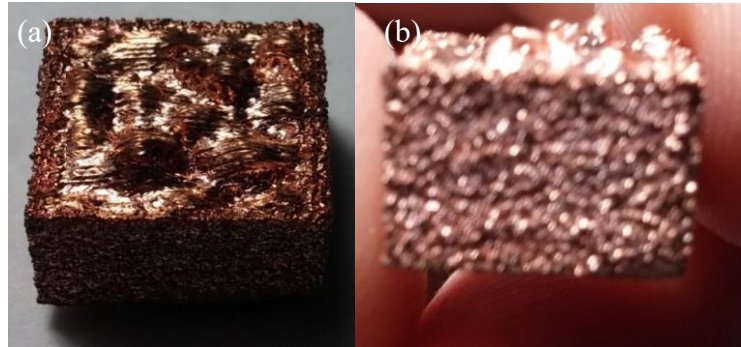


Figure 3.11: Cube-shape samples. (a) Top surface of a cube-shape sample with build direction normal to the top surface. Accumulation of powder due to uneven sintering during operation can be seen. (b) Side wall of the same sample showing rugged surface and layered structure.

As it can be seen from Figure 3.11, the top surface and side wall have different surface textures and different surface roughness values. Uneven powder accumulation on the top surface can also be seen, which is caused by uneven sintering during the sintering process. The electrochemical polishing process was optimized to improve the surface roughness of both the top surface and the side surfaces of the cube. As it can be seen from Figure 3.12a and Figure 3.13 the surface roughness of the side wall decreased significantly down to $\sim 20 \mu\text{m}$; however, the top surface exhibited a different behavior compared to the previous samples that were used for process optimization. The initial surface roughness was measured to be $\sim 10 \mu\text{m}$ in regions where powder accumulation was not seen and when the electrochemical polishing process was employed the surface roughness increased to approximately $\sim 13 \mu\text{m}$ seen in Figure 3.12b and Figure 3.14. Indicating that further optimization is needed for the top surface and it is also an indication of process limitations which gives rise to a search for new methods.

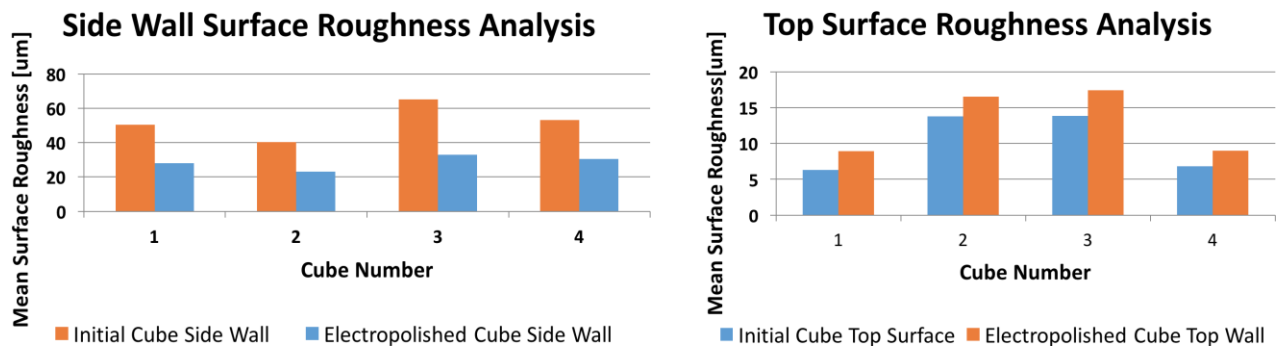


Figure 3.12: Directionality analysis. (left) Side wall surface roughness before and after the electrochemical polishing process to show significant reductions in the surface roughness. (right) Top face surface roughness before and after the electrochemical polishing process to show increases in the surface roughness.

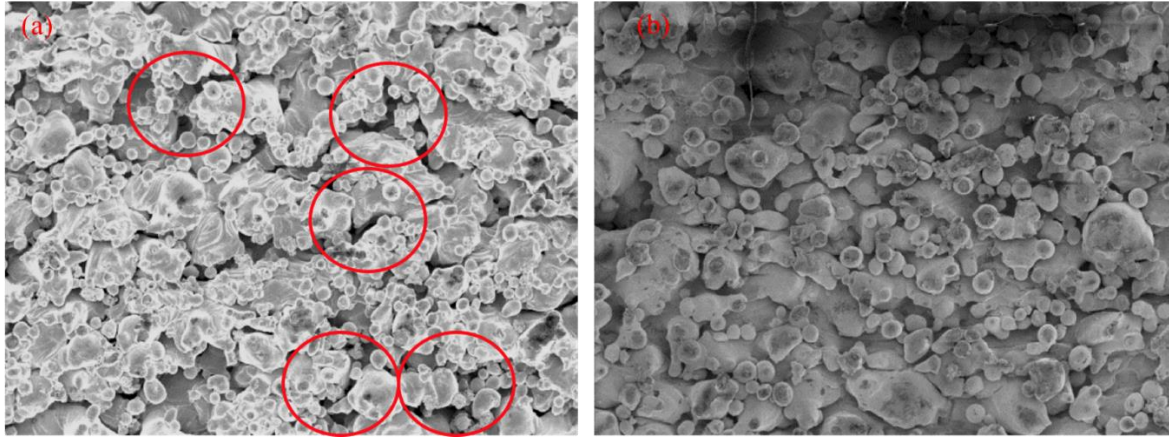


Figure 3.13: SEM images of side wall: (a) the pre-polishing SEM image showing regions where powder has not fully fused to form voids; (b) the post-polishing image showing a smoother texture and less voids.

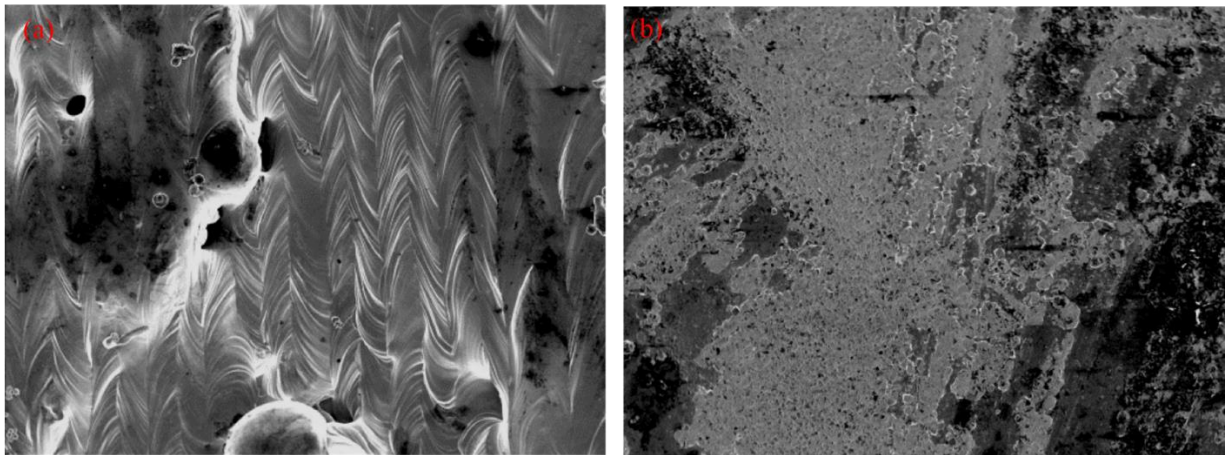


Figure 3.14: SEM images of top surface: (left) the pre-polishing SEM image showing a wavy surface, and (right) post-polishing SEM showing a less reflective and rougher surface.

Considering the different build orientations, the current density and electrode distance used in the electrochemical polishing process need to be optimized to achieve uniform polishing. To investigate this, new samples were produced by NCSU-CAMAL. The optimization samples designed and fabricated were 0.5 in x 0.5 in rectangular prisms with varying thicknesses. Using the process parameters in Figure 10 the optimum electrode area was determined to be 0.25 in², which is the area of the samples used (Figure 3.15a) and the optimum distance was determined to be 0.5 mm between the electrode and the work piece (Figure 3.15b). This distance was limited by our experimental setup hence we could not investigate shorter distances. The minimum surface roughness seen was 9.87 μ m using the optimized process parameters resulting in an overall 71.8% surface roughness reduction.

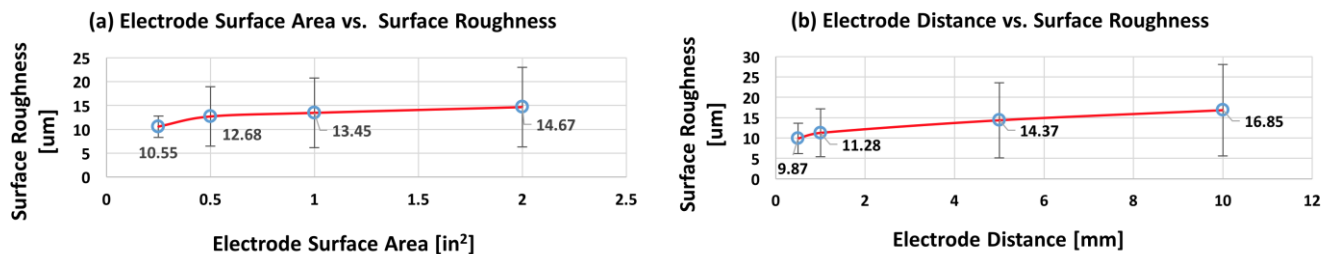


Figure 3.15: Electrochemical polishing results for surface roughness with respect to: (a) electrode surface area; and (b) electrode distance to the sample.

Figure 3.16 illustrates the surface roughness improvement visually. There is a decrease in texture and a smoother look even by optical inspection.

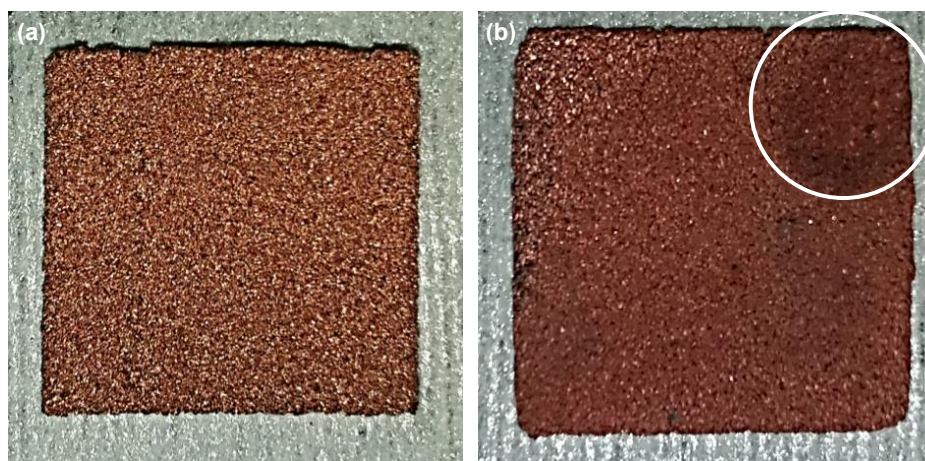


Figure 3.16: Electrochemically polished sample: (a) pre-polishing surface, and (b) post-polishing surface. The mark indicated in (b) is the electrical connection portion. An overall decrease in surface texture and roughness can be seen visually.

However, even with the decrease in surface roughness several drawbacks still exist. Especially, when considering that the application will be for enclosed surfaces, agitation of the electrolyte as well as the positioning of the electrode will be two major issues. Without proper electrode positioning uniform polishing cannot be achieved. Also, fresh electrolyte is always needed to continue the polishing process.

Another issue is that the initial surface roughness and morphology of the fabricated structures may not be suited for electrochemical polishing. As seen in Figure 3.17, a rough top layer exists with a highly random morphology which makes it near impossible to achieve uniform polishing since the electrochemical polishing process depends on the current density at a given location. With the differences in asperity size, the polishing occurs differently at different areas. To combat this issue, an abrasive method that can plow away the large asperities and reach the smooth inner layer is needed.

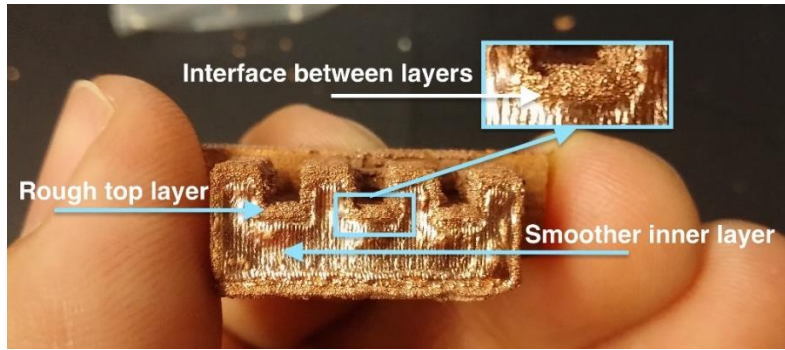


Figure 3.17: Surface morphology of a three-walled channel structure.

3.2.3. Magnetically Driven Abrasive Flow Polishing Process

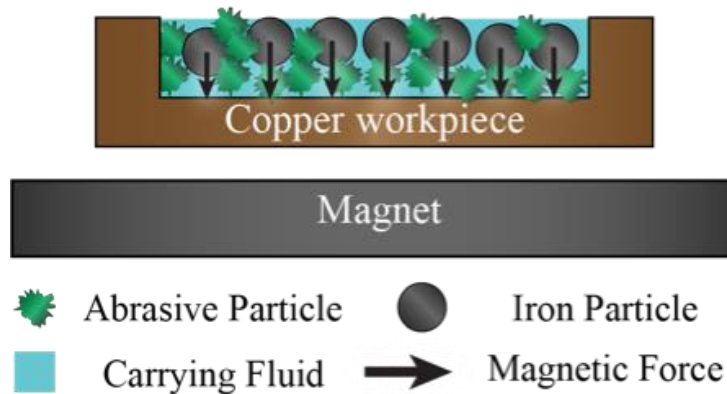


Figure 3.18: Conceptual image of the magnetically driven abrasive flow polishing system

Magnetically driven abrasive flow polishing relies on a moving magnetic field to move the Iron particles in the slurry in a reciprocating motion to induce the motion of the abrasive particles. The main concept is to generate a magnetic downward force to attract both particles towards the surface of the work piece and use this force and the relative motion between the particles and the work piece to plough the asperities on the surface (Figure 3.18). This concept can chip away at the asperities and flatten the surface effectively. By adjusting the magnetic field and the velocity of the magnet the magnetic force on the particles and the movement of the particles can be controlled to produce effective surface finishing.

3.2.3.1. Abrasive Wear Model and Magnetic Field Interaction

The magnetic and abrasive particles are used in the loosely mixed formation. Figure 3.19 illustrates how the particles are distributed in the generated magnetic field. By focusing on one magnetic particle alone one can draw the free body diagram presented in the same figure.

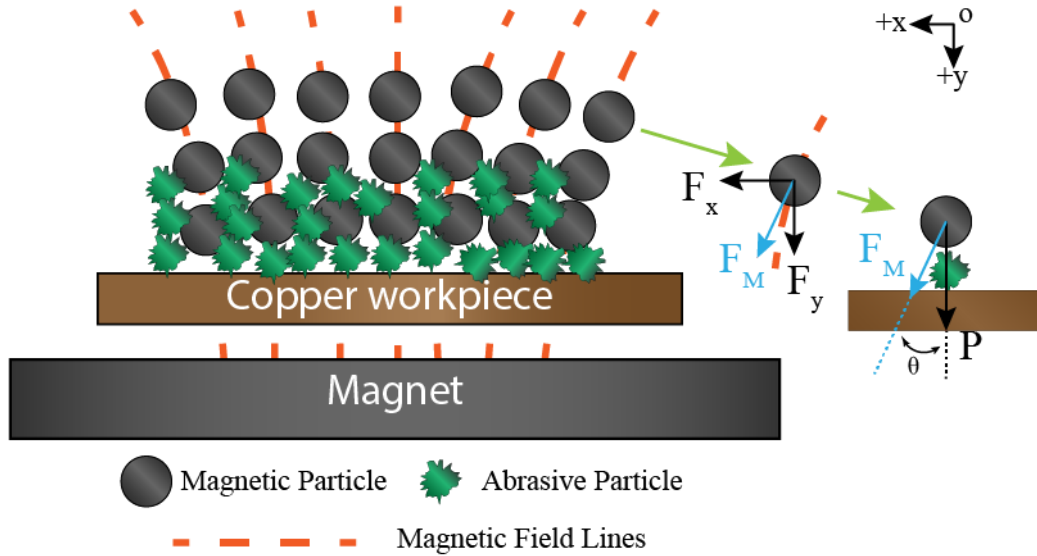


Figure 3.19: Detailed image showing the abrasive slurry containing the magnetic and abrasive particles over a copper work. The permanent magnet and the generated magnetic force lines show how the magnet can guide this slurry. The free-body diagram of a single magnetic particle is also shown. The forces acting on this particle can then be translated to “P”, the force acting on the surface by the abrasive particle.

Using this free-body diagram the forces acting on the magnetic particle can be analyzed. The magnetic force, F_M , can be derived as [189]:

$$F_x = V_o \chi H_x \frac{\partial H}{\partial x} \quad (5)$$

$$F_y = V_o \chi H_y \frac{\partial H}{\partial y} \quad (6)$$

$$F_M = \sqrt{F_{M,x}^2 + F_{M,y}^2} \quad (7)$$

where V_o is the volume and χ is the susceptibility of the magnetic particle, respectively, and \mathbf{H} is the intensity of the magnetic field.

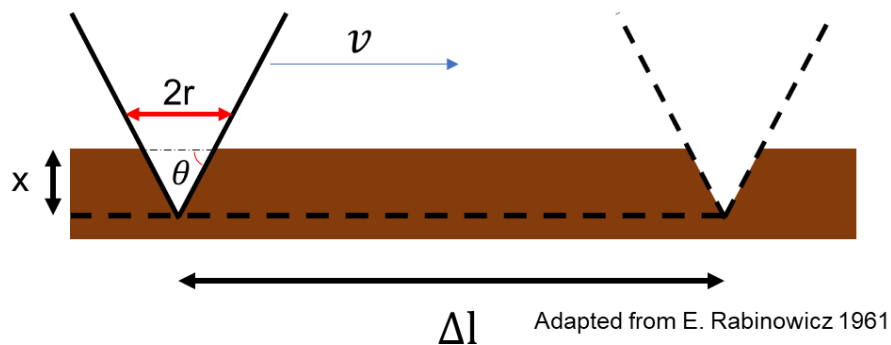


Figure 3.20: Abrasive wear model for material removal [190]

It should be noted that in order to understand the overall material removal and the surface smoothing, the whole slurry must be analyzed. To have a first order estimate, the slurry can be thought of as one body, including the abrasive and magnetic particles together. The force acting on the slurry, which is normal to the surface, is derived as:

$$P = F_M \cos(\theta) = \frac{B^2}{2\mu_o} \left(1 - \frac{1}{\mu_m} \right) \quad (8)$$

where P is the component of the magnetic force normal to the surface seen in Figure 3.19; B is the magnetic flux density of the magnet which can be related to the intensity of the magnetic field (**H**) through Maxwell's equations, θ is the angle between P and F_m , μ_o is the magnetic permeability of air, and μ_m is the magnetic permeability of the slurry. μ_m can be derived as:

$$\mu_m = \frac{\mu_{Fe}\mu_{abrasive}}{\mu_{abrasive}V_{abrasive} + \mu_{Fe}V_{Fe}} \quad (9)$$

Where V_i 's are the volume fractions and μ_i are the magnetic permeability of each particle in the slurry. Developing on these equations we can introduce equation 10 which can be used to determine the material removal rate using the parameters shown in Figure 3.20.

$$S = \frac{V}{t} = \frac{\tan\theta P v}{\pi H_a} \quad (10)$$

where S is the material removal rate, V is the total material being removed, $\tan\theta$ is the wear coefficient, H_a is the hardness of the workpiece, v is the velocity of the slurry and t is the total process time [190]. $\tan\theta$ should not be confused with the angle between P and F_m . $\tan\theta$ is directly related to the sharpness of a given abrasive particle shown in Figure 3.20.

By adjusting the normal magnetic force and the velocity of the slurry, one can easily adjust the material removal rate. The force can be adjusted by changing the magnet being used or the distance of the magnet to the work piece and the velocity can be controlled by controlling the magnet velocity. The wear coefficient can be estimated as 10^{-2} for a 3-body abrasive system [190]. By having the time as a parameter on the right-hand side of the equation, we can directly calculate material that will be removed in a given situation or we can estimate the required process time by first calculating the material that needs to be removed from the surface profiles that were measured previously.

3.2.3.1.1. Mathematical Modeling of the Magnetic field

Analytical Approach

To analyze the system, the magnetic field generated by the permanent magnets needs to be solved. For constant magnetization inside a certain volume that drops to zero immediately beyond the surface, the magnetic flux density is given by [191]:

$$\vec{B} = \nabla \times \vec{A} \quad (11)$$

The potential (\mathbf{A}) at any distance x is given by [192]

$$A(x) = \frac{\mu_0}{4\pi} \oint \frac{\vec{M}(\vec{x}') \times \hat{n}'}{|\vec{x} - \vec{x}'|} da' \quad (12)$$

where \vec{M} , \hat{n}' , and μ_0 are the surface magnetization, normal to the surface at point \vec{x}' , and vacuum susceptibility, respectively [189]. However, a different approach can be used to determine the magnetic flux density of permanent magnets. The whole volume can be treated as having a continuous distribution of magnetic dipoles [189].

$$d\vec{m} = \vec{M}dv \quad (13)$$

$$\vec{M} = M\hat{k} \quad (14)$$

The magnetic scalar potential is given by:

$$\Phi_{dipole}(\vec{x}) = \frac{1}{4\pi} \frac{\vec{m} \cdot \vec{n}}{|\vec{x}|^2} \quad (15)$$

The magnetic flux density is then found to be:

$$\vec{B}_{dipole}(\vec{x}) = \frac{\mu_0}{4\pi} \frac{3\vec{n}(\vec{n} \cdot \vec{m}) - \vec{m}}{|\vec{x}|^3} \quad (16)$$

Using these equations and starting from the magnetic scalar potential for an infinitesimal element in a certain volume with a continuous distribution of magnetic dipoles with the same

magnetization, the magnetic flux density induced by a permanent magnet at a distance z from the surface can be calculated as:

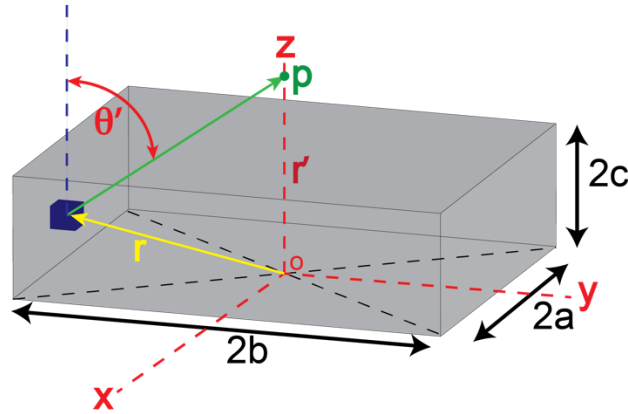


Figure 3.21: Permanent magnet illustration showing the dimensions, infinitesimal element and point of evaluation (p). The center of the selected infinitesimal element has coordinates of x', y', z' .

The distance from the infinitesimal element to the point of evaluation, $|\vec{r} - \vec{r}'|$, can be written as $|\vec{r} - \vec{r}'| = [x'^2 + y'^2 + (z - z')^2]^{1/2}$. This distance will be used to evaluate the magnetic scalar potential caused by the dipoles in the infinitesimal element by using the previously developed equation for the scalar magnetic potential in differential form. The derivation will focus only on the magnetic flux parallel to the z axis, since this value is of importance in calculating the abrasive force acting on the copper sample.

$$\begin{aligned} d\phi_{z \text{ axis}}(z) &= \frac{1}{4\pi} \frac{dm \cos\theta'}{|\vec{r} - \vec{r}'|^2} = \frac{1}{4\pi} M dV \frac{z - z'}{|\vec{r} - \vec{r}'|^3} \\ &= \frac{M}{4\pi} \frac{z - z'}{[x'^2 + y'^2 + (z - z')^2]^{3/2}} dx' dy' dz' \end{aligned} \quad (17)$$

The differential magnetic scalar potential can then be integrated over x, y, z which are $2a, 2b, 2c$, respectively as seen in Figure 3.21.

$$\frac{M}{4\pi} \int_{-c}^c (z - z') dz' \int_{-b}^b dy' \int_{-a}^a \frac{dx'}{[x'^2 + y'^2 + (z - z')^2]^{3/2}} \quad (18)$$

Integrating over x and y gives the following equation for the magnetic scalar potential only as a function of z .

$$\phi_{z \text{ axis}}(z) = \frac{M}{\pi} \int_{-c}^c \arctan \frac{ab}{(z - z')\sqrt{a^2 + b^2 + (z - z')^2}} dz' \quad (19)$$

$$\Phi_{z \text{ axis}}(z) = \frac{M}{\pi} \left[(z+c) \arctan \frac{ab}{(z+c)\sqrt{a^2+b^2+(z+c)^2}} - (z-c) \arctan \frac{ab}{(z-c)\sqrt{a^2+b^2+(z-c)^2}} \right] \quad (20)$$

The following relation can then be obtained by substituting $M = \frac{B_r}{\mu_0}$.

$$B_{z \text{ axis}}(z) = \frac{B_r}{\pi} \left[\arctan \frac{ab}{(z-c)\sqrt{a^2+b^2+(z-c)^2}} - \arctan \frac{ab}{(z+c)\sqrt{a^2+b^2+(z+c)^2}} \right] \quad (21)$$

Even though the z component of the magnetic flux density is of importance, the other components are given below for the completeness of the analysis from the solutions by Yang et al. [193].

$$B_x(x, y, z) = \frac{B_r}{4\pi} \ln \left(\frac{F_2(-x, y, -z)F_2(x, y, z)}{F_2(x, y, -z)F_2(-x, y, z)} \right) \quad (22)$$

$$B_y(x, y, z) = \frac{B_r}{4\pi} \ln \left(\frac{F_2(-y, x, -z)F_2(y, x, z)}{F_2(y, x, -z)F_2(-y, x, z)} \right) \quad (23)$$

$$B_z(x, y, z) = -\frac{B_r}{4\pi} [F_1(-x, y, z) + F_1(-x, y, -z) + F_1(-x, -y, z) + F_1(-x, -y, -z) + F_1(x, y, z) + F_1(x, y, -z) + F_1(x, -y, z) + F_1(x, -y, -z)] \quad (24)$$

where F_1 and F_2 are given by:

$$F_1(x, y, z) = \arctan \left(\frac{(x+a)(y+b)}{(z+c)\sqrt{(x+a)^2 + (y+b)^2 + (z+c)^2}} \right) \quad (25)$$

$$F_2(x, y, z) = \frac{\sqrt{(x+a)^2 + (y-b)^2 + (z+c)^2} + b - y}{\sqrt{(x+a)^2 + (y+b)^2 + (z+c)^2} - b - y} \quad (26)$$

By using equations 24 and 25, the magnetic flux density parallel to the top surface of the magnet at various distances can be calculated as shown in Figure 3.22 which can be used to determine how much the magnetic particles will experience the magnetic force due to the magnet in x and y directions.

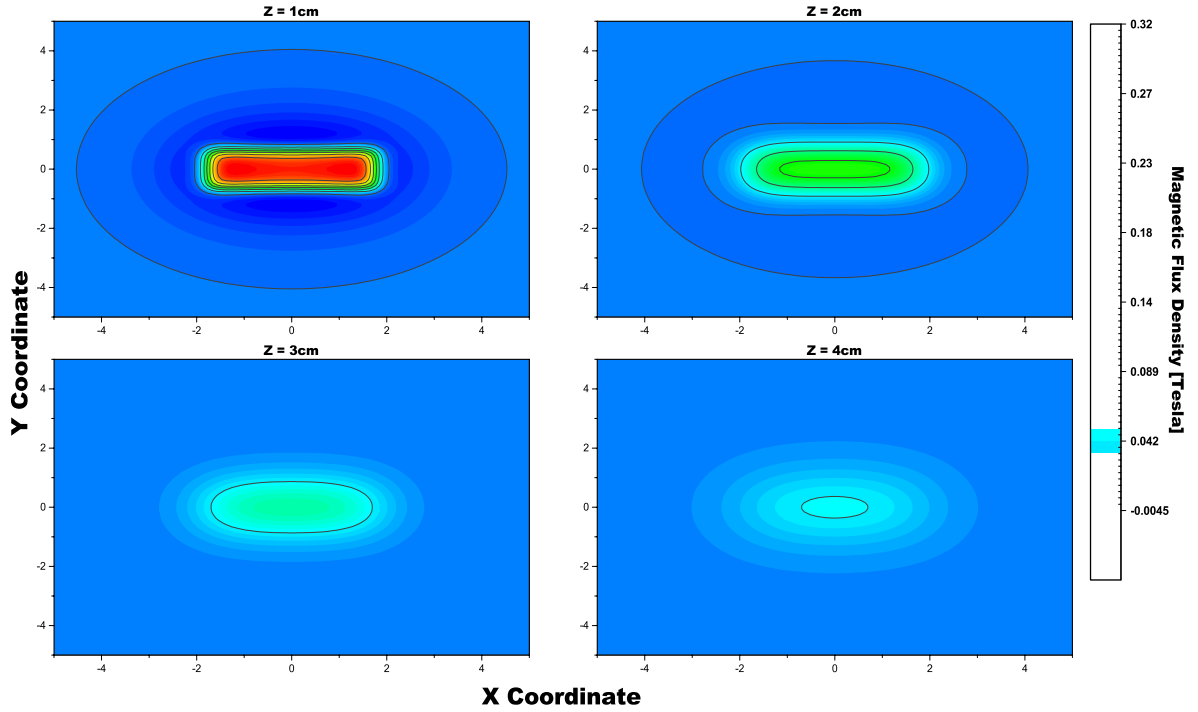


Figure 3.22: Magnetic flux density contour plots showing the magnetic flux density in units of Tesla at various distances from the surface of the permanent magnet. The force generated by the magnetic field on the abrasive particles is directly proportional to the magnetic flux density hence understanding how the flux density decays is an important parameter in designing the experimental setup.

Computational Approach

The magneto-rheological abrasive finishing method relies entirely on the permanent magnet that generates the magnetic field inside the copper waveguide and its movement. To predict the amount of material that will be removed, the magnetic force needs to be determined and optimized. The speed at which the magnet travels is also another parameter that needs to be determined. Since the movement distance is short (~10 cm) the particles have limited time to react to the changing magnetic field and move together with it. To accomplish this optimization process, FEA simulations need to be performed to determine the magnetic flux density and speed of the magnet and the separation between the magnet and the work piece. To perform these simulations, COMSOL Multiphysics is utilized [194]. The changing magnetic field is first modeled in this section and then the output from this section is used to manipulate the particles in the following section. To obtain the magnetic field, Maxwell's equations need to be solved [189]. Gauss's law of magnetism is expressed as:

$$\nabla \cdot B = 0 \quad \nabla \times B = \mu_o(J_f + J_b) = \mu_o J \nabla \times M = J_b \quad (27)$$

Ampere's law in the presence of a current field can be expressed as:

$$\nabla \times H = J_f \quad (28)$$

Where $\mu_o = 4\pi \times 10^{-7}$ is the permeability of free space and J_f and J_b are the free and bound electric current, respectively. J is the current flux, M is the magnetization, H is the magnetic field strength. The magnetic flux density, B , depends on the previous parameters as follows:

$$B = \mu_o(H + M) = \mu_o(1 + \chi)H \quad (29)$$

where χ is the susceptibility of the material, or in this case the magnetic and abrasive particles.

Maxwell's equations can be simplified since no electrical current exists in this structure.

$$\nabla \times B = 0 \quad \nabla \times M = 0 \quad \nabla \times H = 0 \quad (30)$$

In order to simulate the moving magnetic field, the 2D geometry seen in Figure 3.23 is used. Four domains exist, (1) air, (2) magnet, (3) copper work piece, (4) magnetic-abrasive slurry. The use of 2D geometry significantly reduces the computational load and decreases computation time to create an effective optimization tool.

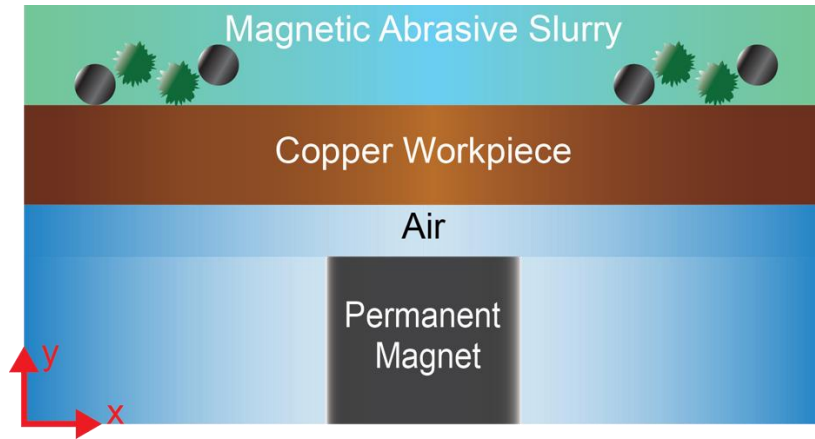
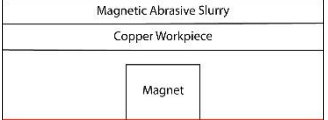
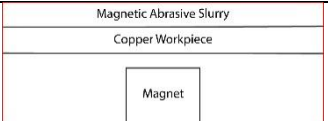
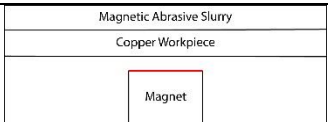
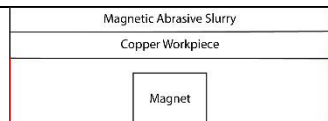
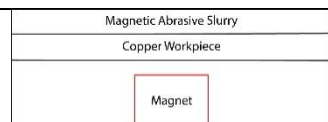
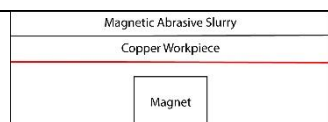
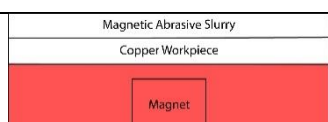


Figure 3.23: The 2D geometry used for computational modeling showing the available domains.

Two sets of boundary conditions are needed to fully define and solve this model: (1) boundary conditions defining the magnetic field, and (2) boundary conditions for deforming the mesh to move magnet.

The first set of four different boundary conditions includes: (1) magnetic insulation, (2) continuity pair, (3) magnetic shielding, (4) magnetic flux density. The second set of boundary conditions include: (1) free deformation and (2) prescribed deformation. Table 3.3 shows the associated equations and the boundaries to which these conditions are applied.

Table 3.3: Boundary conditions used in the computational model [194]

Boundary Condition	Equation	Applied Boundary/Domain
Magnetic Insulation	$\hat{n} \cdot \vec{B} = 0$	
Magnetic Shielding	$\hat{n}(\vec{B}_1 - \vec{B}_2) = -\nabla_t d_s d(\mu_0 \mu_r \nabla_t V_m)$	
Magnetic Flux Density	$\hat{n} \cdot \vec{B} = \hat{n} \cdot \vec{B}_o$	
Prescribed Mesh Displacement 1	$d_x = d_y = 0$	
Prescribed Mesh Displacement 2	$d_x = 10[mm] \sin(wt)$ $d_y = 0$	
Prescribed Mesh Displacement 3	$d_x \neq 0 \quad d_y = 0$	
Free Deformation	$d_x = d_y \neq 0$	

Since the structure is constructed from rectangular domains, a mapped mesh (as can be seen in Figure 3.24) is used in combination with the moving mesh model and associated boundary

conditions to simulate a moving magnet structure. The displaced mesh model accounts for the magnet speed and is only used in the magnet and air domains as seen in Table 3.3 for this study.

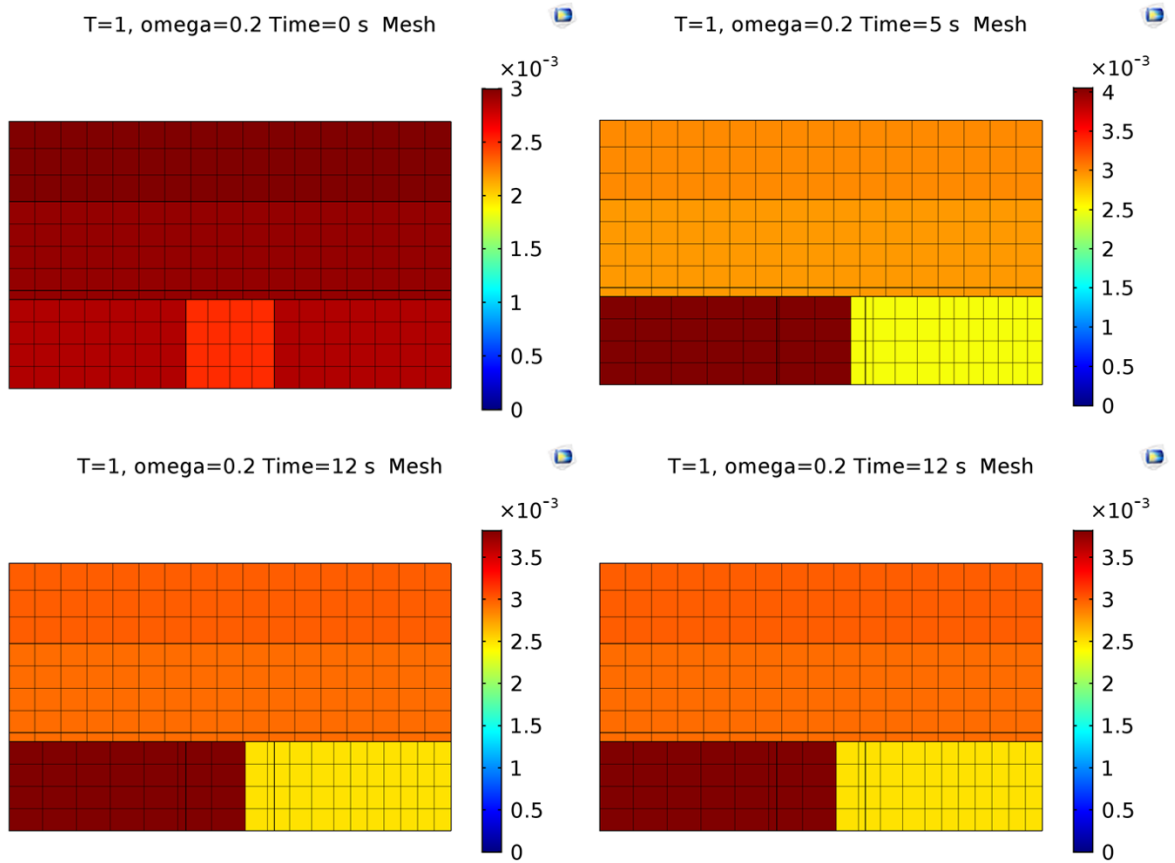


Figure 3.24: Mapped mesh used in the computational model with the color bar representing element size. At time = 0s the mesh is not deformed. The consecutive time steps show how the mapped mesh is deformed.

To achieve a time-dependent solution, the magnetic field is first initialized inside the magnetic-abrasive slurry domain by solving the model as if it were a stationary model. This solution is then used in the transient model as the initial condition for the magnetic field. The solution uses time-steps of 0.1s and simulates up to 20s (Figure 3.25).

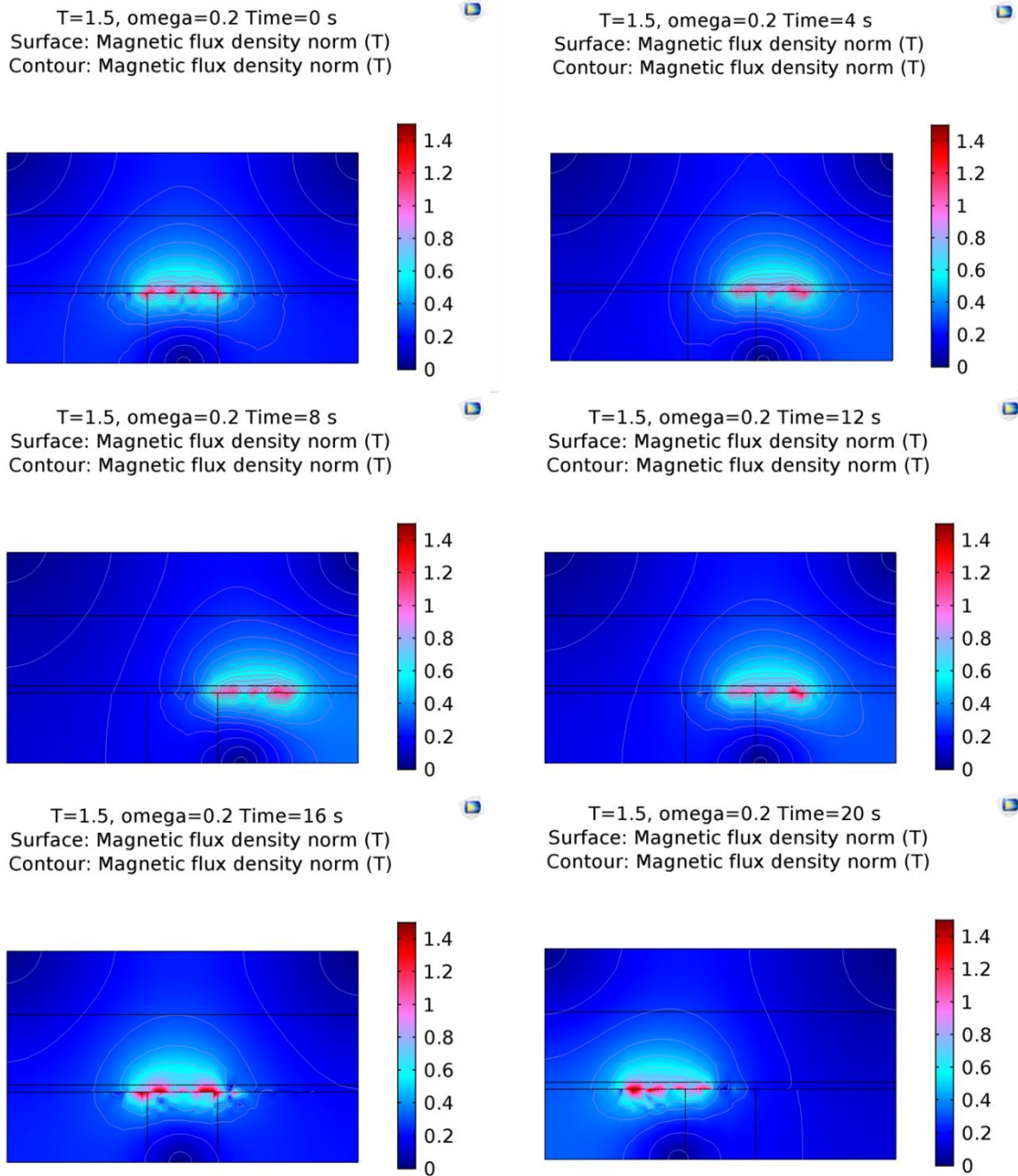


Figure 3.25: Computational results for the magnetic flux density showing both a surface plot and the magnetic flux contour lines. The consecutive images (right to left and then top to bottom) show how the translational magnetic field and hence the magnetic flux density changes over 1 full cycle.

A parameter sweep is also conducted to understand how the magnetic field inside the slurry domain is affected as seen in Figure 3.26. Table 3.4 shows the parameters and the values of this sweep. By using this parameter sweep, the optimal separation distance and magnetic flux density are identified.

Table 3.4: Parameter sets used to conduct the parameter sweep

Parameter	Value
Magnetic Flux Density [Tesla (T)]	0.5, 1, 1.5
Frequency of motion [Hz]	0.1, 0.2, 0.3, 0.4
Separation distance [mm]	10, 20, 30, 40

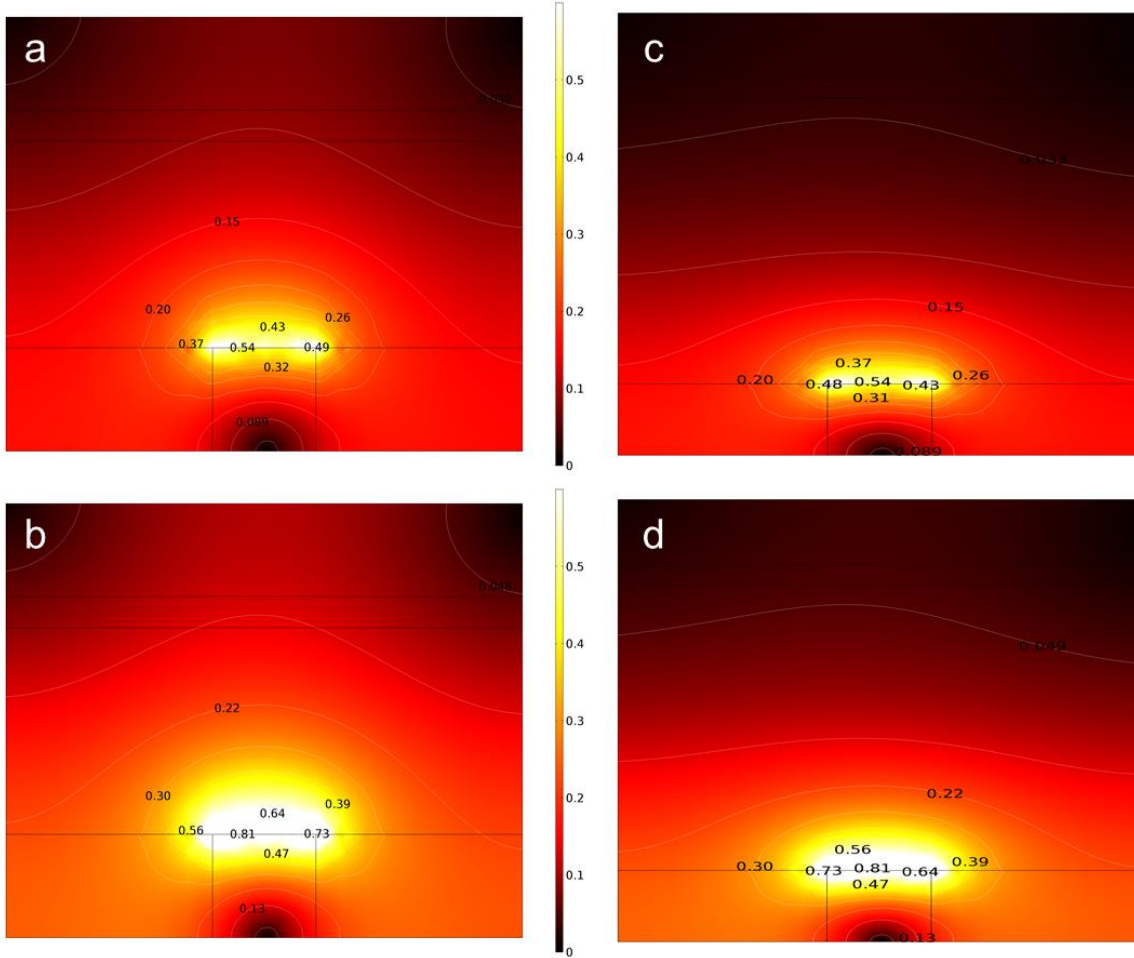


Figure 3.26: Parameter sweep results showing how the magnetic flux density changes with varying air gap distance between the magnet and the copper piece and the magnetic flux density on the magnet's surface. (a) Magnetic flux density 1 Tesla, and 2cm air gap. (b) Magnetic flux density 1 Tesla, and 4cm air gap. (c) Magnetic flux density 1.5 Tesla, and 2cm air gap. (d) Magnetic flux density 1.5 Tesla and 4cm air gap.

3.2.3.2. Factors Affecting Abrasive Wear

By combining the computational and theoretical approach to abrasive material removal and magnetic fields, 3 important factors have been identified to affect the abrasive wear in this system: (1) the force applied normal to the surface (P in Eqn. 8), (2) the velocity of the abrasive particles (V in Eqn. 10), and the wear coefficient of the particles ($\tan\theta$ in Eqn. 10).

3.2.3.2.1. Force

The normal force acting on the abrasive particles, which will be called the abrasive force, is one of the most crucial factors affecting the abrasion process. It is observed in Eqn.10 that the processing time will decrease as the abrasive force increases. Conversely, if the processing time is kept constant, the amount of material removed will increase as the abrasive force increases in the polishing process.

Three factors can influence the abrasive force: (1) magnet strength; (2) size of the magnet; and (3) concentration of iron particles. The first two contributing factors can be combined into one effect, which is the magnetic field. By choosing a magnet with higher magnetization and increasing the size of the magnet, the force acting on the particles can be increased. Currently the strongest commercially available permanent magnets are made from Nd-Fe-B with a magnetic strength of 1.5 T. Simplifying the model derived in the previous sections by assuming that the force generated on the iron particle is directly transferred to abrasive particles, it is calculated that the maximum force achieved is approximately 0.04 N/particle at approximately 2 cm away under the influence of a 1.5 T magnet. However, increasing the force can result in contamination issues due to the particles becoming embedded on the workpiece surface. If the force is too strong, the whole abrasive particle can penetrate the material and can be trapped. To ensure that contamination is minimized, the maximum achievable force of 0.04 N/particle is compared to the force that would be required to trap the particle. This trapping force is calculated as illustrated in Figure 3.27 by assuming that the cross-sectional area of an abrasive particle is circular in shape and multiplying its area with the hardness of the material ($H_a \approx 350\text{MPa}$ for copper, and largest magnetic particle diameter $\approx 200\mu\text{m}$). Through these calculations, it is found that the force required for particle penetration is approximately 11N/particle, which is far greater than the maximum achievable force, indicating that workpiece contamination should not be an issue.

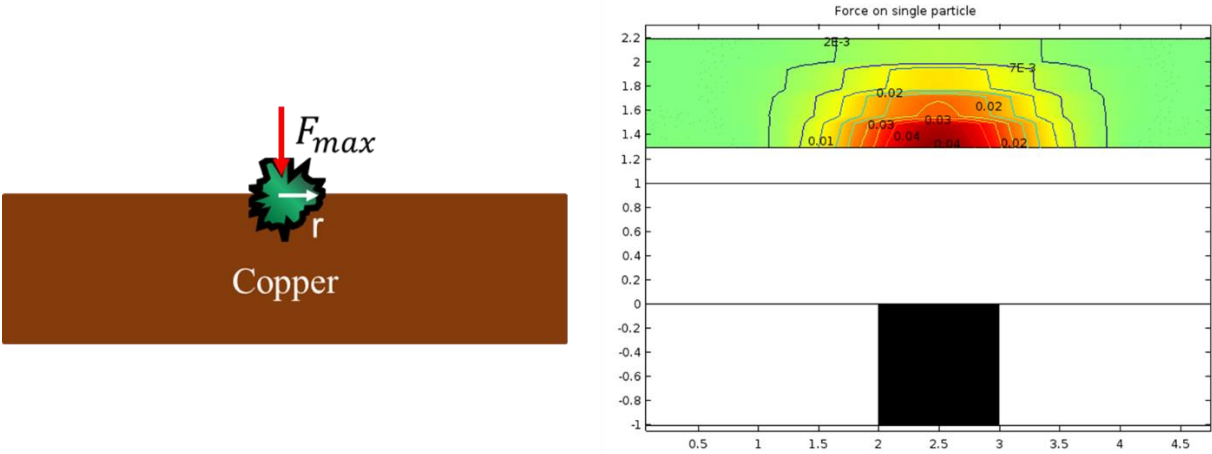


Figure 3.27: model of abrasive particle and the force being calculate (left). Computational calculation of force on a single particle (in N) (right)

3.2.3.2.2. Velocity

Increasing the particle velocity allows more material to be removed per unit time (Eqn.1) and the increment in particle velocity can be obtained by increasing magnet velocity. Two factors limit the speed of the system: (1) experimental setup; and (2) rheological limitations. The first limitation depends on the components of the system, such as the actuator, micro-controller, and motor driver circuit. The current experimental setup allows speeds up to 20 cm/s after which point the H-bridge circuit overheats and the system shuts itself down. The rheological limitations limit the speed at which the slurry can move. As such, even if the magnet can move faster, the slurry (mostly the iron particles) cannot move in synchrony with the magnet. We believe that this is because the magnetic forces acting on the magnetic particles are not large enough to accelerate them if the interaction time is short (magnet motion frequency is high). This phenomenon was observed during experimentation and the process was operated below the observed limit at a speed of 20 cm/s.

3.2.3.2.3. Abrasive and magnetic particles

The effects of abrasive and magnetic particles on the abrasion process are not immediately evident. Research has shown that the wear coefficient, $\tan\theta$, is affected by the abrasive particle size, shape, and material [20–22]. Examining Figure 3.28, the wear coefficient increases as the size of the particles increases [21], indicating that larger particles can remove more material. This is preferred to remove the initially rough layer consisting of big asperities as illustrated in Figure 3.28. Second, the wear coefficient increases as the shape of the abrasive particles diverges from a sphere. This divergence increases the number of abrasive edges to increase the sharpness. Third, the wear coefficient depends on the material the abrasive particles are made from. Depending on the hardness of the material, the sharpness changes drastically as shown in the values for alumina and silicon carbide and diamond [190]. With these effects and cost of particles in mind, non-spherical silicon carbide particles and non-spherical alumina particles were chosen as the abrasives in the prototype tests.

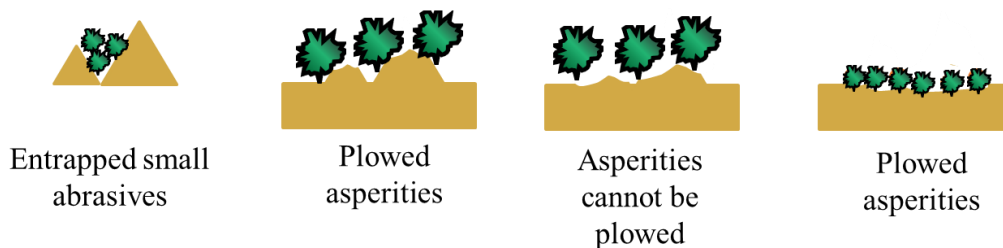


Figure 3.28: Material removal process is conceptualized to show how the size of the abrasive particles can affect the overall material removal.

By contrast, the effect of iron particles on abrasion depends strongly on their concentration, instead of their physical properties. The concentration of iron particles that come into contact with abrasive particles changes the total force experienced by the abrasive particles. Assuming that one iron particle can only contact one abrasive particle at any given instant, the force experienced by the abrasive particles, and hence the material removal rate, increases as the concentration of the iron particles increase. However, the material removal rate across the whole work piece surface decreases if concentration of the iron particles is too high because the number of abrasive particles has to be reduced to accommodate the increase of iron particles. As such, there is an optimum iron particle concentration in which the process should operate. This range is characterized for the simplified model and is shown in Figure 3.29 at 50%.

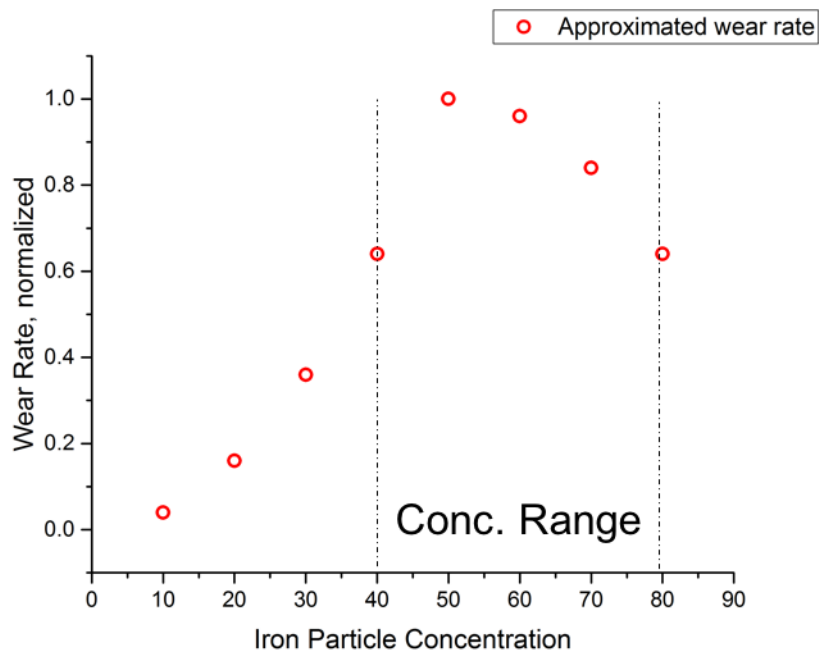


Figure 3.29: Normalized wear rate vs. iron particle concentration. The wear rate calculated for each concentration is normalized by the maximum achievable wear rate.

3.2.3.3. Experimental Setup, Results, and Discussion

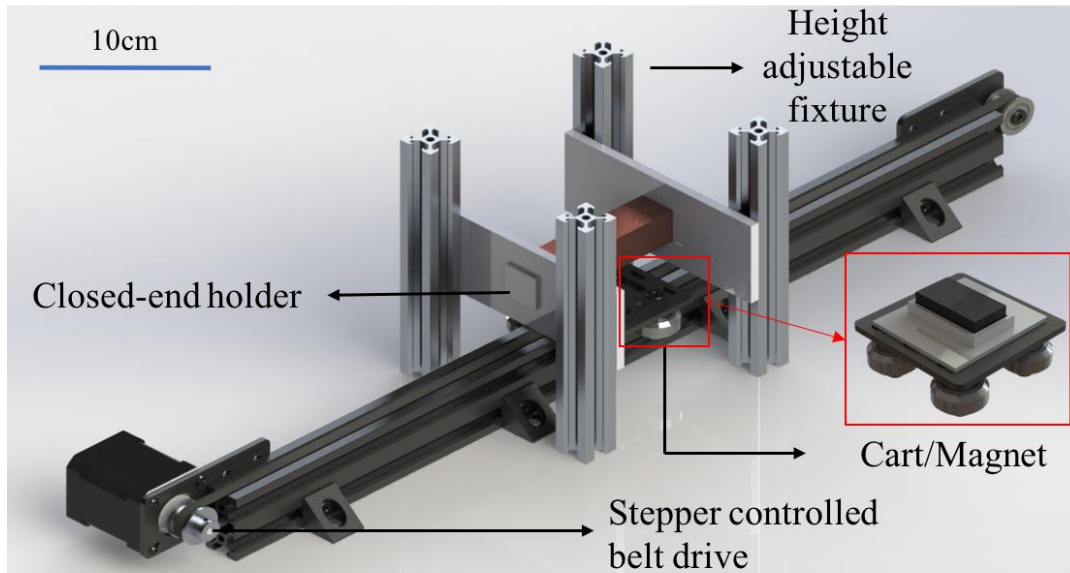


Figure 3.30: 3D rendering of conceptual experimental setup highlighting key components.

As outlined and explained in the previous section, this model relies on an oscillating magnetic field and the motion of the magnetic abrasive slurry with this magnetic field. The goal is to ensure that the abrasive particles move together with the magnetic particles under the influence of an external magnetic field. This is done partially by using a highly viscous media as the carrier fluid (e.g. Glycerol) so that the abrasive and magnetic particles move together. Figure 3.30 shows the conceptual experimental setup highlighting key components. As described previously the factors that affect the process are as follows: (1) concentrations of the magnetic and abrasive particles, (2) size and shape of the abrasive particles, (3) travelling distance and frequency of motion of magnets, (4) viscosity of the carrier fluid, (5) number of abrasion cycles. Furthermore, it is a well-established fact that the surface smoothness will increase up to a certain point with increasing number of abrasion cycles [168,170,195]. In order to assess the effects, the following experiments were designed.

The carrier fluid was chosen as glycerol since it was used previously by [176] for similar abrasion processes due to its high viscosity (2000 cps), its good lubrication properties, and its non-reactive nature, especially with ABS since that is the material used for the experimental setup. The carrier fluid wt% was taken as 10% since it was shown that for effective abrasion to take place the lubricating fluid should not be more than 10% [196,197]. The traveling distance is chosen as 10 cm for all experiments since the length of the experimental setup holding the work piece and the slurry was designed as 10cm from the simulation results presented previously.

Figure 3.31 shows the wiring diagram for the experimental setup and Figure 3.32 shows the optical photo of the setup, consisting of the holding piece, linear rail system with belt drive, controller

(Arduino) and circuitry, and computer to run LabView, which was used as the control software using a specially designed interface using the LabView interface for Arduino (LIFA) library.

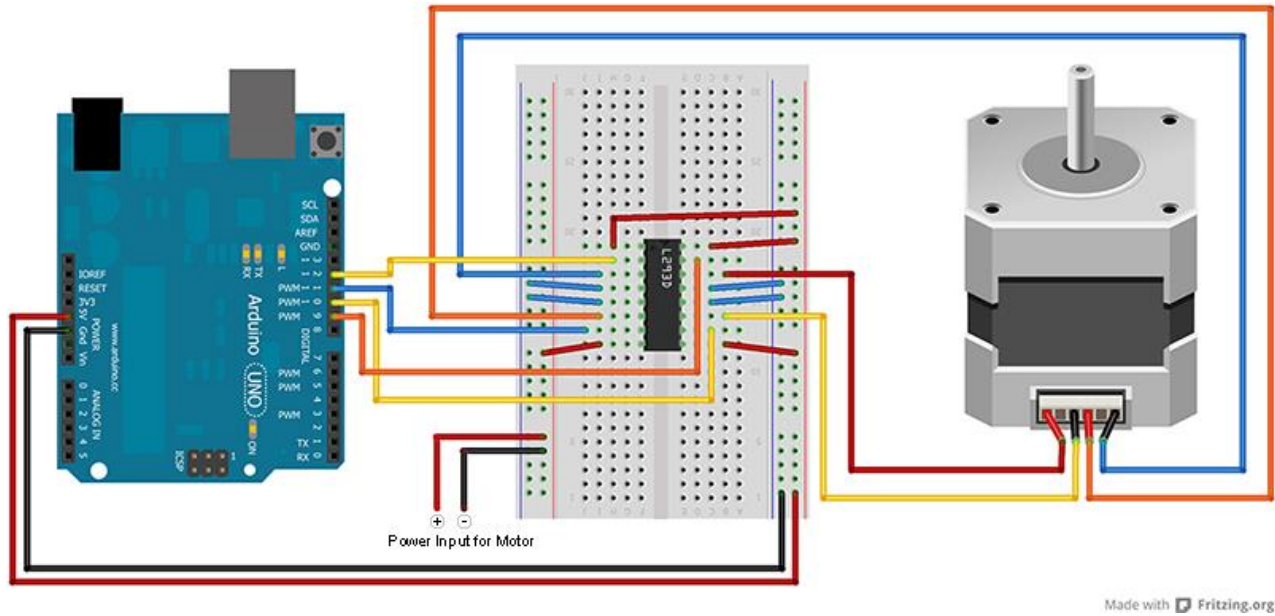


Figure 3.31: Wiring diagram for stepper motor driving the linear belt drive system.

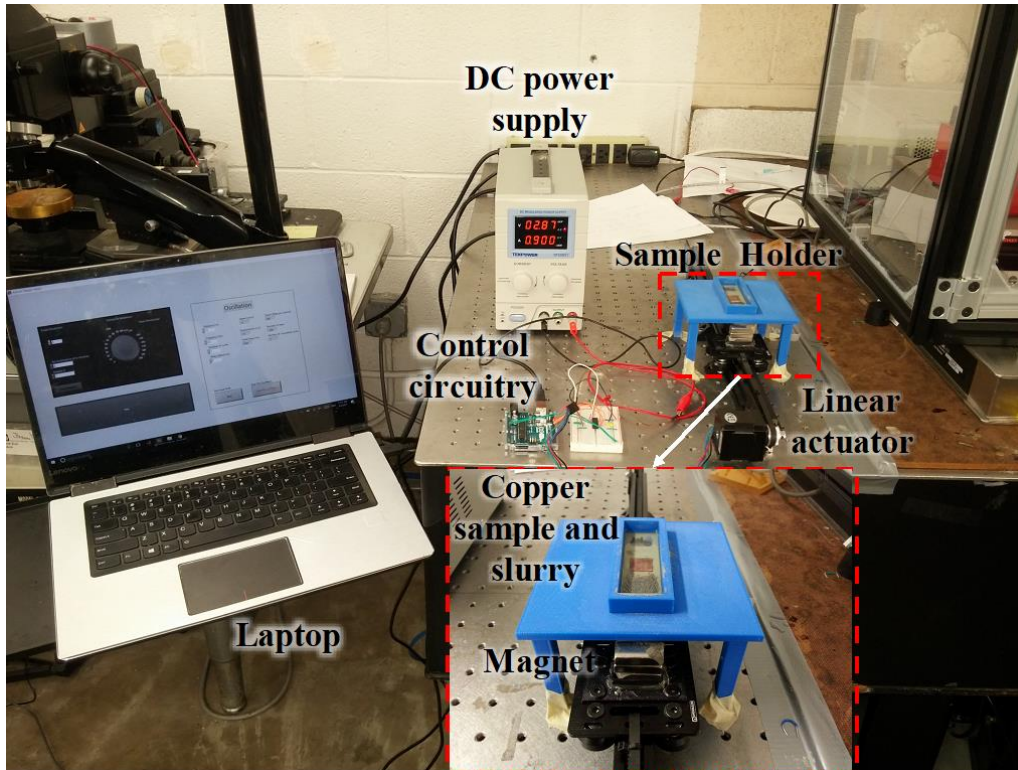


Figure 3.32: An optical photo of the experimental setup.

Figure 3.33 shows the preliminary interface designed for this system. It allows easy control of motion amplitude, frequency, and number of abrasion cycles. This controller also has a vision system that can be used to monitor the process, which will be of importance in the future when a fully closed system will be designed.

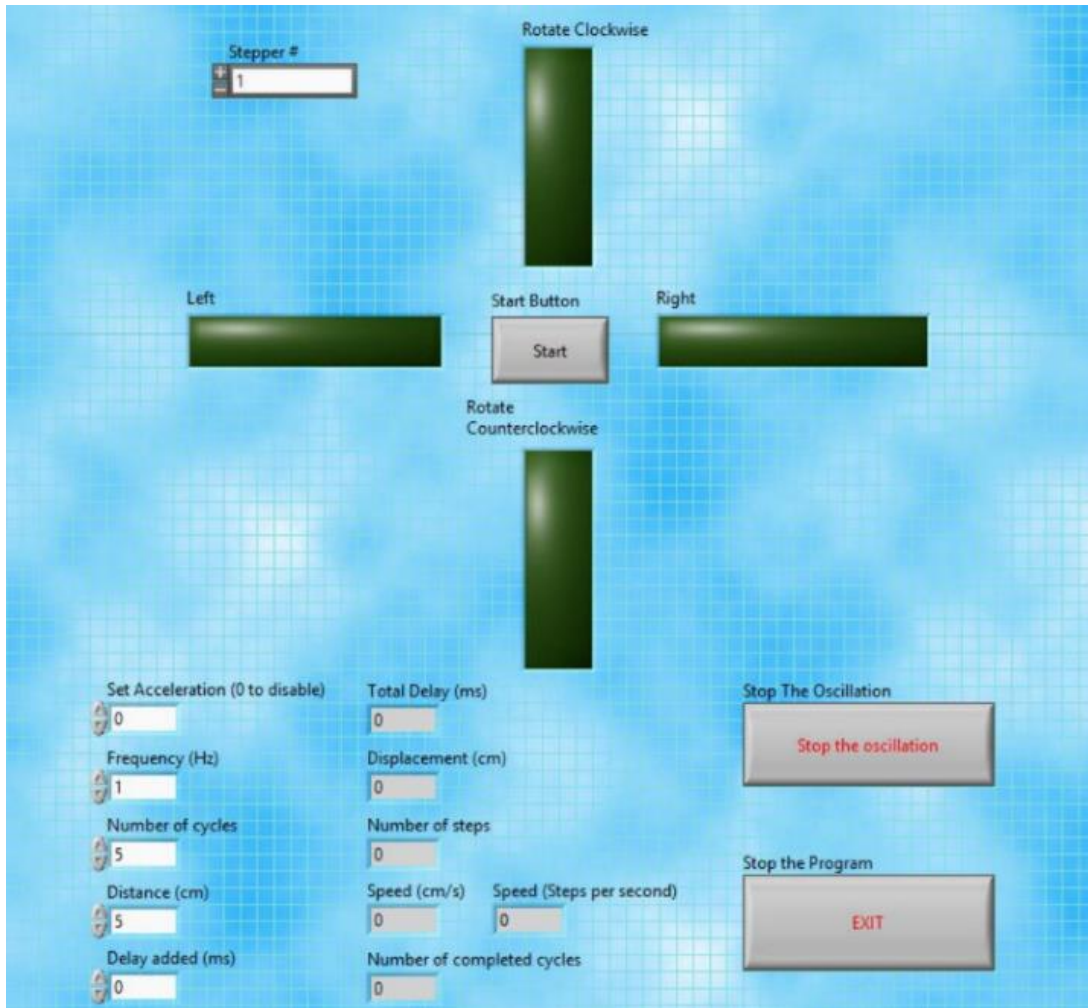


Figure 3.33: Graphical user interface used to control the process parameters and the position of the permanent magnet.

A NEMA17 stepper motor, capable of delivering 45 N.cm torque, is used to actuate the belt drive system; however, this motor is limited to approximately 800 steps/sec of motion speed. Depending on the amplitude and frequency of the motion required, this corresponds to different linear speeds. Figure 3.34 shows the magnetic abrasive slurry used in experiments and the consecutive time-step photos showing the motion of the magnetic abrasive slurry under the effect of the magnetic field. The slurry can follow the movement of the magnet and can pass over the copper sample for smoothing it in the process. For the reader to understand the overall motion, the time-step image shows from a video of one abrasion cycle at 0.5 Hz with a travelling distance of 10 cm sampled at 0.2s.

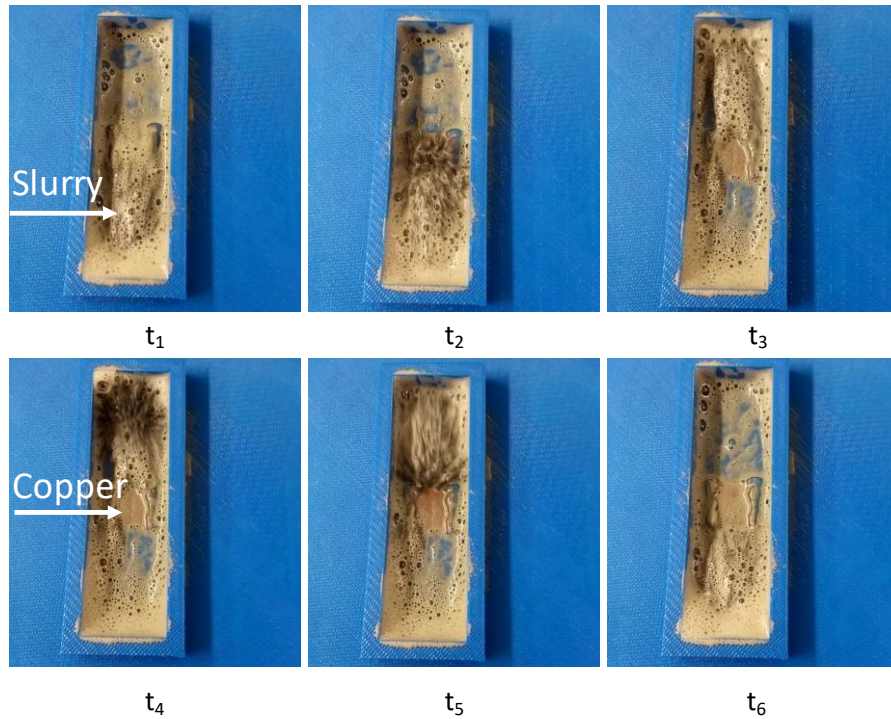


Figure 3.34: Motion of the magnetic abrasive slurry under the influence of an external translational magnetic field. The images are taken in 0.2s intervals and the 6 images show 1 full cycle.

Initial results can be seen in Table 3.5 and Figure 3.35. The results show the surface roughness improvement achieved using various sizes of particles for 2000 cycles and 3000 cycles. The number of cycles can be increased to achieve smoother surfaces. As indicated in the theory portion of this section, the particle size used in the process needs to be similar to the surface roughness such that the particles are not smaller than the voids that exist on the surface or the particles can get stuck in these regions, which causes the increase of surface roughness due to particle trapping and contaminations. The samples are cleaned using ultra sonication in IPA for 20 minutes after the abrasion process is completed.

Table 3.5: Experimental results of different process parameters including particle type, shape and number of cycles.

Particle	Process Parameters (# cycles, frequency and travelling distance)	Initial Ra	Processed Ra	% Decrease
SiC 30 μm	2000 cycles @ 0.5Hz and 10cm	30.5 μm	22.3 μm	26%
SiC 15 μm	2000 cycles @ 0.5Hz and 10cm	40.47 μm	33.11 μm	17.5%
SiC 30 μm	3000 cycles @ 0.5Hz and 10cm	30.6 μm	18.25 μm	40%

SiC 15 μm	3000 cycles @ 0.5Hz and 10cm	30.5 μm	21.5 μm	30%
SiC 30 μm + SiC 15 μm	3000 + 3000 cycles @ 0.5Hz and 10cm	30.2 μm	16.7 μm	44.7%

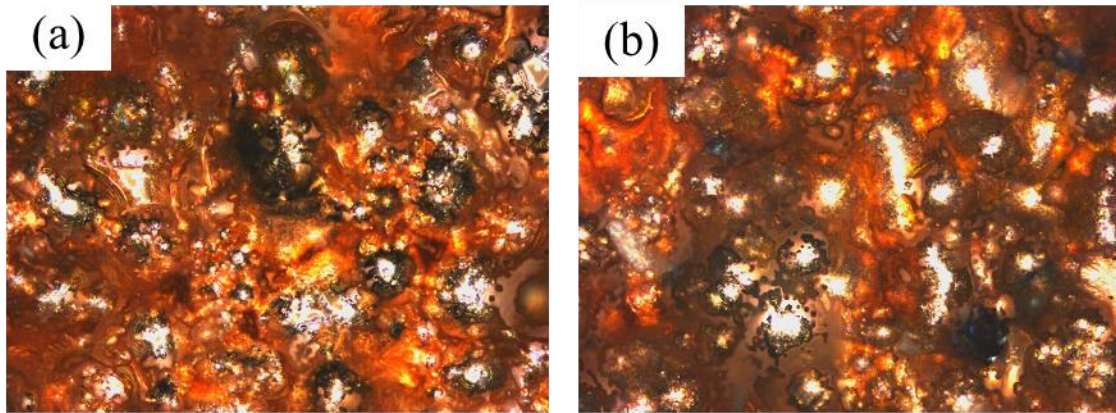


Figure 3.35: Processing results compared to as-fabricated samples. (a) The as-fabricated sample has many asperities, mostly due to unfused particles. (b) The processed sample has a smoother texture and less visible unfused particles

Further optimizations in terms of process parameters were conducted to achieve the surface finish required by the application. The particle concentration and the number of polishing cycles were experimentally studied. The surface roughness of the samples was analyzed by confocal microscopy after each polishing step. By optimizing these two parameters, a surface roughness (Ra) of 4 μm was achieved as shown in Figure 3.36. Further polishing using the same experimental setup and sample did not improve the surface roughness. This is believed to be due to the initial surface morphology which included voids on the surface resulting from the fabrication process.

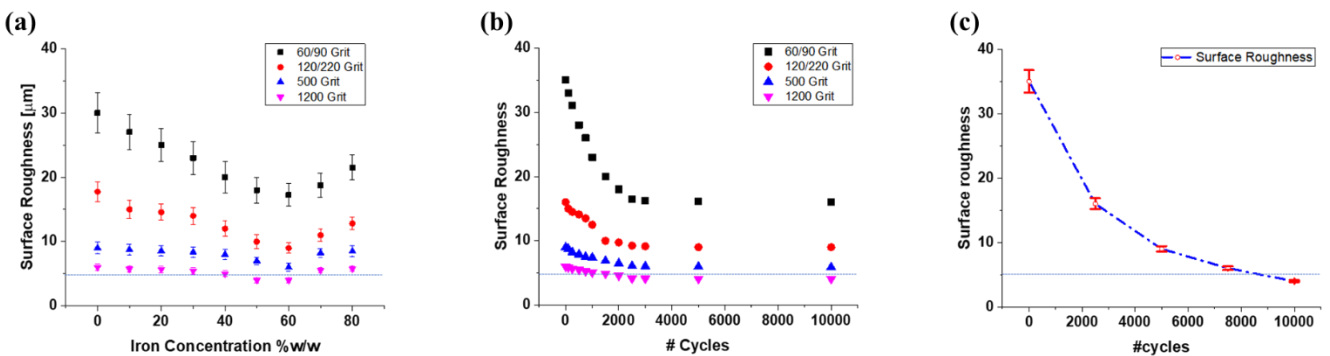


Figure 3.36: Process optimization. (a) Particle concentration optimization, (b) Process cycle optimization, (c) Full polishing cycle on a single sample.

The particle concentration affects the force on each abrasive particle and the total number of abrasive particles acting on the surface. The analytical model shows that an iron particle concentration in the range of 50-70% w/w would be the optimal for material removal/polishing as shown in Figure 3.29. Figure 3.36a shows the experimental polishing results that for all 4 polishing particle systems, the best surface finish was achieved using 60% w/w iron particles in all systems, which is similar to previously reported values for three-body abrasion processes [20]. Moreover, it is seen that iron particle concentration is more important in the initial polishing step in Figure 3.36a because large surface asperities exist on the surface initially. By reducing them, the later polishing steps are less affected by the change in particle concentration and operate well within predicted concentration range. A 4-step polishing process was designed by changing the particle systems to smaller sizes using the best polishing results from the previous step, a minimum surface roughness of 4 μm was achieved. The number of cycles for each step was conducted for 10,000 cycles and a steady decrease in surface roughness was seen. Specifically, using the 60/90 grit abrasives, the surface roughness was decreased from 30 μm to 18 μm , resulting in a 33% decrease. The next polishing step resulted in a 44% decrease, giving a surface roughness of 10 μm . The 500 grit silicon carbide particles used in the third step reduced the surface roughness to 6 μm . Finally, the 1200 grit alumina particles reduced the surface roughness to 4 μm . To determine the number of cycles required to reach a steady state surface roughness samples were polished using the four different abrasives for various number of polishing cycles. By conducting these experiments, the time required to fully polish the samples was determined. A total of 100 to 10,000 cycles were tested for each slurry type as shown in Figure 3.36b. It is observed that 2250-2500 cycles were needed to polish the samples to a certain steady state roughness value dictated by the initial surface morphology. After 2500 cycles for all four different abrasive slurries, not much change in surface roughness was seen. This can be attributed to two different effects: (1) initial surface morphology and (2) dulling of the abrasive particles. To reduce the number of cycles needed, the magnetic force and the magnet movement speed should be increased. After optimizing the process in terms of the particle concentration and number of polishing cycles, a 0.5in x 0.5in x 1mm sample was polished. The surface roughness (R_a) was measured to be 35 μm and each different kind of abrasive slurry was used for 2500 cycles. After a total of 10,000 cycles, the sample was polished to a surface roughness of 4 μm , as shown in Figure 3.36c. Figure 3.37 show the polished surface without the agglomerated particles and the surface is smoother compared to its original state. However, the surface roughness did not decrease further due to the voids on the surface as seen in the SEM image.

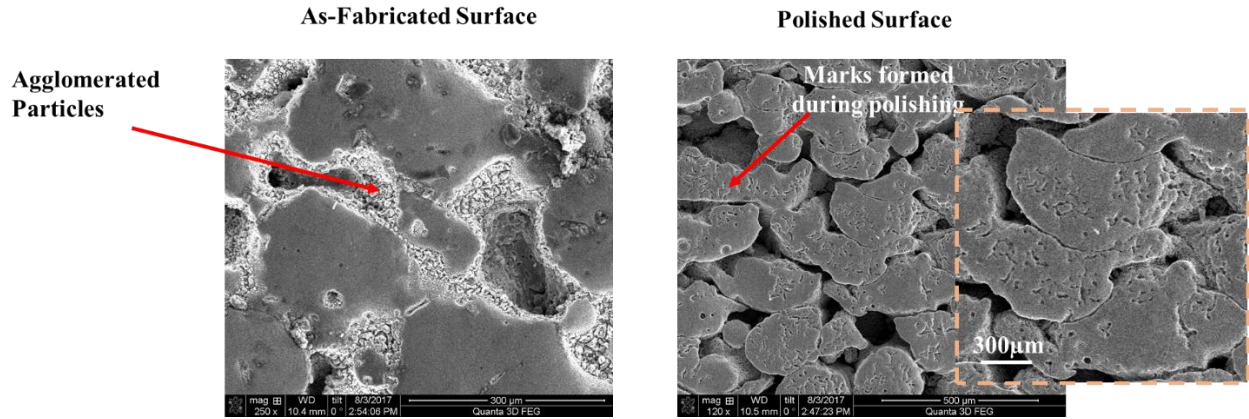


Figure 3.37: SEM images comparing surfaces pre (left) and post-polishing (right)

After investigating all the parameters affecting the process with optimizations, an improvement of approximately 10X better surface roughness has been achieved. However, the operating window of the waveguide structure at 90 GHz require further reduction in surface roughness. In order to achieve this goal for the 3D-printed waveguide functions, improvements were made on the fabrication side at NCSU CAMAL to reduce the initial surface roughness of the structures down to 25µm and reduce voids present on the surface. With this enhancement, the new structures were polished down to sub 2 µm surface roughness as shown in the pre- and post-polishing samples in Figure 3.38. The SEM images also show the stark contrast between as fabricated samples and polished ones. With the key visual aspect being, a drastic reduction in the number unfused copper particles on the surface.

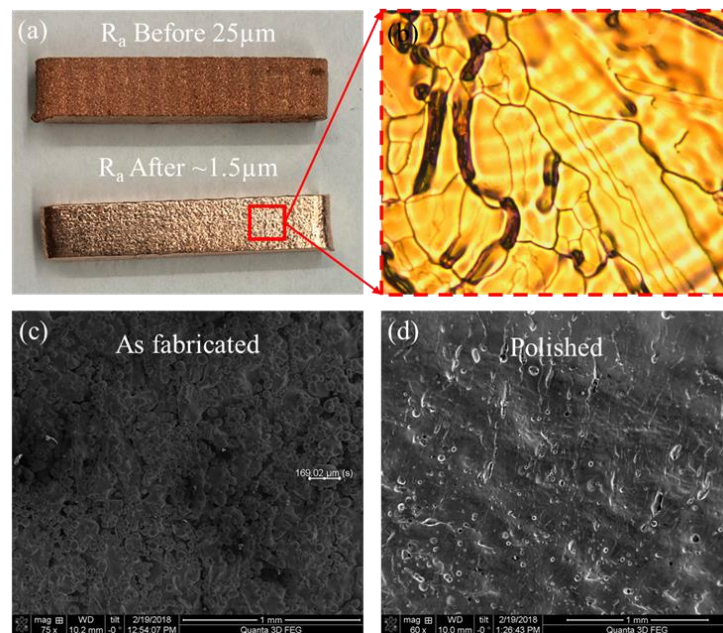


Figure 3.38: Post fabrication improvement samples before and after being polished: (a) visual comparison of polished and unpolished samples; (b) enlarged light microscopy image of surface after the polishing process; (c) SEM image of as fabricated sample; (d) SEM image of polished sample.

After achieving the sub $2\mu\text{m}$ surface roughness, the polishing method was modified to work on real waveguide structures. The conceptual image of the modified polishing setup is shown in Figure 3.39 with the addition of a height-adjustable sample holding jig as well as the connections that were made to the waveguide structures. These connecting elements were designed much like a channel such that they could house the necessary slurry during polishing.

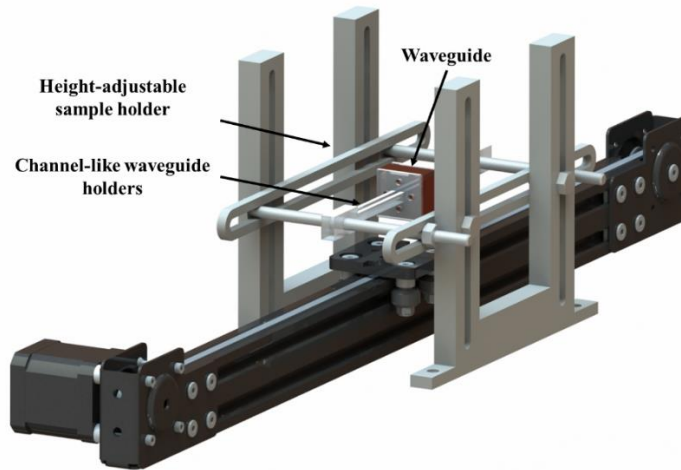


Figure 3.39: Modified experimental setup.

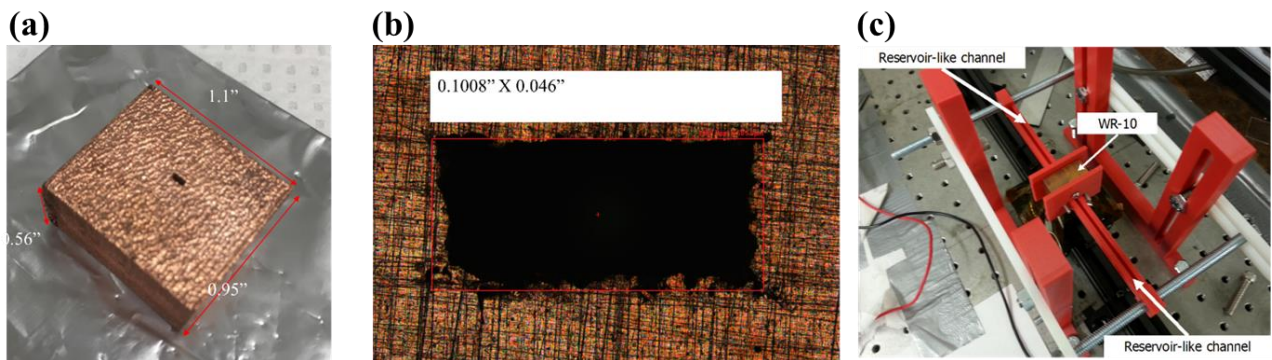


Figure 3.40:(a) Half-inch waveguide; (b) Waveguide cross-section; (c) Waveguide attached to experimental setup.

The waveguide structure shown in Figure 3.40a with a length of 0.5in was fabricated and the experimental setup was constructed. The optical photo is shown in Figure 3.40c. Initial signal transmission and loss experiments (conducted by UC Davis) yielded a 3dB decrease in signal loss as seen in Figure 3.41. Further studies should be conducted into polishing full waveguides and measuring how the performance changes with polishing, as well potentially adding electromagnets

to enhance the magnetic field strength and investigating other magnetic and abrasive particles to reach the sub-micron surface finish required for VEDs.

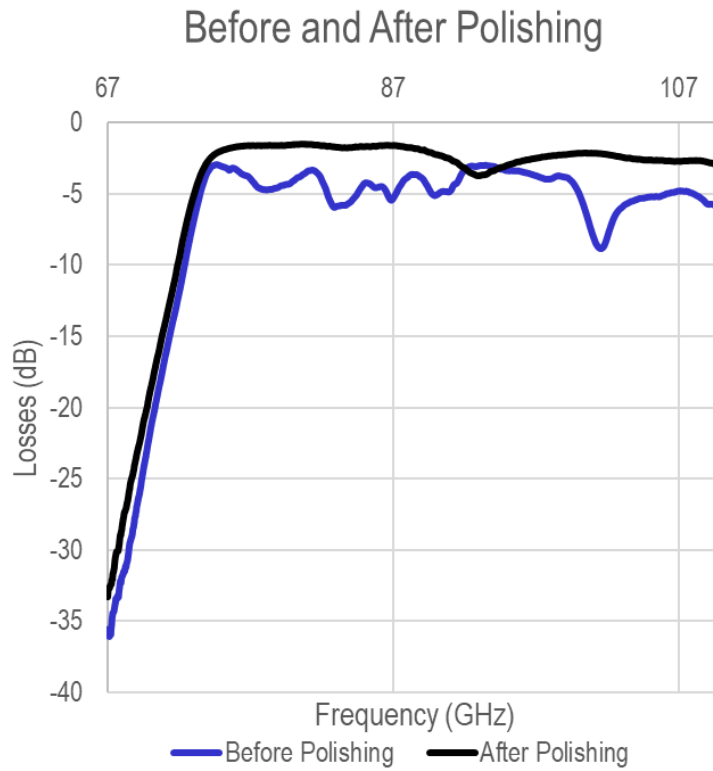


Figure 3.41: Signal losses in waveguide structure fabricated in figure 3.40.

3.3. Conclusion

The goal of this chapter is to tackle the issues surrounding surface finishes (roughness) of 3D printed parts, with specific emphasis on enclosed surfaces fabricated via metal 3D printing processes. To tackle this issue, vacuum electronic devices which are fabricated from copper particles and the require near mirror-like surface finishes is chosen as the application area. The chapter first introduces specific background information including the electron-beam based metal additive manufacturing principles. A review of different internal surface polishing techniques is given and two alternative methods for polishing enclosed 3D printed surface are proposed: electrochemical polishing and abrasive flow polishing techniques. Electrochemical polishing is investigated as a promising method; however, its shortcomings are soon realized prompting the need for another polishing method. Drawing inspiration from abrasive flow polishing techniques, a novel magnetically driven abrasive flow polishing technique is developed. The factors affecting this process are investigated in details and major improvements are made to achieve the reduction of the initial surface roughness from $40\ \mu\text{m}$ to $1.5\ \mu\text{m}$. Further improvements can be made to the system to enable multi-axis motion and polishing of different materials.

4. Chapter 4: Conclusion and Outlook

4.1. Conclusion

In this dissertation, 3D printing and post-processing techniques for surface functionalization and surface roughness improvement have been described. Chapter 1 introduced the most common 3D printing techniques and their technical bottlenecks. In Chapter 2, the technical challenge of incorporating functional materials and functional surfaces using 3D printing has been addressed by developing a post-fabrication process to create energy harvesting devices. Chemical vapor deposition was used to coat 3D printed structures with various types of Parylene materials to create piezoelectret energy harvesters. While tackling the issues surrounding 3D printing, additional challenges in the fabrication of electret-based energy harvesters are also discussed. A multi-layer highly flexible energy harvester has been designed and fabricated as a simpler way for multi-layer electret devices to enhance the performance. Testing results showed that by utilizing 100 nm-thick Parylene AF4 as the coating material, a power output of $12.5 \mu\text{W}/\text{cm}^2$ has been harvested by 3-Newton force applied at 2 Hz. Due to the relatively thin coating and lower surface charge density of Parylene AF4, the power output is low as compared with other reported values of similar electret energy harvesters. To combat this issue, the use of multi-material 3D printing with Parylene C coating has been investigated. A thicker coating of 10 μm in thickness has been applied and longer time period of the charging process has been utilized to increase the surface charge density. This results in a 50X increase in the surface potential and a peak power output of $8 \mu\text{W}/\text{cm}^2$ from a single-layer energy harvester. Even though these initial results are promising, further testing should be conducted to investigate other issues, such as the optimization of process parameters and the life-time use of these devices. Finally, different electret materials should be investigated to determine if there are other CVD-compatible electret materials with higher surface charge density to increase device performances.

In chapter 3, the goal is to tackle the issues of the surface roughness for 3D printed structures, with the specific emphasis on enclosed surfaces. such as waveguides in vacuum electronic devices fabricated from oxygen free high conductivity copper with near mirror-like surface finishes. Two alternative methods for polishing enclosed 3D printed surface have been proposed. First, electrochemical polishing is investigated but its shortcomings are soon realized prompting the need for a novel polishing method. These shortcomings include the position of the electrode with respect to the polishing surface, and the need for fresh electrolyte close to the polishing surfaces which can be relatively hard to achieve in an enclosed structure. Drawing inspirations from the abrasive flow polishing technique, a novel magnetically driven abrasive flow polishing technique is developed. The factors affecting this process are investigated in details and major improvements are accomplished by decreasing the initial surface roughness (R_a) of 3D printed copper structures from 40 μm to 1.5 μm . Further improvements can be made to the prototype system to enable multi-axis motions to polish different materials. Process optimization will be needed, and certain limitations may exist in terms of 3D motion control of magnetic particles.

4.2. Outlook & Future Works

Although initial applications and results are shown throughout this dissertation, several applications and potential improvements can be investigated both for the 3D printed energy harvesting devices and for the polishing of 3D printed surfaces. In terms of 3D printed energy harvesting, different coating materials, such as PET, PTFE, and other high surface charge density electrets, as well as other structural materials, such as different silicones, should be investigated to both increase the electret performance and achieve required mechanical properties. In the areas of wearable electronics and other soft robotics, applications can be specifically targeted in the future. Two applications are presented below to highlight the potential use of the fabrication process developed in chapter 2 in the field of wearable electronics and soft devices. For the future development of polishing techniques, additional process optimization can be done to further reduce the surface roughness, while the effect of particle contamination on device performance of the treated structures should be investigated. Furthermore, more freedom in the motion axis could be increased to allow for the polishing of more complex structures.

4.2.1. 3D printed Energy Harvesters and soft devices

4.2.1.1. General direction of wearables and other soft devices

With advances in healthcare and virtual interaction (AR/VR wearable systems) applications, both sensors and actuators are becoming more important. There are still challenges that remain in realizing such devices: (1) sensor/actuator stiffness and flexibility, (2) fabrication of soft devices on an industrial scale, (3) performance degradation of soft devices under excessive use, and (4) seamless integration of sensors and actuators into a single device. Some of the techniques covered in this chapter can be used to mitigate these issues with clever designs and advances in materials processing and fabrication for industrial scale devices. Once these hurdles are overcome, many possibilities exist. In recent years, technology firms such as Facebook, Apple, and Google have invested heavily in making wearable devices. There is still more to be accomplished in this field both from an academic and industrial standpoint. For future directions of what the research presented in chapter 2 can enable, two applications are covered: (1) the fabrication of a wearable glove-like device that has distinct sensor and actuator functions for haptic feedback systems, and (2) novel ideas to integrate electret-based energy harvesters to automobiles and other vehicles with rubber-based tires.

4.2.1.2. Wearable all 3D printed glove

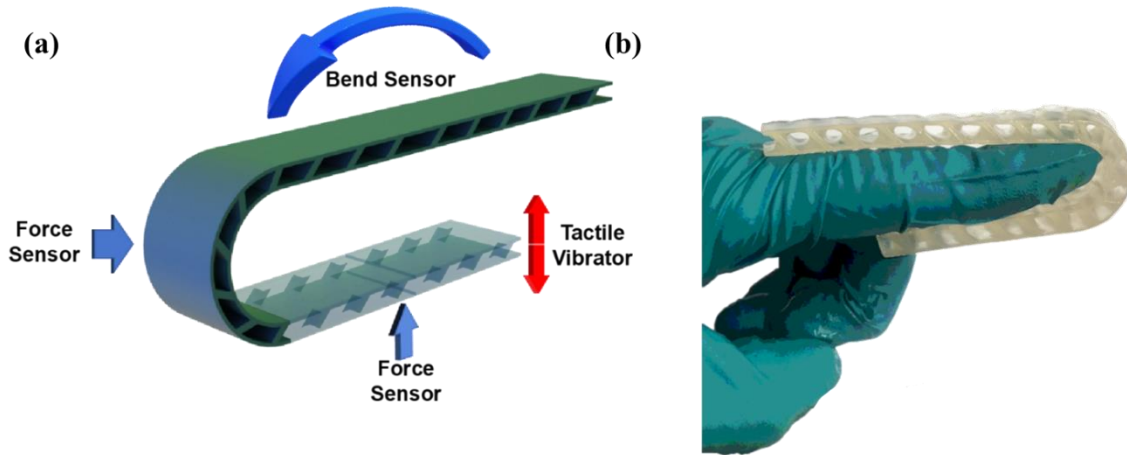


Figure 4.1: (a) conceptual device with three different sensors and one actuator. (b) Device on the finger.

By building on the techniques developed throughout Chapter 2, one application for a wearable glove-like device with integrate sensors and actuators could be realized with a single fabrication process. The device concept seen in Figure 4.1a consists of three sensors (two force sensors and a bend sensors) and a tactile vibrator for haptic feedback. The overall concept is fairly similar to many wearable AR/VR glove concepts while this device utilizes 3D printing and the electret principles to create a fully integrated device in a single fabrication step. The 3D printed structure seen in Figure 4.1b is fabricated using the DLP printing process. A new material is used in order to create a more flexible device that could both bend and vibrate. The printing resin consists of 33 wt% Isobornyl Acrylate, 2wt% Diphenyl(2,4,6-trimethylbenzoyl)phosphine oxide (TPO) as the photoinitiator, and 75% Aliphatic Urethane Diacrylate (AUD). It has been previously shown that this novel photochemistry could be used to achieve highly stretchable polymers capable of stretching up to 1100% strain which is more flexible than that of most commercial UV curable elastomers [15]. However, to achieve the layer thickness ($\sim 100\mu\text{m}$) for this application, the original photochemistry of epoxy aliphatic acrylate hasn't been used. By mixing the chemicals in the given amounts and stirring at 85°C , the 3D printing resin is obtained to be poured into the modified 3D printing system capable of heating the resin vat up to 70°C using a thermal controller and high-power heating tapes. Using 385 nm wavelength UV lights operating at 40 Watts, each layer could be cured in 15 seconds. The modified system can be seen in Figure 4.2 and the 3D printed samples are subsequently cleaned using IPA and then dried for 1 week in ambient condition. These samples are then coated with Parylene C.

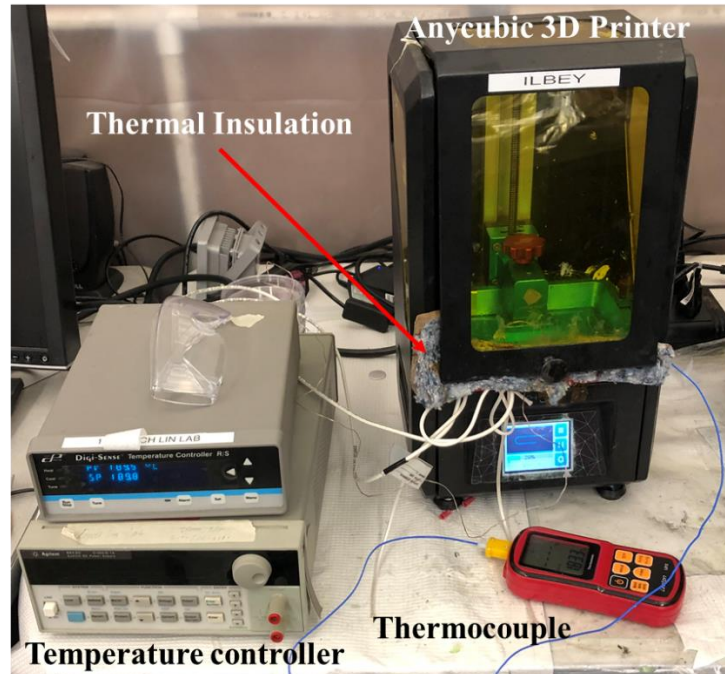


Figure 4.2: A modified 3D printing system

Further works for this specific application include the corona charging step to functionalize the electret surfaces, and tests for sensor under various loads and frequencies as well as the tests for the actuator system.

4.2.1.3. Tire energy harvester

The second future direction that can be realized through the fabrication method presented in Chapter 2 is the integration of energy harvester in rubber-based tires in the automobile industry. As a dynamic system, automobiles have the potential to recycle some of the energy via energy harvesting such as those used in the braking systems (regenerative braking) which do not interfere with vehicle performance and are currently being used commercially (i.e. Nissan Leaf) [198]. Tire companies have also taken initiative in developing airless tires to overcome environmental concerns. According to Michelin, 200 M tires/year are scrapped due to irregular wear and 12% of these tires are caused by blowouts. By making air-free tires, nearly 24 M tires each year could be saved from getting scrapped reducing the environmental impact [199]. Furthermore, airless tires will not require spare tires to reduce vehicle weight and possible lower rolling resistance to result in an increase in fuel economy [200]. Some concepts from different tire companies are seen in Figure 4.3.



Figure 4.3: Different airless tire concepts from commercial companies. (a) Bridgestone airless tire [201]; (b) Michelin airless tire [202]; (c) Goodyear Turf Command airless tire [200]; (d) Michelin airless tire on a real EV [199].

When these concepts are investigated, the overall structure resembles the electret structures developed in the previous sections. The materials used are also similar and the continuous rotary motion of the tire combined with the displacement that occurs between the inner and outer circle of the tire are analogous to how the electret devices work. As such, the concept of using Parylene coating on airless tires becomes a very attractive concept for the airless tires. To test this idea, the following concept and experimental setup are conceived. The outer and inner ring electrodes will act as the metal layer, while the middle section will be the flexible separation layer covered with Parylene C. A simple design resembling the actual design of the Michelin tire fitted to the Chevrolet Bolt EV is analyzed in COMSOL Multiphysics (Figure 4.4) and the displacement that can be obtained is examined.

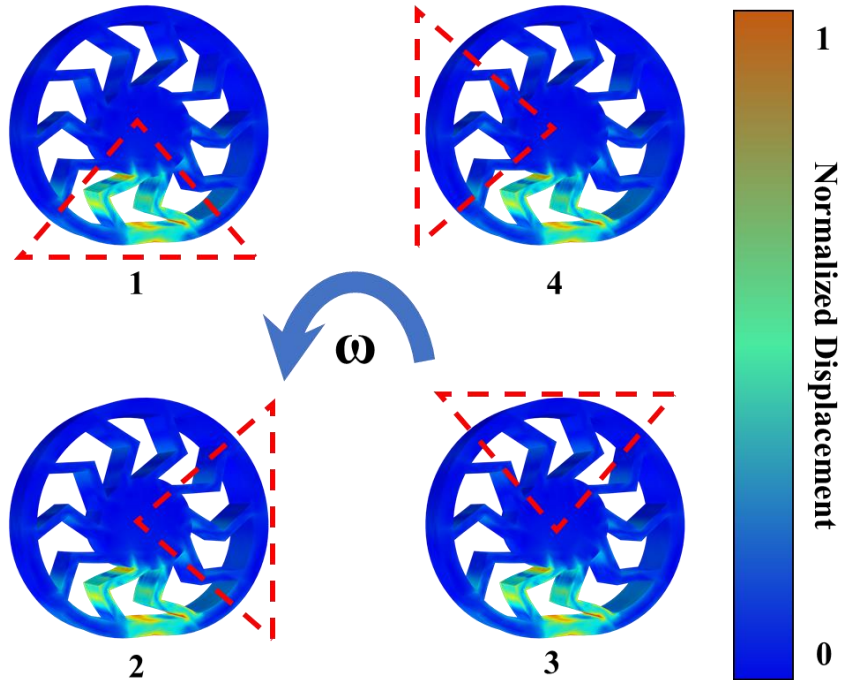


Figure 4.4: COMSOL Multiphysics simulation highlighting the displacement of the outer tire with respect to the inner wall.

The experimental setup in Figure 4.5 is conceptualized. The springs at both ends of the shaft would be used to adjust the load on the tires while the shaft would rotate controlled by a stepper motor at one end. An electrode strip would be placed underneath the tire as the contact electrode to connect to the current preamplifier while the shaft and the inner hub would be used as the inner electrode. By measuring the energy can be harvested for different vehicles, the overall figure of merit for such a system can be calculated.

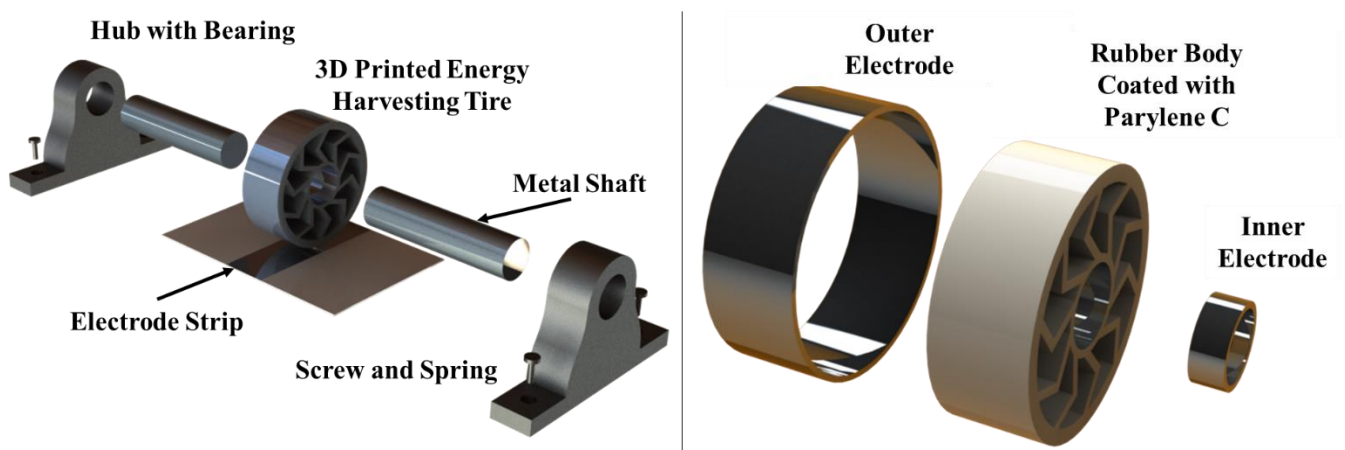


Figure 4.5: Experimental setup concept to test the potential applicability of this idea to road vehicles

Some samples have been prepared and printed for tests but the fabrication process could not be completed due to the unexpected closures due to COVID-19. Some prototype samples are shown in Figure 4.6, still on the 3D printing build platform.

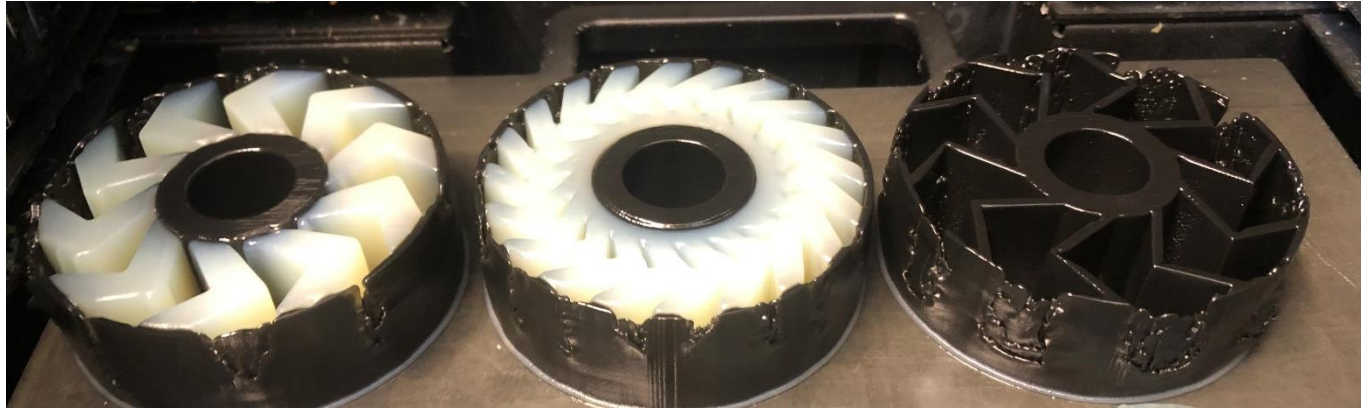


Figure 4.6: 3D printed airless tire concepts

4.2.2. Metal 3D Printing Polishing

The system developed in Chapter 3 can polish structures with 1 axis of motion on the magnets. However, the increasing design complexity can result in a complex structure such as motions in the multiple axes for the control of magnet would be desirable. The current experimental setup needs to be further expanded to 2D motions (Figure 4.7) and even further on to 3D motions. Considering the insights gained from the results of this method, potential pitfalls do exist in transferring this technique into 2D and 3D motions. Such pitfalls include, but are not limited to: moving particles around the turns, long processing time due to the overall length of the structures, and the need of different workpiece holders for various channel geometries. Nevertheless; the proposed scheme is a unique and interesting technique that is capable of polishing enclosed surfaces and can be applied to other areas such as microfluidics where surface roughness is also of extreme importance [16] or other 3D printed materials with further investigations.

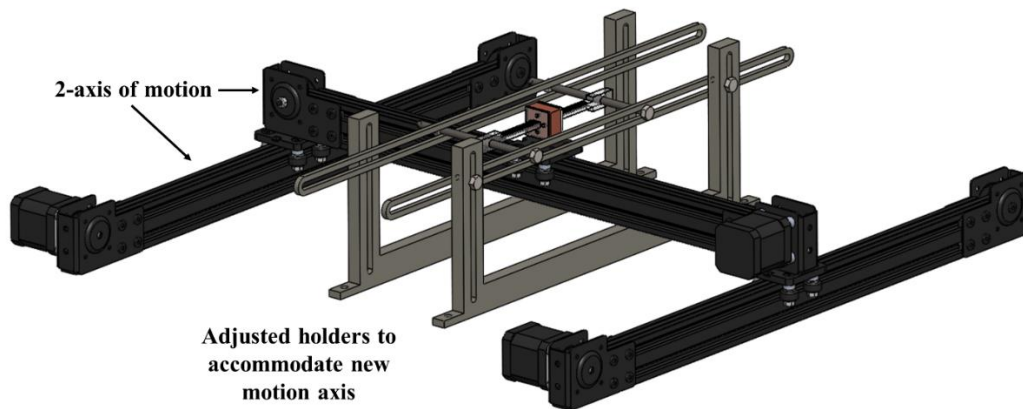


Figure 4.7: A 2D motion polishing system.

References

- [1] B.P. Conner, G.P. Manogharan, A.N. Martof, L.M. Rodomsky, C.M. Rodomsky, D.C. Jordan, J.W. Limperos, Making sense of 3-D printing: Creating a map of additive manufacturing products and services, *Smart Mater. Struct.* 1 (2015) 1310–1311. <https://doi.org/10.1049/el.2015.2186>.
- [2] W.E. Frazier, Metal additive manufacturing: A review, *J. Mater. Eng. Perform.* 23 (2014) 1917–1928. <https://doi.org/10.1007/s11665-014-0958-z>.
- [3] P. Shakor, S. Nejadi, G. Paul, S. Malek, Review of emerging additive manufacturing technologies in 3d printing of cementitious materials in the construction industry, *Front. Built Environ.* 4 (2019) 85. <https://doi.org/10.3389/fbuil.2018.00085>.
- [4] NASA's Centennial Challenges: 3-D Printed Habitat Challenge | NASA, (n.d.). https://www.nasa.gov/directorates/spacetech/centennial_challenges/3DPHab/index.html (accessed April 9, 2020).
- [5] Relativity Space — Relativity Space, (n.d.). <https://www.relativityspace.com/terran> (accessed October 22, 2019).
- [6] J.-P. Kruth, M.C. Leu, T. Nakagawa, Progress in Additive Manufacturing and Rapid Prototyping, *CIRP Ann. - Manuf. Technol.* 47 (1998) 525–540. [https://doi.org/10.1016/S0007-8506\(07\)63240-5](https://doi.org/10.1016/S0007-8506(07)63240-5).
- [7] The 3D Printing ETF (BATS:PRNT) Has Big Potential | ETF Daily News, (n.d.). <https://etfdailynews.com/2016/09/14/a-brand-new-3d-printing-etf-with-big-investment-potential/> (accessed May 4, 2017).
- [8] J.C. Fox, S.P. Moylan, B.M. Lane, Effect of Process Parameters on the Surface Roughness of Overhanging Structures in Laser Powder Bed Fusion Additive Manufacturing, *Procedia CIRP.* 45 (2016) 131–134. <https://doi.org/10.1016/j.procir.2016.02.347>.
- [9] J.W. Murray, P.K. Kinnell, A.H. Cannon, B. Bailey, A.T. Clare, Surface finishing of intricate metal mould structures by large-area electron beam irradiation, *Precis. Eng.* 37 (2013) 443–450. <https://doi.org/10.1016/j.precisioneng.2012.11.007>.
- [10] E. Yasa, J.P. Kruth, J. Deckers, Manufacturing by combining Selective Laser Melting and Selective Laser Erosion/laser re-melting, *CIRP Ann. - Manuf. Technol.* 60 (2011) 263–266. <https://doi.org/10.1016/j.cirp.2011.03.063>.
- [11] B. Berman, 3-D printing: The new industrial revolution, *Bus. Horiz.* 55 (2012) 155–162. <https://doi.org/10.1016/j.bushor.2011.11.003>.
- [12] O.A. Mohamed, S.H. Masood, J.L. Bhowmik, Optimization of fused deposition modeling process parameters: a review of current research and future prospects, *Adv. Manuf.* 3 (2015) 42–53. <https://doi.org/10.1007/s40436-014-0097-7>.
- [13] S. Jasveer, X. Jianbin, Comparison of Different Types of 3D Printing Technologies, *Int. J. Sci. Res. Publ.* 8 (2018). <https://doi.org/10.29322/IJSRP.8.4.2018.p7602>.

- [14] R. Mutlu, G. Alici, M. in het Panhuis, G.M. Spinks, 3D Printed Flexure Hinges for Soft Monolithic Prosthetic Fingers, *Soft Robot.* 3 (2016) 120–133. <https://doi.org/10.1089/soro.2016.0026>.
- [15] H.K. Yap, H.Y. Ng, C.-H. Yeow, High-Force Soft Printable Pneumatics for Soft Robotic Applications, *Soft Robot.* 3 (2016) 144–158. <https://doi.org/10.1089/soro.2016.0030>.
- [16] R.D. Sochol, E. Sweet, C.C. Glick, S.-Y.Y. Wu, C. Yang, M. Restaino, L. Lin, 3D printed microfluidics and microelectronics, Elsevier B.V., 2018. <https://doi.org/10.1016/j.mee.2017.12.010>.
- [17] T.J. Wallin, J. Pikul, R.F. Shepherd, 3D printing of soft robotic systems, Nature Publishing Group, 2018. <https://doi.org/10.1038/s41578-018-0002-2>.
- [18] R.I. Haque, O. Chandran, S. Lani, D. Briand, Self-powered triboelectric touch sensor made of 3D printed materials, *Nano Energy.* 52 (2018) 54–62. <https://doi.org/10.1016/J.NANOEN.2018.07.038>.
- [19] J.F. Destino, N.A. Dudukovic, M.A. Johnson, D.T. Nguyen, T.D. Yee, G.C. Egan, A.M. Sawvel, W.A. Steele, T.F. Baumann, E.B. Duoss, T. Suratwala, R. Dylla-Spears, 3D Printed Optical Quality Silica and Silica-Titania Glasses from Sol-Gel Feedstocks, *Adv. Mater. Technol.* 3 (2018) 1700323. <https://doi.org/10.1002/admt.201700323>.
- [20] G. Siqueira, D. Kokkinis, R. Libanori, M.K. Hausmann, A.S. Gladman, A. Neels, P. Tingaut, T. Zimmermann, J.A. Lewis, A.R. Studart, Cellulose Nanocrystal Inks for 3D Printing of Textured Cellular Architectures, *Adv. Funct. Mater.* 27 (2017). <https://doi.org/10.1002/adfm.201604619>.
- [21] L.E. Murr, E. Martinez, K.N. Amato, S.M. Gaytan, J. Hernandez, D.A. Ramirez, P.W. Shindo, F. Medina, R.B. Wicker, Fabrication of metal and alloy components by additive manufacturing: Examples of 3D materials science, *J. Mater. Res. Technol.* 1 (2012) 42–54. [https://doi.org/10.1016/S2238-7854\(12\)70009-1](https://doi.org/10.1016/S2238-7854(12)70009-1).
- [22] Z. Fan, H. Feng, Study on selective laser melting and heat treatment of Ti-6Al-4V alloy, *Results Phys.* 10 (2018) 660–664. <https://doi.org/10.1016/j.rinp.2018.07.008>.
- [23] C. Ledford, C. Rock, P. Carriere, P. Frigola, D. Gamzina, T. Horn, Characteristics and Processing of Hydrogen-Treated Copper Powders for EB-PBF Additive Manufacturing, *Appl. Sci.* 9 (2019) 3993. <https://doi.org/10.3390/app9193993>.
- [24] GE prepares Boeing 777X for takeoff with 3D printed turbine blades - 3D Printing Industry, (n.d.). <https://3dprintingindustry.com/news/ge-prepares-boeing-777x-for-takeoff-with-3d-printed-fan-blades-146566/> (accessed October 22, 2019).
- [25] L.E. Murr, S.M. Gaytan, E. Martinez, F. Medina, R.B. Wicker, Next Generation Orthopaedic Implants by Additive Manufacturing Using Electron Beam Melting, *Int. J. Biomater.* 2012 (2012) 14. <https://doi.org/10.1155/2012/245727>.
- [26] Z. Li, C. Liu, B. Wang, C. Wang, Z. Wang, F. Yang, C. Gao, H. Liu, Y. Qin, J. Wang, Heat treatment effect on the mechanical properties, roughness and bone ingrowth capacity of 3D printing porous titanium alloy, *RSC Adv.* 8 (2018) 12471–12483.

<https://doi.org/10.1039/c7ra13313h>.

- [27] O.L.A. Harrysson, D.J. Marcellin-Little, T.J. Horn, Applications of Metal Additive Manufacturing in Veterinary Orthopedic Surgery, *JOM*. 67 (2015) 647–654. <https://doi.org/10.1007/s11837-015-1295-x>.
- [28] D. Gamzina, M. Kozina, A. Mehta, E.A. Nanni, S. Tantawi, P.B. Welander, T. Horn, C. Ledford, Copper Reconsidered: Material Innovations to Transform Vacuum Electronics, in: 2019 Int. Vac. Electron. Conf. IVEC 2019, Institute of Electrical and Electronics Engineers Inc., 2019. <https://doi.org/10.1109/IVEC.2019.8744750>.
- [29] T. Horn, I. Karakurt, C. Ledford, M. Gonzalez, D. Gamzina, N.C. Luhmann, L. Lin, Additively manufactured WR-10 copper waveguide, in: 2018 IEEE Int. Vac. Electron. Conf., IEEE, 2018: pp. 409–410. <https://doi.org/10.1109/IVEC.2018.8391526>.
- [30] I. Karakurt, K.Y. Ho, C. Ledford, D. Gamzina, T. Horn, N.C. Luhmann, L. Lin, Development of a magnetically driven abrasive polishing process for additively manufactured copper structures, in: *Procedia Manuf.*, Elsevier B.V., 2018: pp. 798–805. <https://doi.org/10.1016/j.promfg.2018.07.097>.
- [31] R.D. Sochol, E. Sweet, C.C. Glick, S. Venkatesh, A. Avetisyan, K.F. Ekman, A. Raulinaitis, A. Tsai, A. Wienkers, K. Korner, K. Hanson, A. Long, B.J. Hightower, G. Slatton, D.C. Burnett, T.L. Massey, K. Iwai, L.P. Lee, K.S.J. Pister, L. Lin, 3D printed microfluidic circuitry via multijet-based additive manufacturing, *Lab Chip*. 16 (2016) 668–678. <https://doi.org/10.1039/C5LC01389E>.
- [32] S. Pala, L. Lin, Fully Transparent Piezoelectric Ultrasonic Transducer with 3D Printed Substrate, in: Institute of Electrical and Electronics Engineers (IEEE), 2019: pp. 234–237. <https://doi.org/10.1109/transducers.2019.8808403>.
- [33] D. Foresti, K.T. Kroll, R. Amisshah, F. Sillani, K.A. Homan, D. Poulikakos, J.A. Lewis, Acoustophoretic printing, *Sci. Adv.* 4 (2018). <https://doi.org/10.1126/sciadv.aat1659>.
- [34] D. Song, F. Zare Bidoky, W.J. Hyun, S.B. Walker, J.A. Lewis, C.D. Frisbie, All-Printed, Self-Aligned Carbon Nanotube Thin-Film Transistors on Imprinted Plastic Substrates, *ACS Appl. Mater. Interfaces*. 10 (2018) 15926–15932. <https://doi.org/10.1021/acsami.8b01581>.
- [35] S.H. Park, D.Y. Yang, K.S. Lee, Two-photon stereolithography for realizing ultraprecise three-dimensional nano/microdevices, *Laser Photonics Rev.* 3 (2009) 1–11. <https://doi.org/10.1002/lpor.200810027>.
- [36] T. Zandrini, N. Liaros, L.J. Jiang, Y.F. Lu, J.T. Fourkas, R. Osellame, T. Baldacchini, Effect of the resin viscosity on the writing properties of two-photon polymerization, *Opt. Mater. Express*. 9 (2019) 2601. <https://doi.org/10.1364/ome.9.002601>.
- [37] D.K. Patel, A.H. Sakhaei, M. Layani, B. Zhang, Q. Ge, S. Magdassi, Highly Stretchable and UV Curable Elastomers for Digital Light Processing Based 3D Printing, *Adv. Mater.* 29 (2017) 1606000. <https://doi.org/10.1002/adma.201606000>.
- [38] E. Fantino, A. Chiappone, I. Roppolo, D. Manfredi, R. Bongiovanni, C.F. Pirri, F.

- Calignano, 3D Printing of Conductive Complex Structures with In Situ Generation of Silver Nanoparticles, *Adv. Mater.* 28 (2016) 3712–3717.
<https://doi.org/10.1002/adma.201505109>.
- [39] Q. Ge, A.H. Sakhaei, H. Lee, C.K. Dunn, N.X. Fang, M.L. Dunn, Multimaterial 4D Printing with Tailorable Shape Memory Polymers, *Sci. Rep.* 6 (2016).
<https://doi.org/10.1038/srep31110>.
- [40] M. Zarek, M. Layani, I. Cooperstein, E. Sachyani, D. Cohn, S. Magdassi, 3D Printing of Shape Memory Polymers for Flexible Electronic Devices, *Adv. Mater.* 28 (2016) 4449–4454. <https://doi.org/10.1002/adma.201503132>.
- [41] J.R. Tumbleston, D. Shirvanyants, N. Ermoshkin, R. Januszewicz, A.R. Johnson, D. Kelly, K. Chen, R. Pinschmidt, J.P. Rolland, A. Ermoshkin, E.T. Samulski, J.M. DeSimone, Continuous liquid interface production of 3D objects, *Science* (80-.). 347 (2015) 1349–1351. <https://doi.org/10.1126/science.aaa3304>.
- [42] P.N. Bernal, P. Delrot, D. Loterie, Y. Li, J. Malda, C. Moser, R. Levato, Volumetric Bioprinting of Complex Living-Tissue Constructs within Seconds, *Adv. Mater.* 31 (2019) 1904209. <https://doi.org/10.1002/adma.201904209>.
- [43] M. Shusteff, A.E.M. Browar, B.E. Kelly, J. Henriksson, T.H. Weisgraber, R.M. Panas, N.X. Fang, C.M. Spadaccini, One-step volumetric additive manufacturing of complex polymer structures, *Sci. Adv.* 3 (2017). <https://doi.org/10.1126/sciadv.aao5496>.
- [44] B.E. Kelly, I. Bhattacharya, H. Heidari, M. Shusteff, C.M. Spadaccini, H.K. Taylor, Volumetric additive manufacturing via tomographic reconstruction, *Science* (80-.). 363 (2019) 1075–1079. <https://doi.org/10.1126/science.aau7114>.
- [45] T.M. Valentin, S.E. Leggett, P.-Y. Chen, J.K. Sodhi, L.H. Stephens, H.D. McClintock, Y. Sim, I.Y. Wong, Stereolithographic Printing of Ionically-Crosslinked Alginate Hydrogels for Degradable Biomaterials and Microfluidics, 2017.
<http://www.rsc.org/suppdata/c7/lc/c7lc00694b/c7lc00694b1.pdf> (accessed August 1, 2018).
- [46] P.R. Martinez, A. Goyanes, A.W. Basit, S. Gaisford, Fabrication of drug-loaded hydrogels with stereolithographic 3D printing, *Int. J. Pharm.* 532 (2017) 313–317.
<https://doi.org/10.1016/J.IJPHARM.2017.09.003>.
- [47] S.A. Khaled, M.R. Alexander, D.J. Irvine, R.D. Wildman, M.J. Wallace, S. Sharpe, J. Yoo, C.J. Roberts, Extrusion 3D Printing of Paracetamol Tablets from a Single Formulation with Tunable Release Profiles Through Control of Tablet Geometry, *AAPS PharmSciTech.* (2018) 1–11. <https://doi.org/10.1208/s12249-018-1107-z>.
- [48] A. Melocchi, F. Parietti, A. Maroni, A. Foppoli, A. Gazzaniga, L. Zema, Hot-melt extruded filaments based on pharmaceutical grade polymers for 3D printing by fused deposition modeling, *Int. J. Pharm.* 509 (2016) 255–263.
<https://doi.org/10.1016/j.ijpharm.2016.05.036>.
- [49] P. Phamduy, M.A. Vazquez, C. Kim, V. Mwaffo, A. Rizzo, M. Porfiri, Design and characterization of a miniature free-swimming robotic fish based on multi-material 3D

- printing, *Int. J. Intell. Robot. Appl.* 1 (2017) 209–223. <https://doi.org/10.1007/s41315-017-0012-z>.
- [50] P.N. Bernal, P. Delrot, D. Loterie, Y. Li, J. Malda, C. Moser, R. Levato, Volumetric Bioprinting of Complex Living-Tissue Constructs within Seconds, *Adv. Mater.* (2019) 1904209. <https://doi.org/10.1002/adma.201904209>.
- [51] A. Sydney Gladman, E.A. Matsumoto, R.G. Nuzzo, L. Mahadevan, J.A. Lewis, Biomimetic 4D printing, *Nat. Mater.* 15 (2016) 413–418. <https://doi.org/10.1038/nmat4544>.
- [52] B. Grigoryan, S.J. Paulsen, D.C. Corbett, D.W. Sazer, C.L. Fortin, A.J. Zaita, P.T. Greenfield, N.J. Calafat, J.P. Gounley, A.H. Ta, F. Johansson, A. Randles, J.E. Rosenkrantz, J.D. Louis-Rosenberg, P.A. Galie, K.R. Stevens, J.S. Miller, Multivascular networks and functional intravascular topologies within biocompatible hydrogels, *Science* (80-.). 364 (2019) 458–464. <https://doi.org/10.1126/science.aav9750>.
- [53] T.J. Wallin, J.H. Pikul, S. Bodkhe, B.N. Peele, B.C. Mac Murray, D. Therriault, B.W. McEnerney, R.P. Dillon, E.P. Giannelis, R.F. Shepherd, Click chemistry stereolithography for soft robots that self-heal, *J. Mater. Chem. B.* 5 (2017) 6249–6255. <https://doi.org/10.1039/c7tb01605k>.
- [54] A. Sydney Gladman, E.A. Matsumoto, R.G. Nuzzo, L. Mahadevan, J.A. Lewis, Biomimetic 4D printing, *Nat. Mater.* 15 (2016) 413–418. <https://doi.org/10.1038/nmat4544>.
- [55] H. Yuk, S. Lin, C. Ma, M. Takaffoli, N.X. Fang, X. Zhao, Hydraulic hydrogel actuators and robots optically and sonically camouflaged in water, *Nat. Commun.* 8 (2017). <https://doi.org/10.1038/ncomms14230>.
- [56] I. Karakurt, J. Zhong, L. Lin, 3D Printed Flexible Triboelectric Energy Harvesters via Conformal Coating of Parylene AF4, in: 2019 IEEE 32nd Int. Conf. Micro Electro Mech. Syst., IEEE, 2019: pp. 954–957. <https://doi.org/10.1109/MEMSYS.2019.8870748>.
- [57] E.C.E.C. Sweet, J.C.-L.J.C.L. Chen, I. Karakurt, A.T.A.T. Long, L. Lin, 3D printed three-flow microfluidic concentration gradient generator for clinical E. Coli-antibiotic drug screening, in: Proc. IEEE Int. Conf. Micro Electro Mech. Syst., IEEE, 2017: pp. 205–208. <https://doi.org/10.1109/MEMSYS.2017.7863376>.
- [58] R.B.N. Scharff, E.L. Doubrovski, W.A. Poelman, P.P. Jonker, C.C.L. Wang, J.M.P. Geraedts, Towards behavior design of a 3D-printed soft robotic hand, *Biosyst. Biorobotics.* 17 (2017) 23–29. https://doi.org/10.1007/978-3-319-46460-2_4.
- [59] M. Wehner, R.L. Truby, D.J. Fitzgerald, B. Mosadegh, G.M. Whitesides, J.A. Lewis, R.J. Wood, An integrated design and fabrication strategy for entirely soft, autonomous robots, *Nature.* 536 (2016) 451–455. <https://doi.org/10.1038/nature19100>.
- [60] N.W. Bartlett, M.T. Tolley, J.T.B. Overvelde, J.C. Weaver, B. Mosadegh, K. Bertoldi, G.M. Whitesides, R.J. Wood, A 3D-printed, functionally graded soft robot powered by combustion, *Science* (80-.). 349 (2015) 161–165. <https://doi.org/10.1126/science.aab0129>.

- [61] M. Holmberg, D. Dancila, A. Rydberg, B. Hjörvarsson, U. Jansson, J.J. Marattukalam, N. Johansson, J. Andersson, On Surface Losses in Direct Metal Laser Sintering Printed Millimeter and Submillimeter Waveguides, *J. Infrared, Millimeter, Terahertz Waves*. 39 (2018) 535–545. <https://doi.org/10.1007/s10762-018-0470-x>.
- [62] M. Anderson, New metals shine in 3D printers: With novel materials, 3D printing can build more products - [News], *IEEE Spectr.* 56 (2019) 9–10. <https://doi.org/10.1109/mspec.2019.8678423>.
- [63] Ford 3D-printed the manifold for Ken Block’s 900-hp F-150 “Hoonitruck” - Roadshow, (n.d.). <https://www.cnet.com/roadshow/news/ford-3d-printed-manifold-ken-block-hoonitruck/> (accessed October 22, 2019).
- [64] M. Malinauskas, S. Sakirzanovas, V. Padolskyte, D. Gailevicius, V. Mizeikis, K. Staliunas, S. Juodkazis, L. Jonusauskas, L. Mikoliunaite, T. Katkus, R. Gadonas, 3D opto-structuring of ceramics at nanoscale, in: *SPIE-Intl Soc Optical Eng*, 2018: p. 28. <https://doi.org/10.1117/12.2306883>.
- [65] G. Liu, Y. Zhao, G. Wu, J. Lu, Origami and 4D printing of elastomer-derived ceramic structures, *Sci. Adv.* 4 (2018). <https://doi.org/10.1126/sciadv.aat0641>.
- [66] Z. Chen, D. Zhang, E. Peng, J. Ding, 3D-printed ceramic structures with in situ grown whiskers for effective oil/water separation, *Chem. Eng. J.* 373 (2019) 1223–1232. <https://doi.org/10.1016/j.cej.2019.05.150>.
- [67] H. Cui, R. Hensleigh, D. Yao, D. Maurya, P. Kumar, M.G. Kang, S. Priya, X. (Rayne) Zheng, Three-dimensional printing of piezoelectric materials with designed anisotropy and directional response, *Nat. Mater.* 18 (2019) 234–241. <https://doi.org/10.1038/s41563-018-0268-1>.
- [68] Z.C. Eckel, C. Zhou, J.H. Martin, A.J. Jacobsen, W.B. Carter, T.A. Schaedler, Additive manufacturing of polymer-derived ceramics, *Science* (80-.). 351 (2016) 58–62. <https://doi.org/10.1126/science.aad2688>.
- [69] G. Weisgrab, A. Ovsianikov, P.F. Costa, Functional 3D Printing for Microfluidic Chips, *Adv. Mater. Technol.* 4 (2019) 1900275. <https://doi.org/10.1002/admt.201900275>.
- [70] J. Parrish, K. Lim, B. Zhang, M. Radisic, T.B.F. Woodfield, New Frontiers for Biofabrication and Bioreactor Design in Microphysiological System Development, *Trends Biotechnol.* (2019). <https://doi.org/10.1016/j.tibtech.2019.04.009>.
- [71] R.L. Truby, R.K. Katzschmann, J.A. Lewis, D. Rus, Soft Robotic Fingers with Embedded Ionogel Sensors and Discrete Actuation Modes for Somatosensitive Manipulation, in: *2019 2nd IEEE Int. Conf. Soft Robot., IEEE*, 2019: pp. 322–329. <https://doi.org/10.1109/ROBOSOFT.2019.8722722>.
- [72] X. Gong, T. Anderson, K. Chou, Review on powder - based electron beam additive manufacturing technology, *Manuf. Rev.* 1 (2014) 1–9. <https://doi.org/10.1051/mfreview/2014001>.
- [73] M. Seifi, A. Salem, J. Beuth, O. Harrysson, J.J. Lewandowski, Overview of Materials

- Qualification Needs for Metal Additive Manufacturing, *JOM*. 68 (2016) 747–764.
<https://doi.org/10.1007/s11837-015-1810-0>.
- [74] Additive Manufacturing (3D-printing) in the energy sector | Spare parts for gas and steam turbines and other rotating equipment | Siemens, (n.d.).
<https://new.siemens.com/global/en/products/energy/services/maintenance/parts/additive-manufacturing.html> (accessed October 29, 2019).
- [75] G. Liu, Y. Zhao, G. Wu, J. Lu, Origami and 4D printing of elastomer-derived ceramic structures, *Sci. Adv.* 4 (2018) eaat0641. <https://doi.org/10.1126/sciadv.aat0641>.
- [76] J.T. Muth, D.M. Vogt, R.L. Truby, Y. Mengüç, D.B. Kolesky, R.J. Wood, J.A. Lewis, Embedded 3D printing of strain sensors within highly stretchable elastomers, *Adv. Mater.* 26 (2014) 6307–6312. <https://doi.org/10.1002/adma.201400334>.
- [77] A. Frutiger, J.T. Muth, D.M. Vogt, Y. Mengüç, A. Campo, A.D. Valentine, C.J. Walsh, J.A. Lewis, Capacitive soft strain sensors via multicore-shell fiber printing, *Adv. Mater.* 27 (2015) 2440–2446. <https://doi.org/10.1002/adma.201500072>.
- [78] E. García-T̄On, S. Barg, J. Franco, R. Bell, S. Eslava, E. D’Elia, R.C. Maher, F. Guitian, E. Saiz, Printing in three dimensions with Graphene, *Adv. Mater.* 27 (2015) 1688–1693. <https://doi.org/10.1002/adma.201405046>.
- [79] S.Y. Wu, C. Yang, W. Hsu, L. Lin, 3D-printed microelectronics for integrated circuitry and passive wireless sensors, *Microsystems Nanoeng.* 1 (2015).
<https://doi.org/10.1038/micronano.2015.13>.
- [80] J.J. Adams, E.B. Duoss, T.F. Malkowski, M.J. Motala, B.Y. Ahn, R.G. Nuzzo, J.T. Bernhard, J.A. Lewis, Conformal printing of electrically small antennas on three-dimensional surfaces, *Adv. Mater.* 23 (2011) 1335–1340.
<https://doi.org/10.1002/adma.201003734>.
- [81] P.-C. Yeh, J. Chen, I. Karakurt, L. Lin, 3D Printed Bio-Sensing Chip for the Determination of Bacteria Antibiotic-Resistant Profile, in: 2019 20th Int. Conf. Solid-State Sensors, Actuators Microsystems Eurosensors XXXIII (TRANSDUCERS EUROSENSORS XXXIII), IEEE, 2019: pp. 126–129.
<https://doi.org/10.1109/TRANSDUCERS.2019.8808229>.
- [82] N.N. Kumbhar, A. V. Mulay, Post Processing Methods used to Improve Surface Finish of Products which are Manufactured by Additive Manufacturing Technologies: A Review, *J. Inst. Eng. Ser. C*. 99 (2018) 481–487. <https://doi.org/10.1007/s40032-016-0340-z>.
- [83] Z. Yang, G. Wu, S. Wang, M. Xu, X. Feng, Dynamic postpolymerization of 3D-printed photopolymer nanocomposites: Effect of cellulose nanocrystal and postcure temperature, *J. Polym. Sci. Part B Polym. Phys.* 56 (2018) 935–946.
<https://doi.org/10.1002/polb.24610>.
- [84] M. Malinauskas, S. Sakirzanovas, V. Padolskyte, D. Gailevicius, V. Mizeikis, K. Staliunas, S. Juodkazis, L. Jonusauskas, L. Mikoliunaite, T. Katkus, R. Gadonas, 3D opto-structuring of ceramics at nanoscale, in: *SPIE-Intl Soc Optical Eng*, 2018: p. 28.
<https://doi.org/10.1117/12.2306883>.

- [85] Y. Mao, K. Yu, M.S. Isakov, J. Wu, M.L. Dunn, H. Jerry Qi, Sequential Self-Folding Structures by 3D Printed Digital Shape Memory Polymers, *Sci. Rep.* 5 (2015). <https://doi.org/10.1038/srep13616>.
- [86] J. Elwood, L. Lin, A 3D Printed Ethanol Sensor Using Conformally-Coated Conductive Polymer Electrodes, in: Institute of Electrical and Electronics Engineers (IEEE), 2019: pp. 1230–1233. <https://doi.org/10.1109/transducers.2019.8808789>.
- [87] Z.L. Wang, Nanogenerators, self-powered systems, blue energy, piezotronics and piezophotonics – A recall on the original thoughts for coining these fields, *Nano Energy*. 54 (2018) 477–483. <https://doi.org/10.1016/j.nanoen.2018.09.068>.
- [88] Y. Jie, J. Ma, Y. Chen, X. Cao, N. Wang, Z.L. Wang, Efficient Delivery of Power Generated by a Rotating Triboelectric Nanogenerator by Conjunction of Wired and Wireless Transmissions Using Maxwell’s Displacement Currents, *Adv. Energy Mater.* 8 (2018). <https://doi.org/10.1002/aenm.201802084>.
- [89] Y. Song, H. Wang, X. Cheng, G. Li, X. Chen, H. Chen, L. Miao, X. Zhang, H. Zhang, High-efficiency self-charging smart bracelet for portable electronics, *Nano Energy*. 55 (2019) 29–36. <https://doi.org/10.1016/j.nanoen.2018.10.045>.
- [90] H. Song, I. Karakurt, M. Wei, N. Liu, Y. Chu, J. Zhong, L. Lin, Lead iodide nanosheets for piezoelectric energy conversion and strain sensing, *Nano Energy*. 49 (2018). <https://doi.org/10.1016/j.nanoen.2018.04.029>.
- [91] X. Cheng, W. Tang, Y. Song, H. Chen, H. Zhang, Z.L. Wang, Power management and effective energy storage of pulsed output from triboelectric nanogenerator, *Nano Energy*. 61 (2019) 517–532. <https://doi.org/10.1016/j.nanoen.2019.04.096>.
- [92] X. Cao, Y. Jie, N. Wang, Z.L. Wang, Triboelectric Nanogenerators Driven Self-Powered Electrochemical Processes for Energy and Environmental Science, *Adv. Energy Mater.* 6 (2016). <https://doi.org/10.1002/aenm.201600665>.
- [93] W. Tang, Y. Han, C.B. Han, C.Z. Gao, X. Cao, Z.L. Wang, Self-powered water splitting using flowing kinetic energy, *Adv. Mater.* 27 (2015) 272–276. <https://doi.org/10.1002/adma.201404071>.
- [94] Y. Jie, H. Zhu, X. Cao, Y. Zhang, N. Wang, L. Zhang, Z.L. Wang, One-Piece Triboelectric Nanosensor for Self-Triggered Alarm System and Latent Fingerprint Detection, *ACS Nano*. 10 (2016) 10366–10372. <https://doi.org/10.1021/acsnano.6b06100>.
- [95] J. Wu, Z. Wu, X. Lu, S. Han, B.R. Yang, X. Gui, K. Tao, J. Miao, C. Liu, Ultrastretchable and Stable Strain Sensors Based on Antifreezing and Self-Healing Ionic Organohydrogels for Human Motion Monitoring, *ACS Appl. Mater. Interfaces*. 11 (2019) 9405–9414. <https://doi.org/10.1021/acsaami.8b20267>.
- [96] S. Wang, M. Bi, Z. Cao, X. Ye, Linear freestanding electret generator for harvesting swinging motion energy: Optimization and experiment, *Nano Energy*. 65 (2019). <https://doi.org/10.1016/j.nanoen.2019.104013>.
- [97] Y. Zhang, T. Wang, A. Luo, Y. Hu, X. Li, F. Wang, Micro electrostatic energy harvester

- with both broad bandwidth and high normalized power density, *Appl. Energy*. 212 (2018) 362–371. <https://doi.org/10.1016/j.apenergy.2017.12.053>.
- [98] T. Zhou, L. Zhang, F. Xue, W. Tang, C. Zhang, Z.L. Wang, Multilayered electret films based triboelectric nanogenerator, *Nano Res.* 9 (2016) 1442–1451. <https://doi.org/10.1007/s12274-016-1040-y>.
- [99] P. Wang, L. Pan, J. Wang, M. Xu, G. Dai, H. Zou, K. Dong, Z.L. Wang, An Ultra-Low-Friction Triboelectric-Electromagnetic Hybrid Nanogenerator for Rotation Energy Harvesting and Self-Powered Wind Speed Sensor, *ACS Nano*. 12 (2018) 9433–9440. <https://doi.org/10.1021/acsnano.8b04654>.
- [100] X. Shan, H. Li, Y. Yang, J. Feng, Y. Wang, T. Xie, Enhancing the performance of an underwater piezoelectric energy harvester based on flow-induced vibration, *Energy*. 172 (2019) 134–140. <https://doi.org/10.1016/j.energy.2019.01.120>.
- [101] J. Wang, S. Zhou, Z. Zhang, D. Yurchenko, High-performance piezoelectric wind energy harvester with Y-shaped attachments, *Energy Convers. Manag.* 181 (2019) 645–652. <https://doi.org/10.1016/j.enconman.2018.12.034>.
- [102] X. Zhang, P. Pondrom, G.M. Sessler, X. Ma, Ferroelectret nanogenerator with large transverse piezoelectric activity, *Nano Energy*. 50 (2018) 52–61. <https://doi.org/10.1016/j.nanoen.2018.05.016>.
- [103] L.C. Zhao, H.X. Zou, G. Yan, F.R. Liu, T. Tan, W.M. Zhang, Z.K. Peng, G. Meng, A water-proof magnetically coupled piezoelectric-electromagnetic hybrid wind energy harvester, *Appl. Energy*. 239 (2019) 735–746. <https://doi.org/10.1016/j.apenergy.2019.02.006>.
- [104] H. Zhang, Y. Lu, A. Ghaffarinejad, P. Basset, Progressive contact-separate triboelectric nanogenerator based on conductive polyurethane foam regulated with a Bennet doubler conditioning circuit, *Nano Energy*. 51 (2018) 10–18. <https://doi.org/10.1016/j.nanoen.2018.06.038>.
- [105] W. Li, N. Wu, J. Zhong, Q. Zhong, S. Zhao, B. Wang, X. Cheng, S. Li, K. Liu, B. Hu, J. Zhou, Theoretical Study of Cellular Piezoelectret Generators, *Adv. Funct. Mater.* 26 (2016) 1964–1974. <https://doi.org/10.1002/adfm.201503704>.
- [106] X. Cao, M. Zhang, J. Huang, T. Jiang, J. Zou, N. Wang, Z.L. Wang, Inductor-Free Wireless Energy Delivery via Maxwell’s Displacement Current from an Electrodeless Triboelectric Nanogenerator, *Adv. Mater.* 30 (2018). <https://doi.org/10.1002/adma.201704077>.
- [107] S. Pan, Z. Zhang, Fundamental theories and basic principles of triboelectric effect: A review, *Friction*. 7 (2019) 2–17. <https://doi.org/10.1007/s40544-018-0217-7>.
- [108] G. Zhu, B. Peng, J. Chen, Q. Jing, Z.L. Wang, Triboelectric nanogenerators as a new energy technology: From fundamentals, devices, to applications, (2014). <https://doi.org/10.1016/j.nanoen.2014.11.050>.
- [109] N. Wu, X. Cheng, Q. Zhong, J. Zhong, W. Li, B. Wang, B. Hu, J. Zhou, Cellular

- Polypropylene Piezoelectret for Human Body Energy Harvesting and Health Monitoring, *Adv. Funct. Mater.* 25 (2015) 4788–4794. <https://doi.org/10.1002/adfm.201501695>.
- [110] J. Zhong, Q. Zhong, X. Zang, N. Wu, W. Li, Y. Chu, L. Lin, Flexible PET/EVA-based piezoelectret generator for energy harvesting in harsh environments, *Nano Energy*. 37 (2017) 268–274. <https://doi.org/10.1016/j.nanoen.2017.05.034>.
- [111] G. Zhu, P. Bai, J. Chen, Z. Lin Wang, Power-generating shoe insole based on triboelectric nanogenerators for self-powered consumer electronics, *Nano Energy*. 2 (2013) 688–692. <https://doi.org/10.1016/j.nanoen.2013.08.002>.
- [112] W. Yang, J. Chen, G. Zhu, J. Yang, P. Bai, Y. Su, Q. Jing, X. Cao, Z. Lin Wang, Harvesting Energy from the Natural Vibration of Human Walking, 17 (2020) 23. <https://doi.org/10.1021/nn405175z>.
- [113] J. Zhong, Y. Zhang, Q. Zhong, Q. Hu, B. Hu, Z. Lin Wang, J. Zhou, J. Zhong, Y. Zhang, Q. Zhong, Fiber-Based Generator for Wearable Electronics and Mobile Medication, 17 (2020) 35. <https://doi.org/10.1021/nn501732z>.
- [114] W. Yang, J. Chen, Q. Jing, J. Yang, X. Wen, Y. Su, G. Zhu, P. Bai, Z.L. Wang, 3D stack integrated triboelectric nanogenerator for harvesting vibration energy, *Adv. Funct. Mater.* 24 (2014) 4090–4096. <https://doi.org/10.1002/adfm.201304211>.
- [115] Z.L. Wang, Triboelectric nanogenerators as new energy technology and self-powered sensors - Principles, problems and perspectives, *Faraday Discuss.* 176 (2014) 447–458. <https://doi.org/10.1039/c4fd00159a>.
- [116] Y. Jie, Q. Jiang, Y. Zhang, N. Wang, X. Cao, A structural bionic design: From electric organs to systematic triboelectric generators, *Nano Energy*. 27 (2016) 554–560. <https://doi.org/10.1016/j.nanoen.2016.07.028>.
- [117] X. Xia, J. Chen, H. Guo, G. Liu, D. Wei, Y. Xi, X. Wang, C. Hu, Embedding variable micro-capacitors in polydimethylsiloxane for enhancing output power of triboelectric nanogenerator, *Nano Res.* 10 (2017) 320–330. <https://doi.org/10.1007/s12274-016-1294-4>.
- [118] Y. Feng, Y. Zheng, Z.U. Rahman, D. Wang, F. Zhou, W. Liu, Paper-based triboelectric nanogenerators and their application in self-powered anticorrosion and antifouling, *J. Mater. Chem. A*. 4 (2016) 18022–18030. <https://doi.org/10.1039/c6ta07288g>.
- [119] H. Guo, J. Chen, Q. Leng, Y. Xi, M. Wang, X. He, C. Hu, Spiral-interdigital-electrode-based multifunctional device: Dual-functional triboelectric generator and dual-functional self-powered sensor, *Nano Energy*. 12 (2015) 626–635. <https://doi.org/10.1016/j.nanoen.2014.09.021>.
- [120] Y. Jie, N. Wang, X. Cao, Y. Xu, T. Li, X. Zhang, Z.L. Wang, Self-Powered Triboelectric Nanosensor with Poly(tetrafluoroethylene) Nanoparticle Arrays for Dopamine Detection, *ACS Nano*. 9 (2015) 8376–8383. <https://doi.org/10.1021/acsnano.5b03052>.
- [121] X.S. Zhang, M. Di Han, R.X. Wang, F.Y. Zhu, Z.H. Li, W. Wang, H.X. Zhang, Frequency-multiplication high-output triboelectric nanogenerator for sustainably powering

- biomedical microsystems, *Nano Lett.* 13 (2013) 1168–1172.
<https://doi.org/10.1021/nl3045684>.
- [122] W. Tang, J. Tian, Q. Zheng, L. Yan, J. Wang, Z. Li, Z.L. Wang, Implantable Self-Powered Low-Level Laser Cure System for Mouse Embryonic Osteoblasts' Proliferation and Differentiation, *ACS Nano.* 9 (2015) 7867–7873.
<https://doi.org/10.1021/acsnano.5b03567>.
- [123] J. Wang, Z. Wen, Y. Zi, P. Zhou, J. Lin, H. Guo, Y. Xu, Z.L. Wang, All-Plastic-Materials Based Self-Charging Power System Composed of Triboelectric Nanogenerators and Supercapacitors, *Adv. Funct. Mater.* 26 (2016) 1070–1076.
<https://doi.org/10.1002/adfm.201504675>.
- [124] L. Gao, D. Hu, M. Qi, J. Gong, H. Zhou, X. Chen, J. Chen, J. Cai, L. Wu, N. Hu, Y. Yang, X. Mu, A double-helix-structured triboelectric nanogenerator enhanced with positive charge traps for self-powered temperature sensing and smart-home control systems, *Nanoscale.* 10 (2018) 19781–19790. <https://doi.org/10.1039/c8nr05957h>.
- [125] L.M. Zhang, C.B. Han, T. Jiang, T. Zhou, X.H. Li, C. Zhang, Z.L. Wang, Multilayer wavy-structured robust triboelectric nanogenerator for harvesting water wave energy, *Nano Energy.* 22 (2016) 87–94. <https://doi.org/10.1016/j.nanoen.2016.01.009>.
- [126] X. Wang, S. Niu, F. Yi, Y. Yin, C. Hao, K. Dai, Y. Zhang, Z. You, Z.L. Wang, Harvesting Ambient Vibration Energy over a Wide Frequency Range for Self-Powered Electronics, *ACS Nano.* 11 (2017) 1728–1735. <https://doi.org/10.1021/acsnano.6b07633>.
- [127] K. Tao, H. Yi, Y. Yang, H. Chang, J. Wu, L. Tang, Z. Yang, N. Wang, L. Hu, Y. Fu, J. Miao, W. Yuan, Origami-inspired electret-based triboelectric generator for biomechanical and ocean wave energy harvesting, *Nano Energy.* 67 (2020) 104197.
<https://doi.org/10.1016/j.nanoen.2019.104197>.
- [128] S.L. Zhang, M. Xu, C. Zhang, Y.C. Wang, H. Zou, X. He, Z. Wang, Z.L. Wang, Rationally designed sea snake structure based triboelectric nanogenerators for effectively and efficiently harvesting ocean wave energy with minimized water screening effect, *Nano Energy.* 48 (2018) 421–429. <https://doi.org/10.1016/j.nanoen.2018.03.062>.
- [129] T. Jiang, Y. Yao, L. Xu, L. Zhang, T. Xiao, Z.L. Wang, Spring-assisted triboelectric nanogenerator for efficiently harvesting water wave energy, *Nano Energy.* 31 (2017) 560–567. <https://doi.org/10.1016/j.nanoen.2016.12.004>.
- [130] J. Wang, L. Pan, H. Guo, B. Zhang, R. Zhang, Z. Wu, C. Wu, L. Yang, R. Liao, Z.L. Wang, Rational Structure Optimized Hybrid Nanogenerator for Highly Efficient Water Wave Energy Harvesting, *Adv. Energy Mater.* 9 (2019).
<https://doi.org/10.1002/aenm.201802892>.
- [131] S. Wang, Y. Xie, S. Niu, L. Lin, C. Liu, Y.S. Zhou, Z.L. Wang, Maximum surface charge density for triboelectric nanogenerators achieved by ionized-air injection: Methodology and theoretical understanding, *Adv. Mater.* 26 (2014) 6720–6728.
<https://doi.org/10.1002/adma.201402491>.
- [132] B. Chen, W. Tang, T. Jiang, L. Zhu, X. Chen, C. He, L. Xu, H. Guo, P. Lin, D. Li, J.

- Shao, Z.L. Wang, Three-dimensional ultraflexible triboelectric nanogenerator made by 3D printing, *Nano Energy*. 45 (2018) 380–389.
<https://doi.org/10.1016/J.NANOEN.2017.12.049>.
- [133] Y. Xie, S. Wang, S. Niu, L. Lin, Q. Jing, J. Yang, Z. Wu, Z.L. Wang, Grating-Structured Freestanding Triboelectric-Layer Nanogenerator for Harvesting Mechanical Energy at 85% Total Conversion Efficiency, *Adv. Mater.* 26 (2014) 6599–6607.
<https://doi.org/10.1002/adma.201402428>.
- [134] H. Qiao, Y. Zhang, Z. Huang, Y. Wang, D. Li, H. Zhou, 3D printing individualized triboelectric nanogenerator with macro-pattern, *Nano Energy*. 50 (2018) 126–132.
<https://doi.org/10.1016/J.NANOEN.2018.04.071>.
- [135] M.-L. Seol, R. Ivaškevičiūtė, M.A. Ciappesoni, F. V. Thompson, D.-I. Moon, S.J. Kim, S.J. Kim, J.-W. Han, M. Meyyappan, All 3D printed energy harvester for autonomous and sustainable resource utilization, *Nano Energy*. 52 (2018) 271–278.
<https://doi.org/10.1016/J.NANOEN.2018.07.061>.
- [136] Carbon3D, CarbonResin EPU 40 SDS, 2016. https://s3.amazonaws.com/carbon-static-assets/downloads/resin_data_sheets/EPU40_TDS.pdf (accessed August 22, 2018).
- [137] Carbon - The World's Leading Digital Manufacturing Platform, (n.d.).
<https://www.carbon3d.com/> (accessed April 26, 2020).
- [138] Y. Suzuki, Recent progress in MEMS electret generator for energy harvesting, *IEEJ Trans. Electr. Electron. Eng.* 6 (2011) 101–111. <https://doi.org/10.1002/tee.20631>.
- [139] Z. Yang, J. Wang, J. Zhang, Parylene-based electret power generators, (2008).
<https://doi.org/10.1088/0960-1317/18/10/104006>.
- [140] F. Belhora, D. Guyomar, M.H. Mazroui, A. Hajjaji, Y. Boughaleb, Thickness effects of electret and polymer for energy harvesting: Case of CYTOP- CTLM and polyurethane, *Eur. Phys. J. Plus.* 130 (2015). <https://doi.org/10.1140/epjp/i2015-15020-x>.
- [141] S. Genter, O. Paul, Influence of various conducting and inorganic dielectric drift barriers on the charge decay in Parylene-C electret layers, *J. Phys. Conf. Ser.* 557 (2014).
<https://doi.org/10.1088/1742-6596/557/1/012102>.
- [142] Y. Chu, J. Zhong, H. Liu, Y. Ma, N. Liu, Y. Song, J. Liang, Z. Shao, Y. Sun, Y. Dong, X. Wang, L. Lin, Human Pulse Diagnosis for Medical Assessments Using a Wearable Piezoelectret Sensing System, *Adv. Funct. Mater.* 28 (2018) 1803413.
<https://doi.org/10.1002/adfm.201803413>.
- [143] Wearable Tech in Healthcare: Smart Medical Devices & Trends in 2020 - Business Insider, (n.d.). <https://www.businessinsider.com/wearable-technology-healthcare-medical-devices> (accessed April 26, 2020).
- [144] Apple Watch Series 5 - Apple, (n.d.). <https://www.apple.com/apple-watch-series-5/> (accessed April 26, 2020).
- [145] Wearable Technology Forecasts 2019-2029: IDTechEx, (n.d.).
<https://www.idtechex.com/en/research-report/wearable-technology-forecasts-2019->

- 2029/680 (accessed April 26, 2020).
- [146] adidas 4D Technology Shoes | adidas US, (n.d.). <https://www.adidas.com/us/4D> (accessed April 26, 2020).
- [147] J. Zhao, Z. You, A Shoe-Embedded Piezoelectric Energy Harvester for Wearable Sensors, *Sensors*. 14 (2014) 12497–12510. <https://doi.org/10.3390/s140712497>.
- [148] A. Almusallam, N. Torah Torah, D. Zhu, J. Tudor, S. Beeby, Screen-Printed Piezoelectric Shoe-Insole Energy Harvester Using an Improved Flexible PZT-Polymer Composites, (2013). <https://doi.org/10.1088/1742-6596/476/1/012108>.
- [149] B. Meng, W. Tang, X. Zhang, M. Han, W. Liu, H. Zhang, Self-powered flexible printed circuit board with integrated triboelectric generator, *Nano Energy*. 2 (2013) 1101–1106. <https://doi.org/10.1016/j.nanoen.2013.08.006>.
- [150] The Best Running Shoes for Men | Reviews by Wirecutter, (n.d.). <https://thewirecutter.com/reviews/best-running-shoes-for-men/> (accessed April 27, 2020).
- [151] Y. Chiu, M.H. Lee, W.-H. Hsu, PDMS-based flexible energy harvester with Parylene electret and copper mesh electrodes Related content Flexible Electret Energy Harvester with Copper Mesh Electrodes, *J. Micromech. Microeng.* 25 (2015) 104007. <https://doi.org/10.1088/0960-1317/25/10/104007>.
- [152] M.R. Ahmad, M.H. Md Khir, J.O. Dennis, al -, S. Genter, O. Paul, Influence of a SiN Drift-Barrier on the Charge Decay in Parylene-C Electret Layers, *J. Phys. Conf. Ser.* OPEN ACCESS. (2013). <https://doi.org/10.1088/1742-6596/476/1/012084>.
- [153] A. Kachroudi, C. Lagomarsini, V.H. Mareau, A. Sylvestre, Annealing for the improvement of the capabilities of parylene C as electret, *J. Appl. Polym. Sci.* 136 (2019) 46908. <https://doi.org/10.1002/app.46908>.
- [154] S. Genter, Parylene-C as the Electret Material for Micro Energy Harvesting, n.d.
- [155] S. Li, Q. Zhong, J. Zhong, X. Cheng, B. Wang, B. Hu, J. Zhou, Cloth-based power shirt for wearable energy harvesting and clothes ornamentation, *ACS Appl. Mater. Interfaces*. 7 (2015) 14912–14916. <https://doi.org/10.1021/acsami.5b03680>.
- [156] G. Yao, L. Xu, X. Cheng, Y. Li, X. Huang, W. Guo, S. Liu, Z.L. Wang, H. Wu, Bioinspired Triboelectric Nanogenerators as Self-Powered Electronic Skin for Robotic Tactile Sensing, *Adv. Funct. Mater.* 30 (2020) 1907312. <https://doi.org/10.1002/adfm.201907312>.
- [157] S. Okamura, History of electron tubes, (1994) 233. https://books.google.co.uk/books/about/History_of_Electron_Tubes.html?id=VHFyngmO95YC&redir_esc=y (accessed April 28, 2020).
- [158] G.L. Pearson, W.H. Brattain, History of Semiconductor Research, *Proc. IRE*. 43 (1955) 1794–1806. <https://doi.org/10.1109/JRPROC.1955.278042>.
- [159] A. Malekabadi, C. Paoloni, UV-LIGA microfabrication process for sub-terahertz waveguides utilizing multiple layered SU-8 photoresist, *J. Micromechanics*

- Microengineering. 26 (2016). <https://doi.org/10.1088/0960-1317/26/9/095010>.
- [160] R.J. Barker, IEEE Nuclear and Plasma Sciences Society., Modern microwave and millimeter-wave power electronics, IEEE Press, 2005.
- [161] J.H. Booske, R.J. Dobbs, C.D. Joye, C.L. Kory, G.R. Neil, G.S. Park, J. Park, R.J. Temkin, Vacuum electronic high power terahertz sources, IEEE Trans. Terahertz Sci. Technol. 1 (2011) 54–75. <https://doi.org/10.1109/TTHZ.2011.2151610>.
- [162] P.H. Siegel, Terahertz technology, IEEE Trans. Microw. Theory Tech. 50 (2002) 910–928. <https://doi.org/10.1109/22.989974>.
- [163] M. Tonouchi, Cutting-edge terahertz technology, Nat. Photonics. 1 (2007) 97–105. <https://doi.org/10.1038/nphoton.2007.3>.
- [164] X. Li, Y. Zheng, C. Hurd, D. Gamzina, C. Paoloni, L. Himes, R. Letizia, N.C. Luhmann, Y. Tang, X. Hao, M. Gonzalez, H. Li, P. Pan, J. Feng, Backward wave oscillator for high power generation at THz frequencies, in: SPIE-Intl Soc Optical Eng, 2017: p. 2. <https://doi.org/10.1117/12.2273256>.
- [165] D. Gamzina, H. Li, L. Himes, R. Barchfeld, B. Popovic, P. Pan, R. Letizia, M. Mineo, J. Feng, C. Paoloni, N.C. Luhmann, Nanoscale surface roughness effects on THz vacuum electron device performance, IEEE Trans. Nanotechnol. 15 (2016) 85–93. <https://doi.org/10.1109/TNANO.2015.2503984>.
- [166] Y.M. Shin, L.R. Barnett, D. Gamzina, N.C. Luhmann, M. Field, R. Borwick, Terahertz vacuum electronic circuits fabricated by UV lithographic molding and deep reactive ion etching, Appl. Phys. Lett. 95 (2009). <https://doi.org/10.1063/1.3259823>.
- [167] Arcam AB - Additive Manufacturing for Implants and Aerospace, EBM, (n.d.). <http://www.arcam.com/> (accessed May 4, 2017).
- [168] M.S. Cheema, G. Venkatesh, A. Dvivedi, A.K. Sharma, Developments in abrasive flow machining: A review on experimental investigations using abrasive flow machining variants and media, Proc. Inst. Mech. Eng. Part B J. Eng. Manuf. 226 (2012) 1951–1962. <https://doi.org/10.1177/0954405412462000>.
- [169] H. Yamaguchi, T. Shinmura, A. Kobayashi, Development of an Internal Magnetic Abrasive Finishing Process for Nonferromagnetic Complex Shaped Tubes., JSME Int. J. Ser. C. 44 (2001) 275–281. <https://doi.org/10.1299/jsmec.44.275>.
- [170] J. Kang, A. George, H. Yamaguchi, High-speed internal finishing of capillary tubes by magnetic abrasive finishing, Procedia CIRP. 1 (2012) 414–418. <https://doi.org/10.1016/j.procir.2012.04.074>.
- [171] H. Yamaguchi, T. Shinmura, Internal finishing process for alumina ceramic components by a magnetic field assisted finishing process, Precis. Eng. 28 (2004) 135–142. <https://doi.org/10.1016/j.precisioneng.2003.07.001>.
- [172] J. Kang, H. Yamaguchi, Internal finishing of capillary tubes by magnetic abrasive finishing using a metastable austenitic stainless steel tool, Proc. Twenty-Fourth Annu. ASPE Meet. (2010) 1–4.

- [173] S. Jha, V.K. Jain, Design and development of the magnetorheological abrasive flow finishing (MRAFF) process, *Int. J. Mach. Tools Manuf.* 44 (2004) 1019–1029. <https://doi.org/10.1016/j.ijmachtools.2004.03.007>.
- [174] B.S. Brar, R.S. Walia, V.P. Singh, Electrochemical-aided abrasive flow machining (ECA²FM) process: a hybrid machining process, *Int. J. Adv. Manuf. Technol.* 79 (2015) 329–342. <https://doi.org/10.1007/s00170-015-6806-y>.
- [175] K.L. Tan, S.-H. Yeo, C.H. Ong, Nontraditional finishing processes for internal surfaces and passages: A review, *Proc. Inst. Mech. Eng. Part B J. Eng. Manuf.* (2016). <https://doi.org/10.1177/0954405415626087>.
- [176] J. Kang, DEVELOPMENT OF HIGH-SPEED INTERNAL FINISHING AND CLEANING OF FLEXIBLE CAPILLARY TUBES BY MAGNETIC ABRASIVE FINISHING, University of Florida, 2012. <https://doi.org/10.1016/j.procir.2012.04.074>.
- [177] B.M. Lane, S.P. Moylan, E.P. Whintont, POST-PROCESS MACHINING OF ADDITIVE MANUFACTURED STAINLESS STEEL, (n.d.). http://ws680.nist.gov/publication/get_pdf.cfm?pub_id=918449 (accessed May 4, 2017).
- [178] G. Pyka, A. Burakowski, G. Kerckhofs, M. Moesen, S. Van Bael, J. Schrooten, M. Wevers, Surface modification of Ti6Al4V open porous structures produced by additive manufacturing, *Adv. Eng. Mater.* 14 (2012) 363–370. <https://doi.org/10.1002/adem.201100344>.
- [179] X. Liu, P.K. Chu, C. Ding, Surface modification of titanium, titanium alloys, and related materials for biomedical applications, *Mater. Sci. Eng. R Reports.* 47 (2004) 49–121. <https://doi.org/10.1016/j.mser.2004.11.001>.
- [180] G.Y. Liu, Z.N. Guo, S.Z. Jiang, N.S. Qu, Y.B. Li, A study of processing Al 6061 with electrochemical magnetic abrasive finishing, *Procedia CIRP.* 14 (2014) 234–238. <https://doi.org/10.1016/j.procir.2014.03.052>.
- [181] P. Jacquet, Electrolytic method for obtaining bright copper surfaces, *Nature.* (1935) 1076. <https://www.nature.com/nature/journal/v135/n3426/pdf/1351076c0.pdf> (accessed May 4, 2017).
- [182] I.A.S. Mansour, G.H. Sedahmed, ELECTROPOLISHING OF HORIZONTAL COPPER CYLINDERS IN UNSTIRRED PHOSPHORIC ACID SOLUTION, 7 (1978) 313–318.
- [183] G. Schütz, Natural convection mass-transfer measurements on spheres and horizontal cylinders by an electrochemical method, *Int. J. Heat Mass Transf.* 6 (1963) 873–879. [https://doi.org/10.1016/0017-9310\(63\)90078-4](https://doi.org/10.1016/0017-9310(63)90078-4).
- [184] A.M. Awad, N.A.A. Ghany, T.M. Dahy, Removal of tarnishing and roughness of copper surface by electropolishing treatment, *Appl. Surf. Sci.* 256 (2010) 4370–4375. <https://doi.org/10.1016/j.apsusc.2010.02.033>.
- [185] D. Brent, T.A. Saunders, F.G. Moreno, P. Tyagi, TAGUCHI DESIGN OF EXPERIMENT FOR THE OPTIMIZATION OF ELECTROCHEMICAL POLISHING OF METAL ADDITIVE MANUFACTURING, in: *ASME 2016 Int. Mech. Eng. Congr. Expo.*, 2017:

pp. 1–6.

- [186] D.R. Gabe, Electropolishing of copper and copper-based alloys in ortho-phosphoric acid, *Corros. Sci.* 12 (1972) 113–120. [https://doi.org/10.1016/S0010-938X\(72\)90826-8](https://doi.org/10.1016/S0010-938X(72)90826-8).
- [187] M. Turner, P.A. Brook, Some observations on the electropolishing of copper, *Electrodepos. Surf. Treat.* 2 (1974) 245–248. [https://doi.org/10.1016/0300-9416\(74\)90038-8](https://doi.org/10.1016/0300-9416(74)90038-8).
- [188] A.A. Taha, H.H. Abdel Rahman, F.M. Abouzeid, Effect of surfactants on the rate of diffusion controlled anodic dissolution of copper in orthophosphoric acid, *Int. J. Electrochem. Sci.* 8 (2013) 6744–6762.
- [189] P. Monk, *Finite Element Methods for Maxwell’s Equations*, in: 2003.
- [190] E. Rabinowicz, *Friction and wear of materials*, 2nd ed., Wiley, New York, 1995.
- [191] W.N. Cottingham, D.A. Greenwood, *Electricity and Magnetism*, Cambridge University Press, 1991. <https://doi.org/10.1017/CBO9781139168106>.
- [192] W.M. Saslow, How Electric Currents Make Magnetic Fields: The Biot– Savart Law and Ampère’s Law, *Electr. Magn. Light.* (2002) 460–504. <https://doi.org/10.1016/b978-012619455-5.50011-5>.
- [193] J. Yang, T.H. Johansen, H. Bratsberg, G. Helgesen, A.T. Skjeltorp, Potential and force between a magnet and a bulk Y 1 Ba 2 Cu 3 O 7- δ superconductor studied by a mechanical pendulum, *Supercond. Sci. Technol.* 3 (1990). <http://iopscience.iop.org/0953-2048/3/12/004> (accessed May 5, 2017).
- [194] AC/DC Module User’s Guide, 1998. www.comsol.com/blogs (accessed April 28, 2020).
- [195] H. Yamaguchi, K. Hanada, Development of Spherical Magnetic Abrasive Made by Plasma Spray, *J. Manuf. Sci. Eng.* 130 (2008) 031107. <https://doi.org/10.1115/1.2917353>.
- [196] P.S. Satsangi, H. Singh, A Study on Comparison of Abrasive Powders on the Basis of Productivity in Magnetic Abrasive Finishing, II (2016) 0–4.
- [197] Z.Q. Liu, Y. Chen, Y.J. Li, X. Zhang, Comprehensive performance evaluation of the magnetic abrasive particles, *Int. J. Adv. Manuf. Technol.* 68 (2013) 631–640. <https://doi.org/10.1007/s00170-013-4783-6>.
- [198] 2018 Nissan Leaf long-term update: One pedal (near) perfection - Roadshow, (n.d.). <https://www.cnet.com/roadshow/news/2018-nissan-leaf-update-e-pedal/> (accessed April 27, 2020).
- [199] MICHELIN Uptis :: Michelin North America, Inc., (n.d.). <https://michelinmedia.com/michelin-uptis/> (accessed April 26, 2020).
- [200] Goodyear Introduces Airless Tire Technology for Commercial Mower Application, (n.d.). <https://corporate.goodyear.com/en-US/media/news/goodyear-introduces-airless-tire-technology-for-commercial-mower-application.html> (accessed April 27, 2020).
- [201] Airless Tires | Bridgestone Tires, (n.d.). <https://www.bridgestonetire.com/tread-and->

trend/tire-talk/airless-concept-tires (accessed April 27, 2020).

- [202] Michelin and GM partner on airless, puncture-proof tire - CNN, (n.d.).
<https://www.cnn.com/2019/06/05/cars/airless-tire-michelin-gm/index.html> (accessed April 27, 2020).

Appendix A: Appendix to Chapter 3

A.1. Iron Particle Flow Analysis

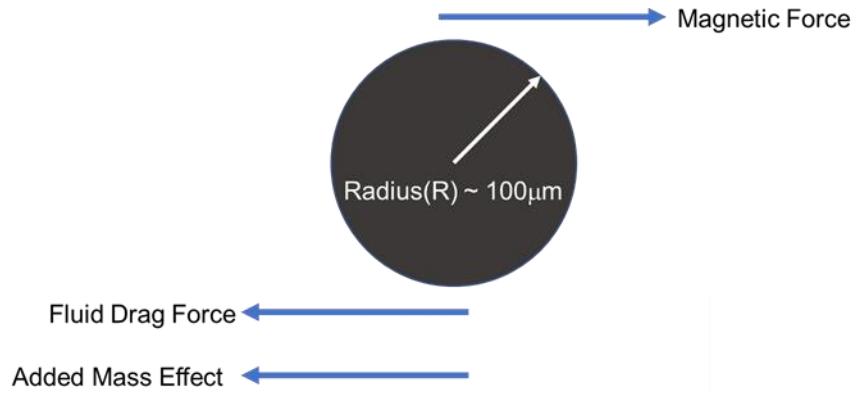


Figure A.1: Free-body force diagram of a single Iron particle.

To understand the acceleration of the Iron particles under the influence of the external magnetic field, the forces acting on the iron particles were examined. The following assumptions were made for this analysis:

- Only single particle motion is considered.
- Steady state laminar flow is assumed.
- Particle is assumed to be spherical.
- Magnet motion is assumed to be a perfect sine wave with an amplitude of 20cm/s and frequency of 1Hz.
- Particle is at center of magnet.
- Friction is omitted.

The magnetic force is calculated using:

$$\text{Magnetic Force: } F_y = V_o \chi H_y \frac{\partial H}{\partial y} \quad (\text{A.1})$$

$$\text{Drag on sphere: } F_D = 6\pi\mu Rv \quad (\text{A.2})$$

$$\text{Added Mass Effect: } m_a = \frac{2}{3}\rho\pi R^3 \quad (\text{A.3})$$

Using equations A.1-3 the following equation of motion can be derived:

$$V_o \chi H_x(t) \frac{\Delta \| \mathbf{H} \|}{\Delta x} - 6\pi\mu V_p R = \frac{3}{2} \pi R^3 \rho_{glycerol} \dot{V}_p + \frac{4}{3} \pi R^3 \rho_p \dot{V}_p \quad (\text{A.4})$$

$$\frac{\Delta \| \mathbf{H} \|}{\Delta x} = \frac{(6.1815 - 6.1812) * 10^5}{2 * 10^{-4}} = 150,000 \frac{A}{m^3} \quad (\text{A.5})$$

$$H_x(t) = H_x(x, y, z) * V_m \sin(2\pi t) \quad (\text{A.6})$$

$$\frac{dV_p}{dt} + 13600V_p = 11280V_m \sin(2\pi t) \quad (\text{A.7})$$

Recognizing that equation A.7 is a linear differential equation, a solution of the following form can be assumed.

$$\mu(t) = e^{\int p(t)dt} = e^{13600t} \quad (\text{A.8})$$

Using this solution form the solution for V_p and the acceleration a_p can be calculated as follows:

$$V_p(t) = Const. * (-V_m)(e^{-13600t} + \pi \cos(2\pi t) + 6800\sin(2\pi t)) \quad (\text{A.9})$$

$$a_p(t) = Const. * V_m(13600e^{-13600t} + 2\pi^2 \sin(2\pi t) + 13600\pi \cos(2\pi t)) \quad (\text{A.10})$$

Using these solutions the acceleration of the magnet with respect to the iron particles can be calculated and compared as seen in Figure A.2. The main conclusion is that at speeds above 20cm/s the iron particles lag behind the magnet and cannot accelerate fast enough to keep up with the magnet's motion.

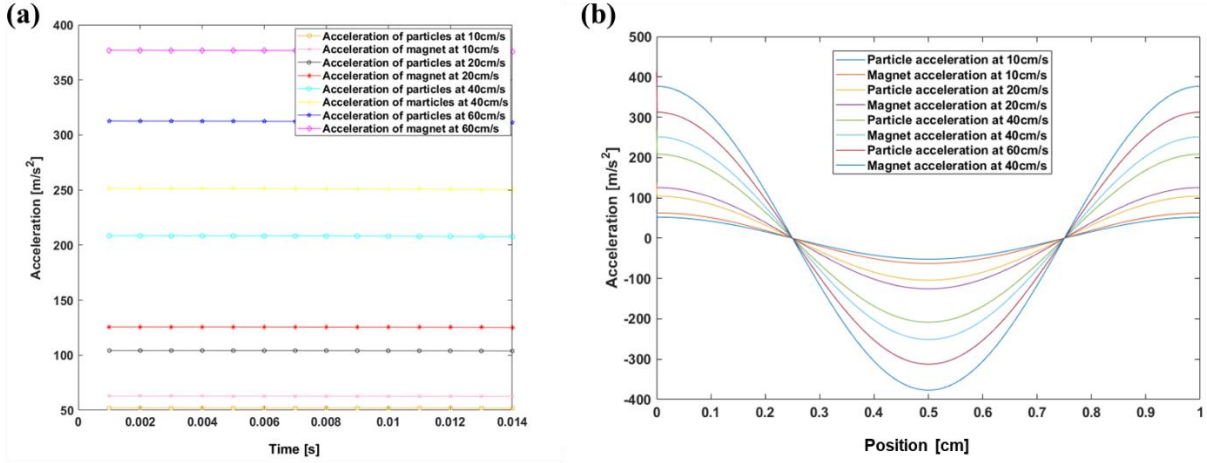


Figure A.2: Acceleration of Iron particles and magnet at different speeds. (a) Acceleration vs. time, (b) Acceleration vs. position.

A.2. Material Removal Calculations, Profile, Curvature

To understand how much material would be removed and how that would affect the profile of the final surface, simple analytical modeling was done. First, to calculate the amount of material removed a cross-section of the waveguide structure is split into 10 equal sections as shown in Figure A.3.

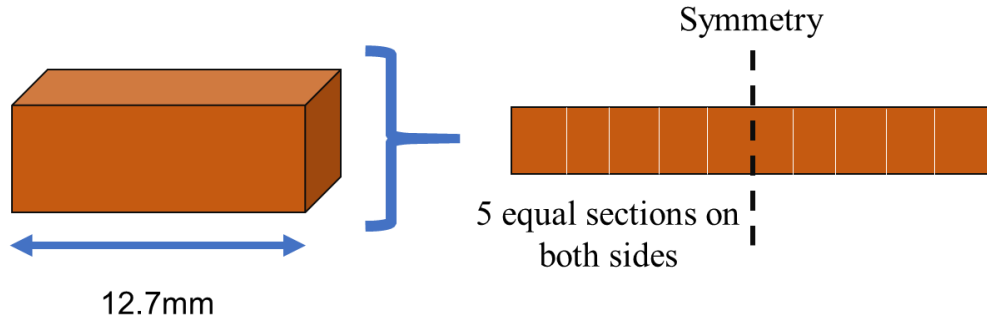


Figure A.3: Waveguide cross-section. Sectioned into 10 equal parts.

Secondly, amount of material removed is calculated for each section using:

$$h = \frac{\tan\theta P v t}{\pi H_a A} \quad (\text{A.11})$$

By using the hardness value for copper, the area that is polished, and the velocity of the magnet Eqn. A.12 can be calculated:

$$h = \frac{\tan\theta P_{avg} t}{88672.5} \quad (\text{A.12})$$

Taking $\tan\theta = \begin{bmatrix} 8 * 10^{-5} \\ 6.8 * 10^{-5} \\ 2.8 * 10^{-5} \\ 1.6 * 10^{-5} \end{bmatrix}$ [190] for each of the different abrasives used in the process and by

using the magnetic field calculations presented in chapter 3 to calculate the force, P_{avg} , the following surface profiles can be calculated.

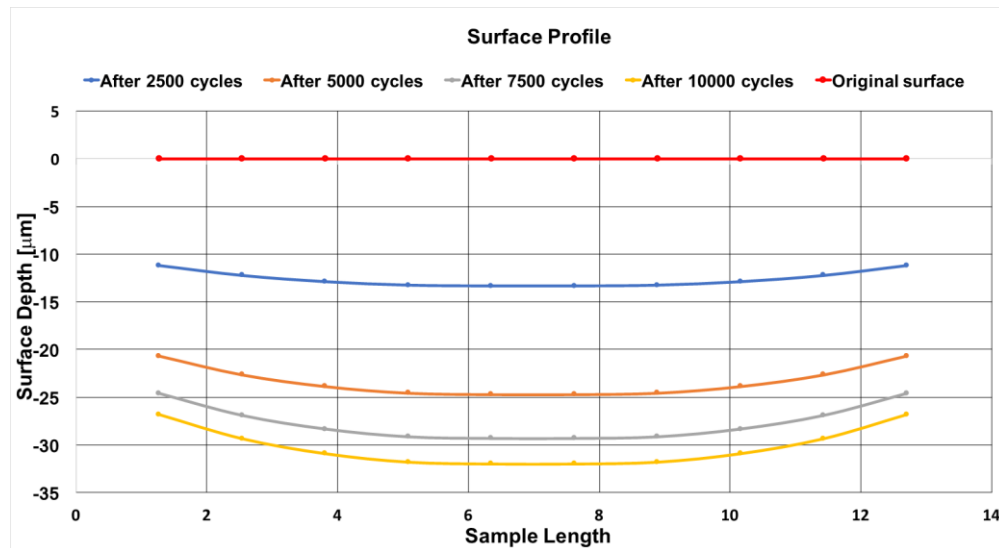


Figure A.4: Cross-sectional surface profile after different cycles.

From Figure A.4 it is seen that a 19% difference in total material removed exists between the edges and the center of the workpiece. This can be reduced by using a larger magnet to create a more uniformly distributed magnetic field.